UNIVERSITY OF BELGRADE
SCHOOL OF ELECTRICAL ENGINEERING

Petar A. Atanasijević

RESPONSE CHARACTERIZATION OF A MORPHO BUTTERFLY'S WING AS A HOLOGRAPHICALLY INTERROGATED IMAGING SENSOR

Doctoral Dissertation

Belgrade, 2024.

УНИВЕРЗИТЕТ У БЕОГРАДУ
ЕЛЕКТРОТЕХНИЧКИ ФАКУЛТЕТ

Петар А. Атанасијевић

КАРАКТЕРИЗАЦИЈА ОДЗИВА КРИЛА МОРФО ЛЕПТИРА КАО ХОЛОГРАФСКИ ИСПИТИВАНОГ СЕНЗОРА СЛИКЕ

докторска дисертација

Београд, 2024.

Подаци о ментору и члановима комисије

Ментор:

др Пеђа Михаиловић, редовни професор
Универзитет у Београду – Електротехнички факултет

Чланови комисије:

др Слободан Петричевић, редовни професор
Универзитет у Београду – Електротехнички факултет

др Јасна Црњански, ванредни професор
Универзитет у Београду – Електротехнички факултет

др Бранислав Салатић, научни сарадник
Универзитет у Београду – Институт за физику

др Марко Крстић, ванредни професор
Универзитет у Београду – Електротехнички факултет

др Ана Гавровска, ванредни професор
Универзитет у Београду – Електротехнички факултет

Датум одбране: _____.

Acknowledgments

Above all, I am grateful to my thesis supervisor Prof. Peđa Mihailović for his careful guidance throughout my post undergraduate journey, numerous hours of discussions, unrelenting effort, and for always looking out for my best interest. It was a joy being his mentee.

I owe my sincere gratitude to Dr. Dejan Pantelić. Not only did he introduce me to holography and *Morphos*, but he also conveyed his passion for them to me. I would also like to thank Dušan Grujić and the whole Photonics Center at the Institute of Physics, Belgrade. They welcomed me to their lab for my PhD journey, lending me their equipment and their experience, providing me with my first steps in the world of free-space optics.

I would like to thank the team lead by Dr. Miloš Tomić, from the Institute of Technical Sciences of the Serbian Academy of Sciences and Arts, Belgrade for lending me their equipment and their expertise during the integrating sphere measurements.

I acknowledge the selfless assistance of people in SistemCD who provided me with the free cutting services of the fragile butterfly wings using their CO_2 lasers.

To Prof. Slobodan Petričević I am deeply grateful for numerous useful advice, opportunities, as well as for many, many phone calls to ensure I do not accidentally forget to write my thesis.

To my friend Dr. Željko Janićijević I am thankful, first and foremost, for introducing me to the joy of doing science. It was his scientific spark that set me on the path we share today.

I wish to express my deep gratitude to Prof. Jasna Crnjanski, Prof. Marko Krstić, Dr. Angelina Totović, and Prof. Dejan Gvozdić, from whom I learned so much during the past decade.

I owe special thanks to my beloved friends Mladen Banović and Milana Lalović, soon to be PhDs themselves. With them, I shared the good and the bad of the PhD experience. They have, each in their own way, provided me with the encouragement and motivation to go to the finish line.

To my former students, now dear friends Filip Krajinić, Maja Živić and Milena Mićić, I am thankful for support, enthusiasm, and hard work in all the successful and unsuccessful experiments we did together.

To my friends Sonja, Vojin, Andreja, Zoka, Kaća, Keka, Vajs, Sandra and Milan I am forever grateful for reminding me of the world outside of the lab.

I thank my family for their everlasting support and kindness. To my mother I express my deepest gratitude. It was her love and encouragement that led me to where I am today.

In the end, I would like to thank my wife Milica for her love and support through it all. She was there every single step of the way, for all of my experiments, failures, successes, crazy ideas and hours of hard work. It is with this in mind that I dedicate this thesis to her and Katarina.

Doctoral dissertation title: Response characterization of a Morpho butterfly's wing as a holographically interrogated imaging sensor

Abstract: Broad spectral range imaging, with its military, scientific, medical and other applications, remains in demand of faster, more sensitive focal plane arrays. The available solutions which allow for broad infrared radiation detection come with a heavy financial toll, while necessitating complex fabrication, cryogenic cooling, and difficult readout electronics integration. In this thesis, we thoroughly characterize an alternative, bioderived approach to broad spectral range imaging, utilizing the wing scales of an unmodified *Morpho didius* butterfly as opto-thermally actuated microcantilever pixels. We show that when the array of scales is illuminated, the scale temperature increases (measured using conventional thermal imaging) with linear proportionality to the absorbed illumination intensity. This results in light-induced scale displacements, following the illumination distribution. To image this distribution, the scale displacement map is acquired using digital holographic interferometry, chosen for its high sensitivity and two-dimensional imaging capacity. The aforesaid imaging principle is examined in the range of 0.4 to $1.45\ \mu m$ illumination wavelengths, showing reproducible linear response, with average sensitivity of $0.478\ \mu m/K$. For the choice of wax with TiO_2 as the wing-mount adhesive, stable sample support is achieved, with a $55\ ms$ response time constant. The resolution limit at $20\ \%$ contrast of the wing as an imager is measured to be $1.46\ lp/mm$, a boundary set by the size of the wing scales. Finally, we conclusively demonstrate image acquisition using the holographically interrogated butterfly's wing. The proposed sensor is an attractive alternative to artificial focal plane arrays, promising high sensitivity optical readout in a broad range of wavelengths.

Keywords: holography, Morpho butterfly, image sensor, bioderived sensor

Scientific field: Physical Electronics

Scientific subfield: Nanoelectronics and Photonics

Наслов докторске дисертације: Карактеризација одзива крила Морфо лептира као холографски испитиваног сензора слике

Сажетак: Сликање у широком опсегу таласних дужина, са својим војним, истраживачким, медицинским и другим применама, и даље тражи брже и осетљивије сензоре слике. Доступна решења за детекцију зрачења широког инфрацрвеног спектра захтевају велика новчана улагања, сложену фабрикацију, криогено хлађење и отежану интеграцију са мерном електроником. У овој тези, детаљно испитујемо алтернативни, био-изведени приступ широкоспектралном сликању, који користи немодификоване љуспице крила *Морфо дидиус* лептира као опто-термално побуђиване микроконзолне пикселе. Показујемо да када је низ љуспица осветљен, њихова температура расте (мерено уобичајеним термалним сликањем) линеарно са апсорбованим интензитетом осветљења, док њихово последично померање прати расподелу зрачења. Како би се ова расподела снимила, мапа померања љуспица се мери применом дигиталне холографске интерферометрије, изабране због високе осетљивости мерења и способности дводимензионалног сликања. Предложена метода сликања је испитивана у опсегу таласних дужина осветљења од 0.4 до $1.45\ \mu m$, где је показала поновљив и линеаран одзив, средње осетљивости од $0.478\ \mu m/K$. У случају избора воска са TiO_2 као адхезива између крила и постоља, постигнуто је стабилно монтирање крила, уз временску константу одзива од $55\ ms$. За крило као сензор слике, измерена је резолуција од $1.46\ lp/mm$ за 20 % контраста. Ова граница је фундаментално постављена величином љуспица. На крају, са сигурношћу демонстрирамо аквизицију слике коришћењем холографски испитиваног крила лептира. Предложени сензор представља примамљиву алтернативу вештачким сензорима слике, обећавајући високо осетљиво оптичко ишчитавање у широком опсегу таласних дужина.

Кључне речи: холографија, Морфо лептир, сензор слике, био-изведени сензор

Научна област: Физичка Електроника

Ужа научна област: Наноелектроника и фотоника

Table of Contents

Table of Figures

Table of Tables

List of abbreviations

A Aperture in optical setups

ADC Analog-to-Digital Controller

BS Beam Splitter

CCD Charged Coupled Device

CM Concave Mirror

CMOS Complementary Metal Oxide Semiconductor

DAC Digital-to-Analog Converter

DC Direct Current

DHI Digital Holographic Interferometry

EB Excitation Beam

ES Excitation Section

ESF Edge Spread Function

FFT Fast Fourier Transform

FPA Focal Plane Array

FPGA Field Programmable Gate Array

GPU Graphics Processing Unit

GSA Gerchberg-Saxton algorithm

L Lens in optical setups

LD Laser Diode

L-I Light-Current

LSF Line Spread Function

LWIR Long-Wave InfraRed

M Mirror in optical setups

MEMS MicroElectroMechanical Sensors

MO Microscope Objective

MOSFET Metal-Oxide-Semiconductor Field-Effect Transistor

MTF Modulation Transfer Fnction

MWIR Mid-Wave InfraRed

NDF Neutral Density Filter

NETD Noise Equivalent Temperature Difference

NIR Near InfraRed

OPA OPerational Amplifier

OTF Optical Transfer Function

PC Personal Computer

PD PhotoDiode

PH Pin Hole

PID Proportional Integral Differential

PSF Point Spread Function

ROIC ReadOut Integrated Circuit

S Sample in optical setups

SWCNT Single-Walled Carbon NanoTube

TEC ThermoElectric temperature Controller

TIA TransImpedance Amplifier

UV UltraViolet

Chapter 1. Introduction

"While there is much truth in the statement that necessity is the mother of invention, it has often been pointed out that it is far from true that necessity is the mother of discovery. Discoveries come often most unexpectedly, in the pursuit of knowledge by the curious and observant" – Karl T. Compton [1].

The strict criteria of animal evolution favored the ability to see from early on. While there is a multitude of research focused toward exploring why and how the different visual systems of today's animals came to be, it is a unanimous opinion that they provide the species with unmatched advantages [2–4]. The eyes enabled animals to navigate through the surroundings, detect and discern predators and prey, and generally perform a wide range of different visually guided tasks. In his book, "*On the Origin of Species*" Charles Darwin listed the eyes as "*organs of extreme perfection and complication".* Due to their complex nature, focusing capacity, huge dynamic range, and aberration correction, even Darwin was left in disbelief that they came to be just as a result of natural selection [5]. Thus, it is no wonder that with the development of early science and technology, humanity aspired toward the creation of artificial imaging devices. The first such device "*camera obscura*" devised many centuries ago, was documented on multiple occasions throughout history [6], most notably by Leonardo da Vinci himself in "*Codex Atlanticus*". Also known as a pinhole camera, camera obscura required no lenses, just a darkened room and a small hole through which a weak upside-down image of the outside was projected on the wall. Further developments added a positive lens in place of the hole, creating a predecessor of a modern-day objective. Then came photography and analog imaging. Just like the evolution of the eyes came hand-in-hand with the evolution of the brain, able to process the raw visual stimuli, the development of artificial imaging came hand-in-hand with the development of electronics and silicon fabrication processes. This gave rise to a new era of artificial vision hardware – digital image sensors in silicon. The most prominent examples of this group are definitely the Charged Coupled Devices (CCDs) and Complementary Metal Oxide Semiconductor (CMOS) sensors. The latter are especially widespread due to their low price and well-rehearsed fabrication processes, available in most smartphones, computers and cameras of today. A thorough review of the working principles, performance and applications of CCDs and CMOS sensors is provided in a book by Daniel Durini [7]. It is worth noting that today's sensors enable our species to record images at thousands of frames per second, image distant stars, microorganisms, light's polarization, and even image individual photons [8–10], giving rise to a new kind of modern-day evolution driven by the available vision systems.

Looking back, it can be deduced that throughout most of the known history, humankind focused its efforts on imaging the visible light, electromagnetic radiation with wavelengths between roughly 380 and $700\ nm$ in vacuum. It was not until the year 1800. that the radiation beyond the visible spectrum was first detected by William Herschel [11]. Herschel conducted an experiment in which he used a prism to disperse sunlight, separating different wavelengths across the white paper on his desk. He then exposed blackened glass bulb thermometers to different "colors" of the spectrum,

measuring their temperature, and finding that the highest temperature increase occurred just above the "red" color (under in terms of photon energy), in the infrared spectral region. At the end of his paper, he assumes these rays to be "*a true account of solar heat*", undetectable by humans due to the "*construction of the organs of sight*" [11]. Throughout the following couple of decades, technology for detecting radiated heat did not exhibit significant advancements surpassing Herschel's thermometers. Then came the Seebeck effect, the first thermocouple and consequently thermopile sensors, dominating the detector game in the infrared until the last decades of the nineteenth century. Thermopile's performance was first surpassed by highly sensitive bolometer sensors, completing the list of early, pre-twentieth century infrared detectors. Understandably, all of the aforementioned devices are classified as thermal infrared detectors. The next century brought the widespread application of the recently discovered photoelectric effect, giving rise to the development of photon detectors both in the visible, and in the infrared spectral region. The choice of material for photon detectors varied over the years, culminating with InGaAs, InSb and HgCdTe sensors covering the near infrared (NIR), mid-wave infrared (MWIR) and a portion of the long-wave infrared (LWIR) spectrum. The research into thermal detectors, focusing especially on thermal imagers (focal plane arrays – FPAs) during the twentieth century (and beyond) was mostly guided by military applications. Thus, thermal imaging became one of the key military imaging technologies, along image intensifiers in the visible spectrum. A comprehensive survey of the beginnings of infrared detectors is provided by Rogalski [12].

1.1 Infrared imaging

Today, infrared FPAs can be naturally divided into two main subcategories, thermal and photon (quantum) detectors. Both have their applications, based on their respective strengths and weaknesses. With the decrease in prices over the course of the last twenty years, thermal FPAs became available to the general public. On the other hand, more sensitive and advanced FPA photon detectors still require strict, hard to maintain operating conditions. Thus, they are reserved for enhanced military and/or scientific applications. The key physical parameters of the available FPAs are their pixel sizes and response times. The FPA's pixel size keeps decreasing for all FPA types (currently on the order of $\sim 10 + \ \mu m$), while the number of pixels in an array continues to increase, though not at a pace dictated by the visible FPAs. While discussing further reduction in pixel size of the novel detectors, challenges of small pixels, most notably due to diffraction should be kept in mind [13]. The response speed also lags behind the visible imagers, varying among detector types. However, examples of sophisticated commercially available FPAs reaching hundreds to thousands of frames per second can be found [14].

Thermal FPAs currently rely on three mainstream technologies, thermopile FPAs, pyroelectric FPAs, and microbolometer FPAs. Of the three, the last one is by far the most used technology in infrared imaging, not just among thermal detectors, but in general [12,15]. A simplified illustration of the microbolometer pixel design and FPAs is provided in Figure 1.1. The microbolometer functioning principle is rather simple. The heat from the infrared source is absorbed by a resistive element with small thermal capacity and large resistance's temperature dependence. Thus, the induced temperature increase of the microbolometer results in a resistance change, proportional to the amount of incident infrared radiation. The resistance change is readily measured using multiple techniques within the ReadOut Integrated Circuit (ROIC), out of which the simplest utilize a current source with voltage measurement, or a Wheatstone bridge architecture [16]. Today, the usual microbolometer material selection offers a choice between either vanadium oxide (VO_x) or amorphous silicon (a-Si) technologies, offered by different manufacturers [15]. The most noteworthy advantages of thermal detectors are their uncooled operation and broad spectral response. They are easier to manufacture and are less expensive compared to their photon detecting counterparts. However, thermal detectors exhibit more noise, they are less sensitive and inherently slower due to the thermal inertia of their

pixels. The problems of sensitivity and response time are unfortunately contradicting, as the increase in sensitivity due to the increase in pixel area consequently increases the pixel's thermal inertia.

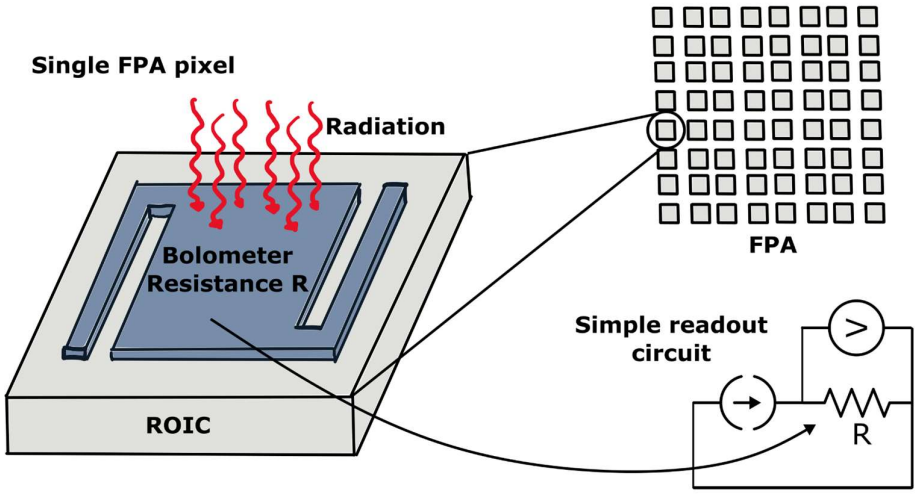

Figure 1.1 An illustration of a microbolometer pixel, and a simple readout circuit.

Photon detecting FPAs in the infrared rely on the absorption of quanta of infrared radiation by the material, exciting the charge carriers to higher energy states. Due to the absence of slow thermal processes, it is no wonder why these types of detectors achieve much higher operating speeds compared to their thermal counterparts. However, the first challenge in design of such devices arises from the fact that infrared radiation consists of low-energy photons, often lacking the capacity to overcome the energy bandgap of the commonly used materials such as silicon. Thus, lower energy bandgaps were required, leading to the inclusion of the aforementioned InGaAs, InSb and HgCdTe alloys in the thermal imaging field. Lower bandgaps on the other hand facilitate easier carrier excitation due to unwanted thermal fluctuations, resulting in a very high influence of thermally generated noise. To overcome this limitation, and the problem of energy bandgap's temperature dependence, the infrared photon detectors must be cooled to stable cryogenic temperatures, making them expensive, bulky and complex. While there is a lot of work currently directed toward enabling the uncooled operation of the FPAs of this type, much more is yet to be achieved [17]. Furthermore, due to the presence of the bandgap E_g, however small, the spectral response of the photon detecting FPAs will always be non-uniform and exhibit a drop approaching the wavelength $\lambda = hc/E_g$, where h is the Planck's constant, and c is the speed of light. This fundamentally limits their use in detection of wide spectrum illumination. The illustration of the theoretical spectral sensitivity trends for both thermal and photon detectors is provided in Figure 1.2. The spectral sensitivity is assumed to have units of the detector's output (response) per unit of the absorbed incident radiation.

Due to the shortcomings of the available FPAs designed for thermal imaging, a multitude of enhancement/alternative approaches was proposed over the years. Prior to going into the details, and citing individual methodologies, this is a good place to quote a theorem, devised at the end of the past century, predicting the research directions in infrared detection:

"All physical phenomena in the range of 0.1-1 eV will be proposed as an infrared detector." – Paul R. Norton [18].

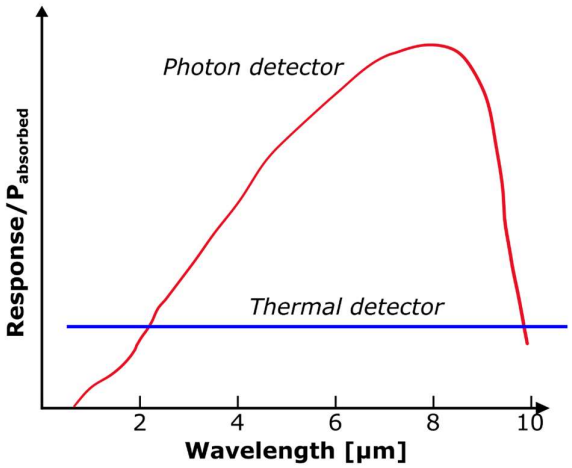

Figure 1.2 Spectral sensitivity of photon and thermal detectors.

1.2 Unconventional approaches to infrared detection

Norton's theorem proved to be very accurate in predicting the wide-ranging future research trends, most focusing on improving the response of uncooled detection. Throughout the last couple of decades, infrared detectors utilizing both simple physics of thermally induced bending (microcantilever sensors) [19,20], and highly advanced physics based on cutting-edge photonics, two-dimensional materials, nanotechnology and nanophotonics were proposed [21–26]. Just some examples of the latter group count thousands of papers in the last five years ♦. As their functioning principles fall outside of the scope of this thesis due to their complexity or rarity of concrete imaging demonstrations, the interested reader is referred to the articles in which they are thoroughly reviewed [27–29]. On the other hand, microcantilever sensors are of interest to the following text both because of their effectiveness and simplicity, practical imaging demonstrations, and the relatedness to the phenomena discussed in this thesis.

During the first decade of this century, intensive research into the uncooled microcantilever sensors resulted in multiple demonstrations of working FPAs with simpler designs and higher sensitivities compared to microbolometers [30–35]. They base their light detection capacity on the simple physics of thermomechanics. The cantilevers are pixels of the FPA, absorbing incident radiation, causing their temperature to increase. Due to the increase in temperature, the cantilevers bend, usually most intensively at the free-standing end – the cantilever's tip. The tip's displacement is proportional to the temperature increase, in turn proportional to the amount of absorbed radiation. By measuring the displacement, the light's intensity can become known. These devices are by all standards microelectromechanical sensors (MEMS), as their structures exhibit ~ 10 to $\sim 100\ \mu m$ dimensions and are usually fabricated through processes similar to standard electronic fabrication. The response of the microcantilever sensor is enhanced greatly by making the cantilever bimaterial. Materials of choice are expected to have different thermal expansion coefficients, causing one to expand more than the other, thus increasing the bending. Furthermore, one of the materials should be a good absorber in the desired spectral region – usually the infrared. The other is chosen to allow the displacement signal to be measured by one of the usual readout methods. Typical combinations of materials are silicon nitride and gold, or silicon dioxide and aluminium, where both silicon nitride

♦ Source: https://app.dimensions.ai/, search: "infrared detection nanomaterials" – 140861 papers, "infrared detection 2d material" – 226498 papers in the 2019-2023. period.

and silicon dioxide serve as radiation absorbers [15]. While most papers on microcantilever infrared sensors provide a theoretical background of sensor operation through analytical and/or numerical approaches, separate studies focusing on general theory of operation/characterization were published [36]. The illustration of the light induced bending of a simple microcantilever is shown in Figure 1.3 a).

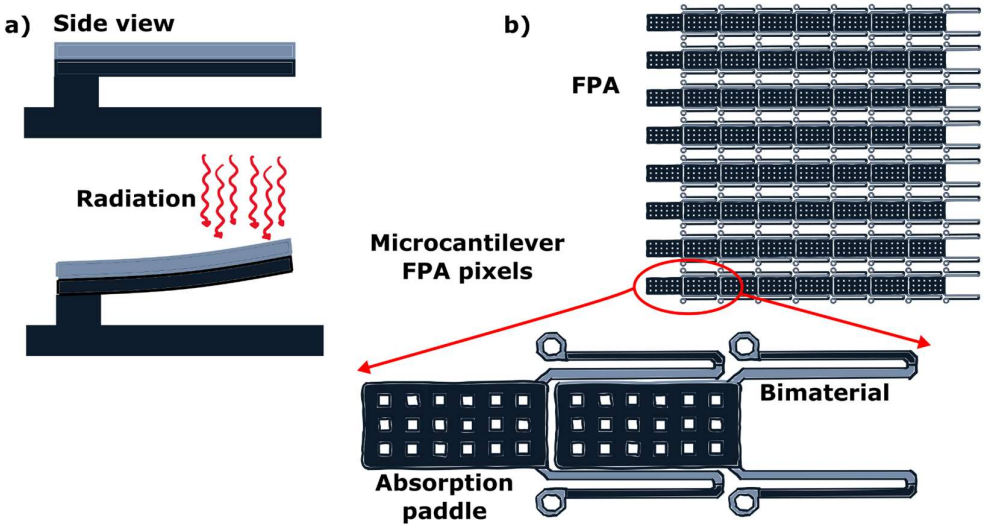

Figure 1.3 Microcantilever infrared sensors: a) bending due to the incident radiation; b) one of the proposed pixel designs with a distinctive absorption paddle, and supporting bimaterial cantilevers [30,37].

To readout the radiation induced displacement of the cantilever, multiple approaches were proposed, e.g. capacitive [19,30,37], optical [32,35,38,39], piezoresistive [40,41] or electron tunneling [42]. The first two methods yielded the most significant demonstrations. Capacitive readout of the cantilever bending requires the existence of metalized contacts both on the cantilever and the substrate, creating a capacitor. With the radiation induced displacement of the cantilever electrode, the distance between electrodes changes. This provides a capacitance change electrical signal, easily readout using a capacitive half-bridge ROIC [30,37]. The fabrication of capacitively readout microcantilever pixels with dimensions of 25 to 50 μm were reported, exhibiting displacement sensitivities of 100 to 400 nm/K (higher for larger cantilevers) [30]. The pixel's complex structure incorporated an infrared absorber paddle, connected to folded bimaterial arms, enabling enhanced response and ambient temperature compensation. The illustration of the pixels is shown in Figure 1.3 b). As an alternative to the proposed electrical readout principles, the optical readout came with the ease in scalability to very large arrays [43], and no necessity for ROIC. This significantly reduces the cost and complexity of sensor's fabrication, while eliminating both the ROIC's thermal influence and electronic noise. To optically measure the displacements of a microcantilever array, back focal plane optical spatial filtering is utilized [44]. The array is illuminated with a collimated monochromatic beam of visible light. The reflective surfaces of cantilevers reflect the incoming light, which is then collected with a Fourier lens, creating a diffraction spectrum in its focal plane. Using a spatial filter (circular, or knife edge), only a part of the spectrum is transmitted to the objective lens of the camera, projecting the sharp image of the interrogated FPA to the visible image sensor. When the cantilevers displace due to the exposure to the infrared, the spectrum in the back focal plane of the Fourier lens exhibits a spatial shift becoming partially blocked by the filter. Thus, a change in the intensity of the acquired visible image is observed, enabling the cantilever angle-to-intensity conversion [34,44–46]. However, the discussed principles of optical readout exhibit an obvious drawback. If some of the pixels are deflected at a different angle compared to the others because of fabrication non-uniformities, their

spectrum will be inherently shifted, and they will provide no signal at the detector. The influence of "dead" pixels is then remedied through inpainting [43].

Research into improving the basic outlined principles went in several directions. Free-standing cantilevers were fabricated, eliminating the negative influence of substrate [47–53]. Novel cantilever designs were devised to increase the sensitivity [32]. "Self-leveling" detector was proposed [54]. Thermal stabilization system was designed [20]. Thermal image processing methods for microcantilever FPAs were discussed [43,55,56]. The maximum target temperature [57], and sensor's pressure-dependent performance were studied [58]. Recent publications concerning bimaterial microcantilevers dealt with the choice of spatial filtering techniques [44], the effects of cantilever's physical dimensions [59,60], and wavelength dependence [61] on FPA's response.

Diverse pixel designs proposed by leading groups showed different device performances. Gong et al. reported infrared image acquisition using $146\ \mu m$ pixels, deflecting $7.494\ \mu m$ for temperature changes of $178.2\ K$ yielding a sensitivity of $42\ nm/K$ [57]. Lim et al. simulated and fabricated the flip over bimaterial beams, increasing the thermomechanical sensitivity of $100\ \mu m$ pixels to $180\ nm/K$ [32]. In 2007. Guo et al. reported $178\ \mu m$ cantilevers exhibiting sensitivities of $77.4\ nm/K$ with demonstration of infrared image acquisition [51]. The paper was published by the same group next year in which they theoretically investigated $120\ \mu m$ pixels showing $138\ nm/K$ sensitivity and $70\ ms$ response times. Image acquisition was demonstrated, and sensitivity underperformance of experimental measurements was discussed [50]. Studies by Lavrik and Grbović reported different combinations of results over the years. In a paper [35] they demonstrate imaging using $75\ \mu m$ pixels with very low time constants of only $6\ ms$ and sensitivity of $50\ nm/K$. Two years later, $220\ \mu m$ complex pixel structures were fabricated, resulting in sensitivities on the order of 500 to $1000\ nm/K$ and time constants between 53.5 and $62.5\ ms$ [47]. Unusual chitin-ceramic bimaterial choice was theoretically investigated by Zhang et al. showing great promise in sensitivity increase of up to $1.6\ \mu m/K$ [62]. However, no experimental verification, nor imaging demonstration was published.

It is noteworthy to emphasize that trends in unconventional infrared detection technologies pretend to go further above or below the limits of the infrared, to the terahertz [47,63], or visible spectral regions [64–68] enabling broader spectral range detection.

1.3 Bioderived Morpho butterfly infrared sensors

Facing the high prices and operating requirements of cooled photon detecting FPAs at one end, and complexity, low sensitivity and speed of microbolometers at the other, some researchers have turned to nature for inspiration on light detection, relying on the field of biomimetics. The development of nature-inspired sensors is usually justified by the simplicity and efficiency of the sensing systems found in biological specimens. They provide fruitful inspiration due to the optimization of their performance through millennia of rigorous evolutive processes. Many such solutions have been proposed [69–71]. In the field of bioinspired sensors, photonic structures prove to be exceptionally useful due to their highly sensitive, non-destructive optical readout capacity. A review on different biomimetic photonic sensors gives an in-depth survey of the noteworthy contributions [72].

Among the photonic elements found in nature, the structures on the wings of *Morpho* butterflies stand out by their mesmerizing beautiful blue color, as well as the versatility in their biomimetic applications. Most of the aforesaid applications base their operation on the properties of the thin-film-like Christmas tree structures, responsible for the butterfly's blue coloration. The branches of the structures are made from chitin, the nature's second most abundant biopolymer [73]. They are periodically separated by gaps filled with the surrounding medium – usually air. Both the order of the repeating structure, as well as the disorder in the length of its branches result in the phenomenon of iridescence [74–76]. The iridescence is in turn strongly dependent on the dimensions of the branches, and the air (medium) gaps, their refractive index, the angle of the scales on which they

are found etc. The change in any of the listed physical properties, as a result of the modulation by the measurand, changes the wavelength dependent reflectance/transmittance, providing an easily discernable optical output. Based on these principles *Morpho* butterfly wings were employed to achieve repetitive DNA amplification [77], detect pH variations [78,79], acoustic vibrations [80], hydrogen gas concentration [81], different solvents [79], temperature [82], and infrared radiation [83–86]. The reader interested in *Morpho* inspired sensing and biomimetic applications other than the infrared radiation detection is referred to one of the several published review articles [87–90].

The pioneering work on infrared radiation detection using *Morpho* butterfly wings was conducted by Pris et al [83]. They used the wings of a *Morpho sulkowsky* butterfly as "wavelength converters", transforming the modulation in the MWIR spectral region to a change of the visible optical readout. The wings were enhanced by single-walled carbon nanotube (SWCNT) doping improving their infrared response. The incident MWIR radiation is reported to cause the heating of the Christmas tree-like structures, consequently resulting in their thermal expansion. The change in dimensions of the structures changed the spectral dependence of reflectance, to be measured using differential spectroscopy. The sensitivity of the response depends on the measurement wavelength, showing a maximum of -5.4 % reflectance change for a wing's temperature change of 4.8 ℃. Due to the very low thermal inertia of the wing scales, high uncooled response speeds up to 40 Hz were reported, although at a significant cost of the signal to noise ratio [83]. The illustration of the detection principle, employed by Pris et al. is shown in Figure 1.4.

Zhang et al. further explored the outlined idea, reporting significantly improved sensitivity for the *Morpho sulkowsky* wings with deposited gold coatings [85]. The coatings on chitin formed bimaterial structures with different thermal expansion coefficients. Upon the heating with infrared illumination, the structures' mechanical response was amplified due to their bimaterial nature. Thus, the relative reflectance drop nearly doubled (-11 %) for the 5 ℃ temperature increase, compared to the study of Pris et al. The illumination was modulated using an optical chopper, resulting in 1.5 % reflectance change signal amplitude at 5 Hz. The illustrations of the bimaterial structures realized by Pris et al. and Zhang et al. are shown in the inset of Figure 1.4.

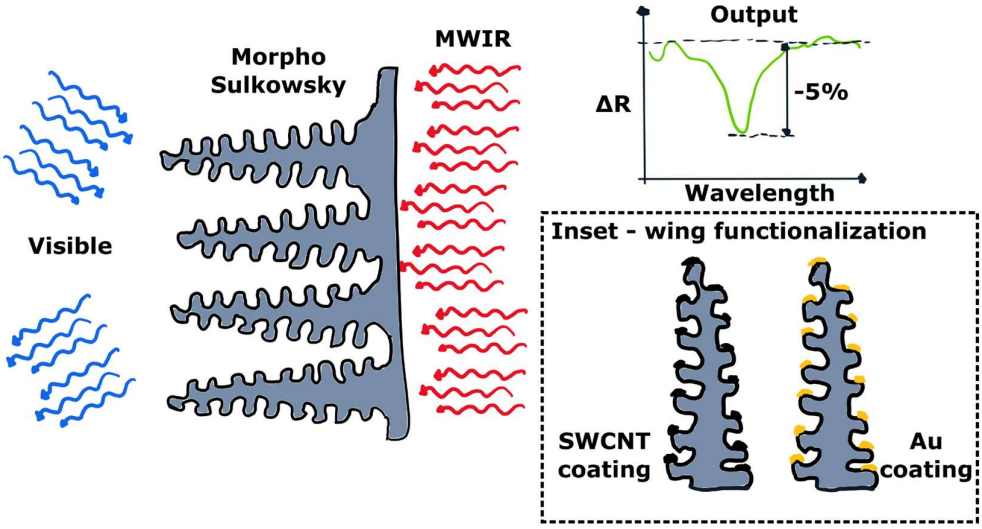

Figure 1.4 The illustration of the wavelength conversion principle proposed by Pris et al. employing the *Morpho* butterfly's wing. The inset shows the illustrations of the functionalized bimaterial Christmas-tree-like structures [83,85].

Shen et al. took the same reflectance change approach utilized in the previous two studies [86]. However, they implemented a different strategy in wing functionalization, exposing the *Morpho*

sulkowsky wings to the water vapor at saturated pressure, causing adsorption. This resulted in a significant drop of the wing's reflectance, especially around the naturally occurring spectral interferometric peak. When such a structure was exposed to the infrared radiation, desorption of vapor molecules was induced, causing a partial return of the interferometric peak, resulting in up to $78\ \%$ reflectance increase, for $5.2\ ℃$ induced temperature changes. The reported increase in sensitivity is accompanied by the benefits of spectral selectivity in measurement, as molecules with different spectral responses can be utilized instead of water. The response speed of up to $60\ Hz$ was achieved, accompanied by a signal to noise ratio of ≈ 60.

Grujić et al. explored a different methodology, treating the wing scales of an unmodified *Morpho menelaus* butterfly as cantilevers that bend due to the temperature gradient induced by the infrared radiation [84]. The measurement of the cantilever displacement was conducted using digital holography. This was the first proposed readout principle which enabled imaging of the infrared radiation induced changes on the surface of the wings. Using a $8.7\ mW$, $980\ nm$ wavelength laser excitation, with $128\ ms$ exposure, they demonstrated the point induced holographically observable phase change of $5.1\ rad$. Knowing the induced temperature difference of $0.4\ K$, the sensitivity of the scales as cantilevers is calculated to be $0.540\ \mu m/K$. This research presents a proof of concept of a novel readout mechanism with promising performance, leaving much to be further studied regarding the detailed response characterization of such a sensor.

1.4 Research motivation and the proposed approach

The aforesaid bioderived sensors showed promising results in uncooled infrared detection, marking the technology based on *Morphos* as a viable future alternative to microbolometers. However, the image acquisition using a *Morpho* butterfly as a sensitive FPA was not yet demonstrated. No response calibration, nor spectral characteristics were experimentally examined. In this thesis, we aim to fill this research vacancy, providing not only a demonstration of imaging, but an in-depth characterization of the sensor's response. To achieve this, we adopt the approach of Grujić et al. as it showed the most promise in two-dimensional radiation detection. We treat the wing scales of a *Morpho* butterfly as microcantilever pixels of a bioderived FPA, exhibiting opto-thermo-mechanical response. As the induced displacements are very small (on the order of microns), we employ digital holographic interferometry to measure them. They displace/bend due to the heating by the incident light, the phase of the acquired hologram changes, and the light induced displacement map over the whole sample area is acquired. This map is regarded as the FPA output and will further be analyzed. Like Grujić et al. we exert no modifications to the natural wing structure. We use the wing "as is", eliminating the complexity of functionalization during the preparation procedures. The proposed detection mechanism inherently has a very broad spectral response with no energy bandgap limitations, promising to overcome the difficulties of simultaneous radiation detection in multispectral regions.

To quantitatively describe the wing's imaging performance, we will devise adaptations of the conventional characterization techniques. Spatial response of the wing will be analyzed through the modulation transfer and contrast transfer measurements. Temporal characteristics will be obtained based on the step excitation response. Response linearity and spectral calibration will be conducted at several wavelengths throughout the visible and NIR spectral regions. To optimize different performance parameters of the wing FPA, different options in mounting the wing to the sample holder will be examined.

The detection principles proposed in this thesis prove the theorem of Paul Norton yet again, while providing concrete evidence of the broad-spectrum imaging capacity of our unusual approach.

1.5 Research outcomes and thesis organization

Within this thesis, we aim to:

- investigate the sensitivity, spatial, temporal, and spectral response of the *Morpho didius* butterfly's wing as a holographically interrogated imaging sensor,
- devise a metric correlating the holographically measurable response to the illumination intensity, enabling sensor's calibration with reduced influence of the scaling during the hologram reconstruction procedure,
- characterize the correlation between the illumination wavelength, the induced temperature change, and the resulting wing displacement,
- investigate the influence of the adhesive material choice, and the temperature of the wing's mount, on the sensor's temporal response, and
- demonstrate the first image acquisition using a wing of a *Morpho didius* butterfly.

This thesis is based on the following publications [91–95]:

I **Atanasijevic, P.**, Grujic, D., Krajinic, F., Mihailovic, P., & Pantelic, D. (2023). Characterization of a bioderived imaging sensor based on a Morpho butterfly's wing. Optics & Laser Technology, 159, 108919.

https://doi.org/10.1016/J.OPTLASTEC.2022.108919

II **Atanasijevic, P.**, Mihailovic, P., Grujic, D., Pantelic, D., & Skenderovic, H. (2021). Morpho butterfly wings as imaging sensor. 14th Photonics Workshop, 29.

III **Atanasijevic, P.**, Krajinic, F., Mihailovic, P., & Pantelic, D. (2023). Thermoelectric temperature control of Morpho butterfly wings used for radiation sensing. 16th Photonics Workshop, 20.

IV Zivic, M., **Atanasijevic, P.**, & Barjaktarovic, M. (2021). Development of a digital holographic microscope for observation of Morpho butterfly wing scales. 2021 29th Telecommunications Forum, TELFOR 2021 - Proceedings.

https://doi.org/10.1109/TELFOR52709.2021.9653260

V Mićić, M., **Atanasijević, P.**, & Mihailovic, P. (2024). Laser diode driver on a Programmable System on a Chip. Review of Scientific Instruments.

https://doi.org/10.1063/5.0184666, accepted for publication.

It is worth noting that the results of publications **IV** and **V** are used within the context of this thesis, although the full scope of their contributions is far from limited to what is outlined in the text that follows.

The thesis is organized as follows:

- **Chapter 2.** gives an introduction to the holographic methods used for wing displacement interrogation. Utilized hologram reconstruction techniques, and post-processing operations are explained.
- **Chapter 3.** outlines the properties of *Morpho didius* wings and photonic structures, focusing on their consequential influence on the proposed sensor's response. Sample preparation procedures are explained and discussed, different adhesive materials are introduced, and wing's spectral reflectance/transmittance/absorptance curves are presented.
- **Chapter 4.** presents the experimental setups that are used throughout the thesis. Details of both the holographic/thermographic setups, and the custom designed electronic devices

are discussed. The dedicatedly devised software used in the experiments is described and its operation illustrated via a flow chart.

- **Chapter 5.** shows the experimental results of light induced displacements and discusses their properties. Changes in response of different types of samples are considered. Negative side-effects of the wing's opto-thermo-mechanical response are introduced and suppressed using custom designed numerical approaches. Results of the wing's spectral calibration are presented.
- **Chapter 6.** deals with the wing's temporal response. A simple physical model based on the wing's average temperature increase is devised, explaining the characteristic shapes of the response curves. Response times of different sample types are measured and comparatively analyzed. The influence of active control of the wing's back surface temperature on the light induced holographic response is experimentally investigated.
- **Chapter 7.** introduces the limitations in spatial resolving capacity of the proposed imaging sensor. Sensor's response uniformity is experimentally investigated. Its modulation transfer capacity is characterized using different measurement approaches, validating the obtained results. Finally, the image acquisition using a butterfly's wing is demonstrated for multiple excitation shapes.
- **Chapter 8.** discusses the presented results, placing them in perspective to the state-of-the-art in the field of conventional and unconventional uncooled imaging sensors with broad spectral range capacity.
- **Chapter 9.** concludes the thesis with final remarks, providing an outlook into future research perspectives.

Chapter 2. Holographic imaging

"The future cannot be predicted, but futures can be invented. It was man's ability to invent which has made human society what it is." - Dennis Gabor, awarded the Physics Nobel Prize in 1971. for his invention of holography.

Throughout the history, the field of optics relied on coherent phase measurement techniques to provide the world with its most sensitive detectors, some of the most groundbreaking examples being the original Michelson interferometer, and the gravitational wave detector [96,97]. The common factor for the aforementioned techniques is that the phase information of the electric field could not be measured directly, but through its consequential influence on light intensity due to light interference. To this day, directly measuring the light's electric field awaits further breakthroughs, as not many detection principles demonstrated the ability to capture frequencies of hundreds of terahertz [98].

A milestone was achieved in 1948. when Dennis Gabor proposed "*A new microscopic principle*" to compensate for strong influence of aberrations in electron microscopy, consequently changing the field of optics forever [99]. In his paper, he postulated and demonstrated the recording and reconstruction of amplitude and phase of a light wave scattered from a semi-transparent object, using an interference pattern of the said wave with the reference wave of a known wavefield. This principle later became known as the holographic principle, while the recording which stored the image of the object and reference wave's interference pattern became known as a hologram. The name was chosen to imply its ability to record the "complete" information describing the light wave.

Being able to image both the amplitude and phase of light soon found many applications in precise measurements, non-destructive testing, biology, and medicine [100,101]. A leap forward in the field was achieved after the invention of a laser, greatly improving the quality and availability of coherent imaging. Following the discovery of digital image sensors, numerical approaches were developed which enabled the transition of holography from analog to a new digital domain [102,103]. Today, holography has become quantum [104,105], holographic systems became available to the general public [106], while holographic methods benefit from novel computational paradigms such as neural networks [107].

2.1 Hologram recording and reconstruction

An illustration of a holographic recording of light reflected from an object (a duckling) is shown in Figure 2.1 a). The presented setup divides the wavefront of a coherent spherical wave, originating from a point source usually generated in the focus of a lens or by a pinhole. One part of the wavefront is incident upon the object, and after reflection becomes the object wave $\underline{E_O(x,y)}$ with the object surface information imprinted in its amplitude and phase. The other part of the wavefront is redirected using a plane mirror, creating a reference wave $\underline{E_R(x,y)}$, still having the characteristics

of the original spherical wave. The two waves meet and interfere at the recording medium creating a hologram. The following equation describes the electric fields of the object and reference waves:

$$\underline{E_o(x,y)} = \left|\underline{E_o(x,y)}\right| e^{j\phi(x,y)}$$
$$\underline{E_R(x,y)} = \left|\underline{E_R(x,y)}\right| e^{j\psi(x,y)} \quad (1)$$

where $\left|\underline{E_O(x,y)}\right|$ and $\left|\underline{E_R(x,y)}\right|$ are the moduli of the complex object and reference fields, while $\phi(x,y)$ and $\psi(x,y)$ denote their phases, respectively. The intensity $I(x,y)$ of the resulting interference pattern is then proportional to the squared modulus of the sum of the complex fields:

$$I(x,y) \sim \left|\underline{E_R}\right|^2 + \left|\underline{E_o}\right|^2 + \underline{E_R}^* \underline{E_o} + \underline{E_R E_o}^* \quad (2)$$

where the proportionality constant, although known, remains irrelevant in most applications.

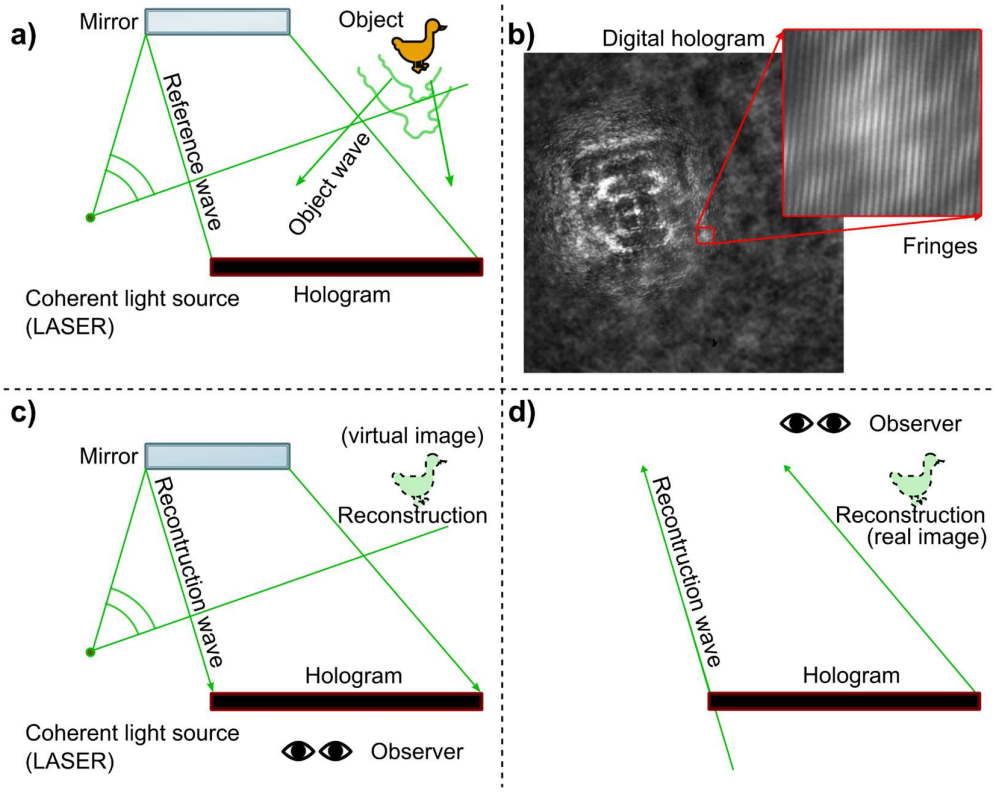

Figure 2.1 a) Illustration of holographic recording; b) Digital hologram with holographic fringes shown in the inset; c) Reconstruction of a hologram using the original reference wave, forming the virtual image; d) Reconstruction using the conjugated reference wave, forming the real image.

In analog holography, the recording medium is usually a photographic plate, providing linear relationship between the incident light intensity and the amplitude of the transmitted wavefield after development [100]:

$$t(x,y) = t_{offset} + \gamma\left(\left|\underline{E_o}\right|^2 + \underline{E_R}^* \underline{E_o} + \underline{E_R E_o}^*\right) \quad (3)$$

where γ and t_{offset} are constants, determined by the photographic material and the chemical development. The parameter t_{offset} in the equation incorporates the mostly uniform intensity of the reference wave $\left|\underline{E_R}\right|^2$. Thus, the amplitude transmission of the photographic plate is proportional to

complex fields $\underline{E_R}^* \underline{E_o} + \underline{E_R E_o}^*$ after development. Figure 2.1 b) shows a digitally recorded hologram, with the inset providing a zoomed image of the object and reference wave's interference fringes.

Placing the developed photographic plate back to its original place and illuminating it using the original reference wave (now recognized as the reconstruction wave) results in the reconstructed field:

$$\underline{E_T(x,y)} = \underline{E_R(x,y)} \cdot t(x,y) \tag{4}$$

transmitted through the plate. After multiplication, the resulting transmitted field can be written in the following format, omitting the (x, y) notation of spatial dependence for simplicity.

$$\underline{E_T} = t_{off}\underline{E_R} + \gamma \underline{E_R} \left|\underline{E_O}\right|^2 + \gamma \underline{E_R E_R}^* \underline{E_O} + \gamma \underline{E_R E_R E_O}^* \tag{5}$$

Out of four distinctive terms in the previous equation, the first and the second are not of interest, as they are proportional only to the $\underline{E_R}$ complex field. The term $\gamma \underline{E_R E_R}^* \underline{E_O}$ can be expressed as $\gamma \left|\underline{E_R}\right|^2 \underline{E_O}$ which, disregarding the constant $\gamma \left|\underline{E_R}\right|^2$ replicates the original complex object field. The final term $\gamma \underline{E_R E_R E_O}^*$, known as the object's twin image does not replicate the conjugated object field $\underline{E_O}^*$ properly, as the presence of the product $\underline{E_R E_R}$ distorts it. It is usually out of focus, when the third term is in focus. It is the third term, proportional to the original object field that gives the observer, looking through the plate, an impression of the presence of the original object (in our case the duckling), even after the object has been moved. Figure 2.1 c) illustrates the reconstruction process, using the original reference wave to reconstruct the object field. The first, the second and the fourth term in the previous equation represent unwanted, disruptive distortions in the reconstruction, and their spatial separation from the reconstructed object wavefield is usually necessary.

The alternative approach to object reconstruction, shown in Figure 2.1 d) assumes the use of a conjugated reference wave as the reconstruction wave. The terms of the transmitted field are then expressed using the following equation.

$$\underline{E_T} = t_{off}\underline{E_R}^* + \gamma \underline{E_R}^* \left|\underline{E_O}\right|^2 + \gamma \underline{E_R}^* \underline{E_R}^* \underline{E_O} + \gamma \underline{E_R}^* \underline{E_R E_O}^* \tag{6}$$

It is the fourth term of the equation that is to a constant term $\gamma \left|\underline{E_R}\right|^2$ proportional to the conjugated object field $\underline{E_O}^*$, while the twin image and the other two terms degrade the quality of the reconstruction.

In the original Gabor hologram, the object and the reference waves were colinear (in-line), resulting in all four reconstruction terms overlapping at the center of the obtained image. Another approach, widely known today as an "off-axis" approach, was demonstrated by Leith and Upatnieks [108]. In their experiment, the aforementioned waves were set at an angle θ to one another, resulting in a reconstruction in which the first and the second term occupied the central part, while the third and the fourth terms (the object and the twin image) occupied different sides of the reconstructed field. The frequencies of interference fringes in off-axis holograms are naturally higher compared to their in-line counterparts. Larger angles θ provide better image separation, increasing the fringe frequency. This phenomenon does not have much effect when high resolution photographic materials are used for hologram recording. However, limited resolution of today's available imaging sensors imposes a constraint on θ in digital holography, to be discussed in the following text.

2.2 Digital holography

Even though the previous analysis relies on analog holographic principles to intuitively illustrate the recording and reconstruction of holograms, the field of digital holography is predominantly used in most of the recent studies. Digital holograms are recorded using CCDs and CMOS imaging sensors without objective lenses. The sensor itself is illuminated with an interference pattern of the reference and object waves, recording its spatial distribution, usually with 8 to 12-bit resolution. The spatial sampling of the interference pattern is determined by the pixel pitch of the sensor Δx_1 and Δy_1 in two dimensions. Finally, the reconstruction is conducted in the digital domain using numerical approaches describing the diffraction of a reconstruction wave as it propagates after being numerically "illuminated and transmitted" through the recorded hologram.

To describe the near-field diffraction of light, the secondary spherical waves of the Fresnel-Kirchhoff formula originating from the Huygens-Fresnel principle can be approximated using parabolic wavefronts, yielding the Fresnel diffraction integral in its convolution form [101]:

$$E_2(x_2, y_2) = \frac{e^{ik}}{i\lambda z} \iint_{-\infty}^{\infty} E_1(x_1, y_1) e^{\frac{i\pi}{\lambda z}[(x_2-x_1)^2+(y_2-y_1)^2]}\, dx_1 dy_1 . \quad (7)$$

In Equation (7), $E_1(x_1, y_1)$ is the complex electric field of the reconstruction wave right after being transmitted through the plane of the hologram (denoted by coordinates (x_1, y_1)), while $E_2(x_2, y_2)$ is the complex electric field of the reconstruction wave, after propagating the distance z to the object image plane (denoted by coordinates (x_2, y_2)). The wavelength of light used for reconstruction is indicated by λ. After leaving only (x_1, y_1) dependent variables under the integral, the same Fresnel diffraction formula can be expressed in another common form, known as the Fourier form [101]:

$$E_2(x_2, y_2) = \frac{e^{ikz}}{i\lambda z} e^{i\frac{k}{2z}(x_2^2+y_2^2)} \iint_{-\infty}^{\infty} \left\{ E_1(x_1, y_1) e^{i\frac{k}{2z}(x_1^2+y_1^2)} \right\} e^{-i\frac{2\pi}{\lambda z}(x_2 x_1 + y_2 y_1)} dx_1 dy_1 \quad (8)$$

where the wave number $k = 2\pi/\lambda$ is introduced for convenience. In both forms of the same integral, E_1 can be numerically obtained by a multiplication of the recorded hologram (matrix) with the mathematical model of the reconstruction beam. In case of a spherical reference wave, the decrease in amplitude with increase in radius from the wave's point source can be neglected over the hologram plane, leaving only the phase dependence in the equation describing the reference wave:

$$E_R(x_1, y_1) = \exp\left(-ik\sqrt{(x_1 - x_0)^2 + (y_1 - y_0)^2 + (z_1 - z_0)^2}\right). \quad (9)$$

Parameters x_0, y_0 and z_0 represent the coordinates of the wave's point source. In the case of a plane reference wave, both the amplitude and phase of the wave don't exhibit spatial dependence over the hologram plane, deeming the multiplication unnecessary.

The numerical reconstruction process of a digitally recorded hologram of a duckling from Figure 2.1 a) is depicted in Figure 2.2.

Even though both the convolution and the Fourier form of the Fresnel diffraction integral represent the same equation, numerical approaches in solving them differ in complexity, and applications. The former can be calculated using the expression:

$$E_2(x_2, y_2) = \frac{e^{ikz}}{i\lambda z} \mathcal{F}^{-1}\left\{ \mathcal{F}\{E_1(x_1, y_1)\} \mathcal{F}\left\{ e^{\frac{i\pi}{\lambda z}(x_1^2+y_1^2)} \right\} \right\} \quad (10)$$

while the latter can be expressed using only one Fourier transform:

$$E_2(x_2, y_2) = \frac{e^{ik}}{i\lambda z} e^{i\frac{k}{2z}(x_2^2+y_2^2)} \mathcal{F}\left\{E_1(x_1, y_1) e^{i\frac{k}{2z}(x_1^2+y_1^2)}\right\}. \quad (11)$$

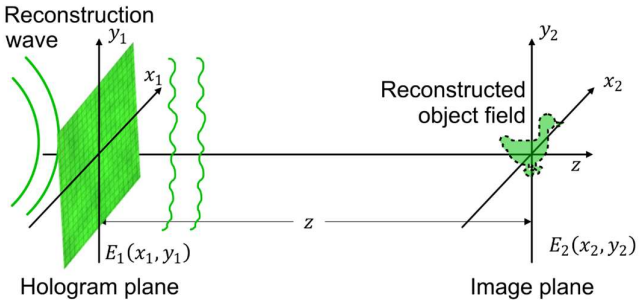

Figure 2.2 The numerical reconstruction process of a digitally recorded hologram. The light is diffracted from the hologram plane, resulting in a complex object field at the image plane.

In Equations (10) and (11), $\mathcal{F}\{\}$ and $\mathcal{F}^{-1}\{\}$ denote the Fourier transform and the inverse Fourier transform, respectively. Treating the Equation (7) integral as a convolution, the expression $\mathcal{F}\left\{e^{\frac{i\pi}{\lambda z}(x_1^2+y_1^2)}\right\}$ is regarded as the Fourier transform of the impulse response, which can be calculated analytically. Thus, the approach of Equation (10) does not require three, but two Fourier transforms.

To numerically solve the expressions of Equations (10) and (11) for discrete values acquired by the image sensor, the easiest way is to apply the well-known Fast Fourier Transform (FFT) algorithm [109], reducing the calculation complexity and time.

The main difference between the two described methods is the size of the reconstructed object field. With the convolution method the sampling between the points (pixels) in the reconstructed field is the same as the sampling of the original hologram ($\Delta x_2 = \Delta x_1$, $\Delta y_2 = \Delta y_1$) making it easily applicable to in-line holographic recording of objects with dimensions less than the dimensions of the imaging sensor. Contrary to that, the sampling ($\Delta x_2, \Delta y_2$) in the reconstructed object field calculated using the Fourier form of the Fresnel diffraction integral is determined by equations:

$$\Delta x_2 = \frac{z\lambda}{N\Delta x_1}$$
$$\Delta y_2 = \frac{z\lambda}{N\Delta y_1} \quad (12)$$

where N is the number of pixels of the hologram, making the resolution of the obtained reconstructions dependent on recording parameters z, λ and N.

Finally, when designing an off-axis holographic setup, the experimenter should keep in mind that the angle between the object and the reference wave should be small, limited by the resulting fringe frequency f to satisfy the sampling theorem with the available imaging sensor:

$$f < \frac{1}{2\Delta x_1}. \quad (13)$$

This restriction translates to the minimum distance between the object with a dimension d_0, and the imaging sensor with a pixel pitch Δx_1 to obtain a small enough angle between the waves. A rule of thumb in practice is given by equation [101]:

$$z > d_0 \frac{\Delta x_1}{\lambda}. \quad (14)$$

A reconstruction of a digital hologram from Figure 2.1 b) using the Fourier form of the Fresnel diffraction integral is shown in Figure 2.3. Both the hologram and the reconstruction are 2048 by 2048 pixels images. The hologram has a pixel pitch of 3.45 μm, while the reconstruction has a pixel distance of 22.6 μm. The recorded object is a logo of the University of Belgrade, School of Electrical Engineering, visible on the far right in the reconstruction. Beside the object, the reconstruction contains two more distinguishable bright regions. The so-called DC term is located in the center of the image. It contains the first and the second term of Equation (5). The physical interpretation of the DC term is that it is the zeroth diffraction order, and that it essentially represents the reconstruction beam, illuminating the hologram, visible to the observer looking through the hologram. The final bright region is the twin image, located symmetrically to the object with respect to the DC term. It resembles the object image, though it is out of focus, and distorted.

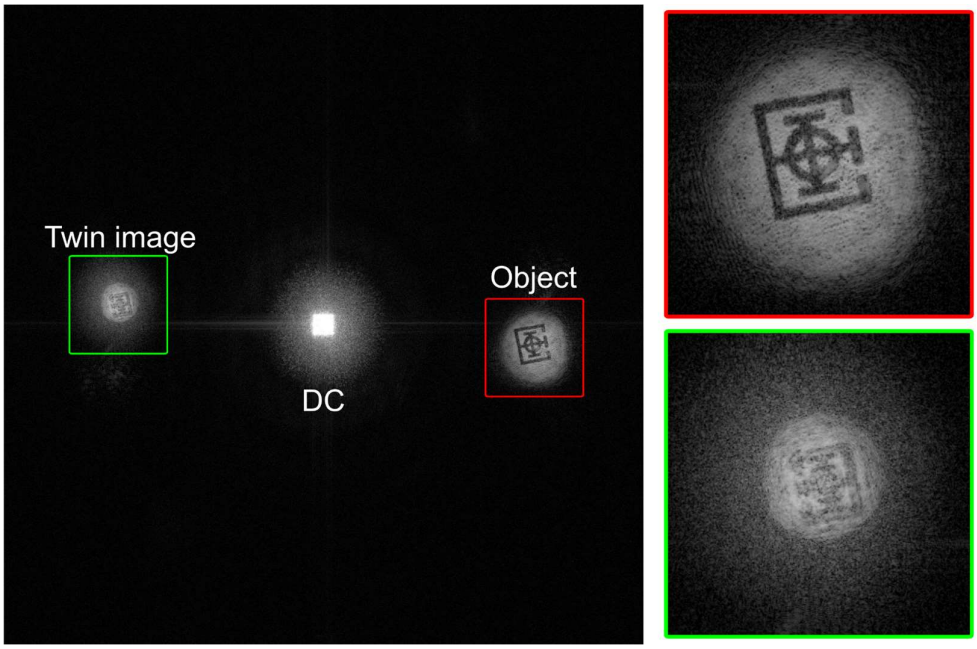

Figure 2.3 An intensity image of a digital hologram (shown in Figure 2.1 b)) reconstruction obtained using a Fourier form of the Fresnel integral. The reconstruction shows the logo of the University of Belgrade, School of Electrical Engineering. Image dimensions are 2048 by 2048 pixels. Zoomed regions with the object and twin images are shown on the right. Their image planes are separated, which is why only one of them is in focus.

Both the convolution and the Fourier form of the Fresnel diffraction integral suffer from a fixed sampling distance $(\Delta x_2, \Delta y_2)$ of the reconstructed field. The object is also moved out of the image center due to the off-axis nature of the hologram recording. To remedy the outlined problems, multiple shifting and scaling algorithms were proposed [101,110–112]. The one, extensively used in this thesis is the Shifted-Fresnel reconstruction method, allowing for both the scale and the shift operation of the object field [111,112]. The convolution form of the Fresnel diffraction integral is modified, changing the expressions $(x_2 - x_1)^2$ and $(y_2 - y_1)^2$ by introducing the shifts a_x and a_y and scaling the coordinates by a factor of s in the image plane, instead of the hologram plane which was derived in literature [111].

$$\begin{aligned}(sx_2 - x_1 + a_x)^2 &= s(x_2 - x_1)^2 + x_2^2(s^2 - s) + x_1^2(1 - s) + a_x^2 + 2sx_2a_x - 2x_1a_x \\ (sy_2 - y_1 + a_y)^2 &= s(y_2 - y_1)^2 + y_2^2(s^2 - s) + y_1^2(1 - s) + a_y^2 + 2sy_2a_y - 2y_1a_y\end{aligned} \quad (15)$$

Returning the expressions of Equation (15) into the convolution form of the diffraction integral, along with the following factors:

$$C_z = \frac{e^{ikz}}{i\lambda z} \cdot e^{\frac{i\pi}{\lambda z}\left((s^2-s)(x_2^2+y_2^2)+a_x^2+a_y^2+2s(x_2a_x+y_2a_y)\right)}$$
$$e^{i\phi_u} = e^{\frac{i\pi}{\lambda z}\left((1-s)(x_1^2+y_1^2)-2(x_1a_x+y_1a_y)\right)} \quad (16)$$
$$e^{i\phi_h} = e^{\frac{i\pi}{\lambda z}s(x_1^2+y_1^2)}$$

introduced for convenience, the final form of the Shifted-Fresnel reconstruction method can be expressed as:

$$E_2(x_2, y_2) = C_z\mathcal{F}^{-1}\left\{\mathcal{F}\{E_1(x_1, y_1) \cdot e^{i\phi_u}\}\mathcal{F}\{e^{i\phi_h}\}\right\}, \quad (17)$$

and implemented using the FFT algorithm.

A reconstruction of a digital hologram from Figure 2.1 b) using the Shifted-Fresnel reconstruction is shown in Figure 2.4. A scale factor $s = 1.5$ and offsets $a_x = -2950\ pix$ and $a_y = -300\ pix$ resulted in an image of the recorded object centered in the image plane with a pixel distance of $5.18\ \mu m$, more than 4 times smaller than the pixel distance obtained using the Fourier form of the diffraction integral.

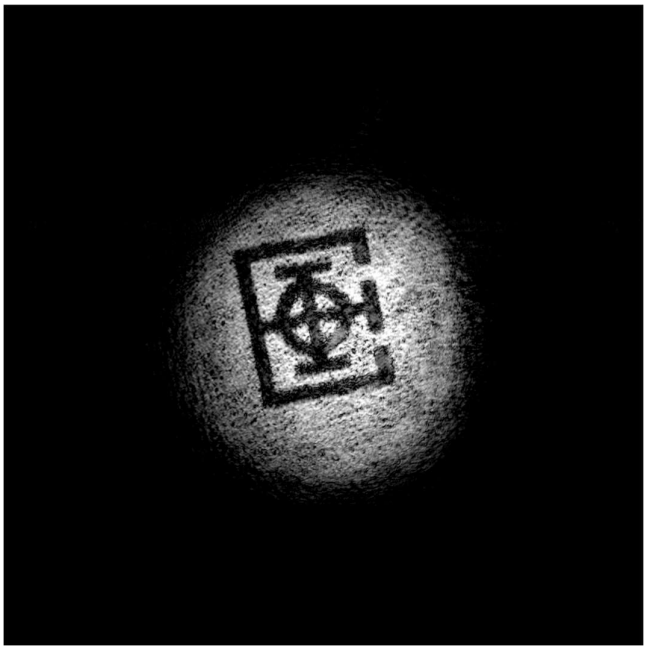

Figure 2.4 An intensity image of a digital hologram (shown in Figure 2.1 b)) reconstruction obtained using the Shifted-Fresnel reconstruction method. The reconstruction shows the logo of the University of Belgrade, School of Electrical Engineering. Image dimensions are 2048 by 2048 pixels.

The nature of off-axis holography ensures separation of the object, its twin image, and the DC term in the reconstruction plane. If separation is not sufficient, improvements in its quality are achievable through DC term and twin image suppression. Over the years, many techniques were proposed to facilitate this requirement, overview of which can be found in holography textbooks [101,102,111]. In this thesis, the DC term is suppressed using one such approach in which the illuminated hologram is filtered using the moving average filter, and the filtered image is subtracted from the original. When required, the twin image is filtered using a mask in the frequency domain of the illuminated hologram [101].

The intensity images of the reconstructed fields of this thesis are not presented in their raw, original form. Instead, they are logarithmically transformed to be easily interpreted, mimicking the

operation of the human eye. A typical raw intensity image with its histogram is shown in Figure 2.5 a). Using a logarithmic function of the raw intensity I, I_{log} is calculated:

$$I_{log} = \log_2(1 + I) \tag{18}$$

emphasizing the object part of the reconstruction, as shown in Figure 2.5 b). The number 1 is added to the intensity to ensure non-zero values in the logarithm. The MATLAB code for digital hologram reconstruction using the Fourier form of the Fresnel integral, with the zero order and twin image filtering, is presented in detail in Appendix A. It is provided as a starting point, while codes applying other discussed reconstruction methods and digital holographic interferometry are omitted to avoid unnecessary clutter.

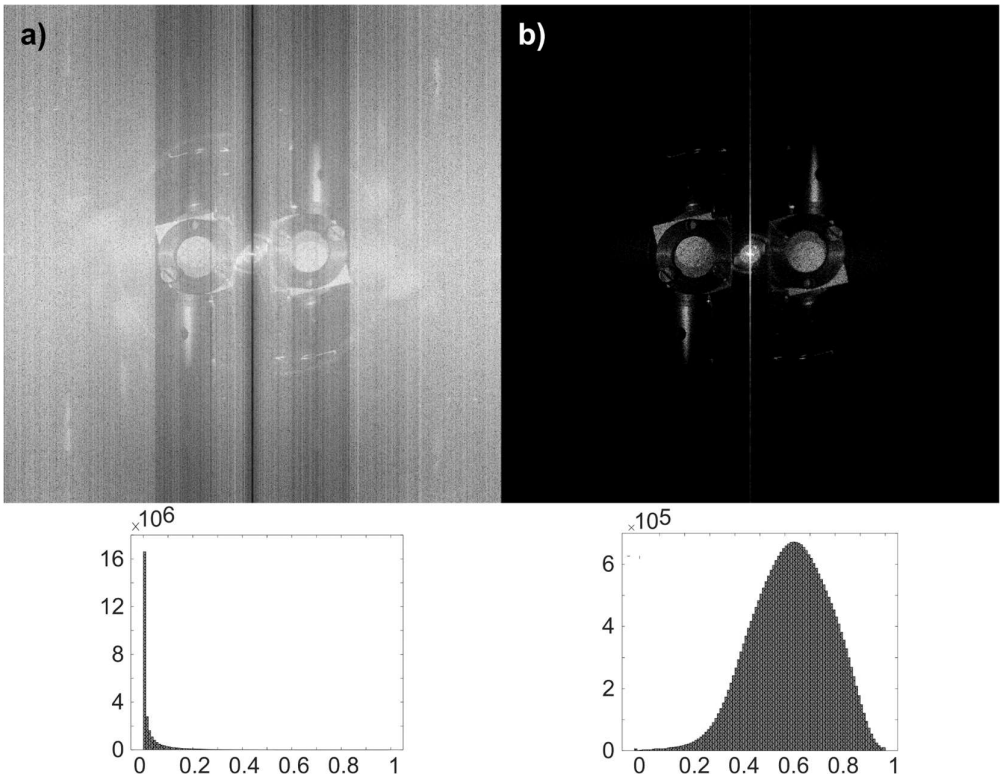

Figure 2.5 Reconstructed hologram intensity images of a mounted *Morpho* butterfly wing sample: a) raw: b) processed using Equation (18); with the corresponding histograms.

2.3 Digital holographic interferometry

Some of the most useful benefits of the holographic method are accessible through the light's phase information provided within the reconstructed object field. The phase is extremely sensitive to changes in the refractive index of materials, or displacements and deformations of the objects reflecting light. Thus, comparing the phases of successive holographic recordings enables very precise displacement and deformation measurements. Such measurements make a foundation of the field known as the digital holographic interferometry (DHI). An illustration of the process of DHI application to displacement measurement of an object (a duckling from previous examples) is shown in Figure 2.6. Two holograms are recorded, one before, and the other after the displacement occurred. From the reconstructed fields, phase information is acquired using expressions:

$$\varphi_1 = atan\left\{\frac{Im\{E_2(x_2,y_2)\}}{Re\{E_2(x_2,y_2)\}}\right\}$$
$$\varphi_2 = atan\left\{\frac{Im\{E_2'(x_2,y_2)\}}{Re\{E_2'(x_2,y_2)\}}\right\}. \quad (19)$$

By subtracting the phases, phase difference induced by displacement is obtained and calculated using the expression [101]:

$$\Delta\varphi = \varphi_2 - \varphi_1 = \vec{d}\cdot\vec{e} = \frac{2\pi}{\lambda}d(1+cos\,\theta), \quad (20)$$

where $\vec{d}$ and $\vec{e}$ are the displacement and sensitivity vectors, respectively, and θ is the angle between the wave illuminating the object, and the wave reflected from the object to the imaging sensor (illustrated in Figure 2.6 a)).

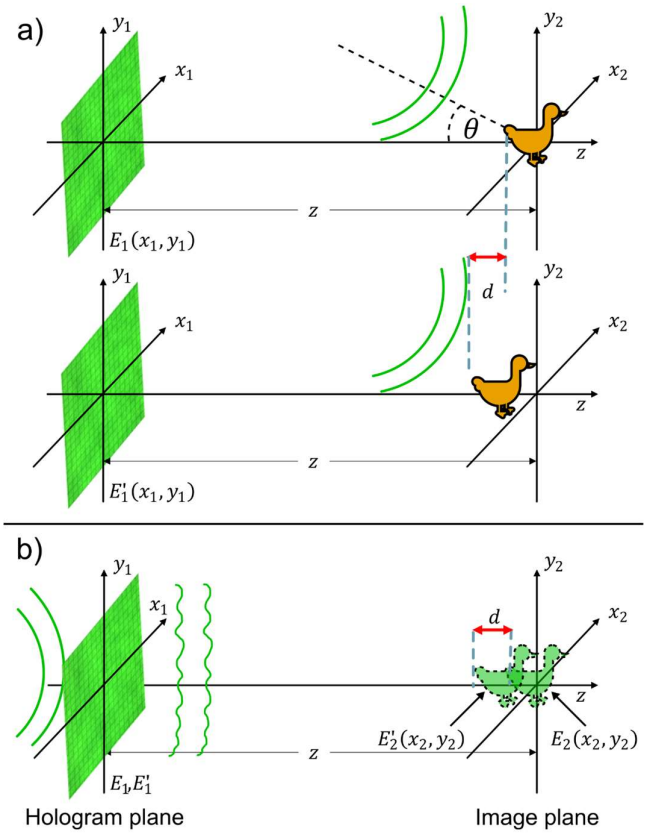

Figure 2.6 Digital holographic interferometry: a) Recording of two successive holograms; b) Differences between the two reconstructions.

The $atan()$ function of Equation (19) returns a 2D phase matrix, limited to values between $-\pi$ and $+\pi$. Through subtraction of Equation (20), the difference in phases can take values between -2π and $+2\pi$. An alternative route would be to find the phase difference by finding the argument of the complex matrix of a point wise division of $E_2'(x_2,y_2)$ and $E_2(x_2,y_2)$:

$$\Delta\varphi = atan\left\{\frac{Im\left\{\frac{E_2'(x_2,y_2)}{E_2(x_2,y_2)}\right\}}{Re\left\{\frac{E_2'(x_2,y_2)}{E_2(x_2,y_2)}\right\}}\right\}, \quad (21)$$

limiting $\Delta\varphi$ between $-\pi$ and $+\pi$. The introduced limit of $\Delta\varphi$ between $-\pi$ and $+\pi$ comes with an expected consequence. If the observed physical change is to induce a phase change higher than $+\pi$ or lower than $-\pi$, the phase would appear to wrap, exhibiting a jump of -2π or $+2\pi$ respectively, staying within the limits imposed by the mathematics.

An example of a phase difference image is shown in Figure 2.7 a). The phase wrapping is expressed by an abrupt color change from dark red $(+\pi)$ to dark blue $(-\pi)$ as the phase difference increases going inwards. The unwrapping of the phase seems like an easy task to a novice holographer. However, the influence of noise makes the task much harder to perform, inspiring a large amount of effort towards robust two-dimensional phase unwrapping techniques in the past decades [113–117]. The problem of phase unwrapping may ultimately be solved if the sampling time T of the recording is small enough to prevent the phase from wrapping between the successive holograms (i and $i+1$):

$$\left|\varphi_{(i+1)\cdot T} - \varphi_{i\cdot T}\right| \leq \pi. \qquad (22)$$

The phase change can be obtained at any instant by a summation of the previous incremental phase changes. This approach is known as temporal phase unwrapping [101].

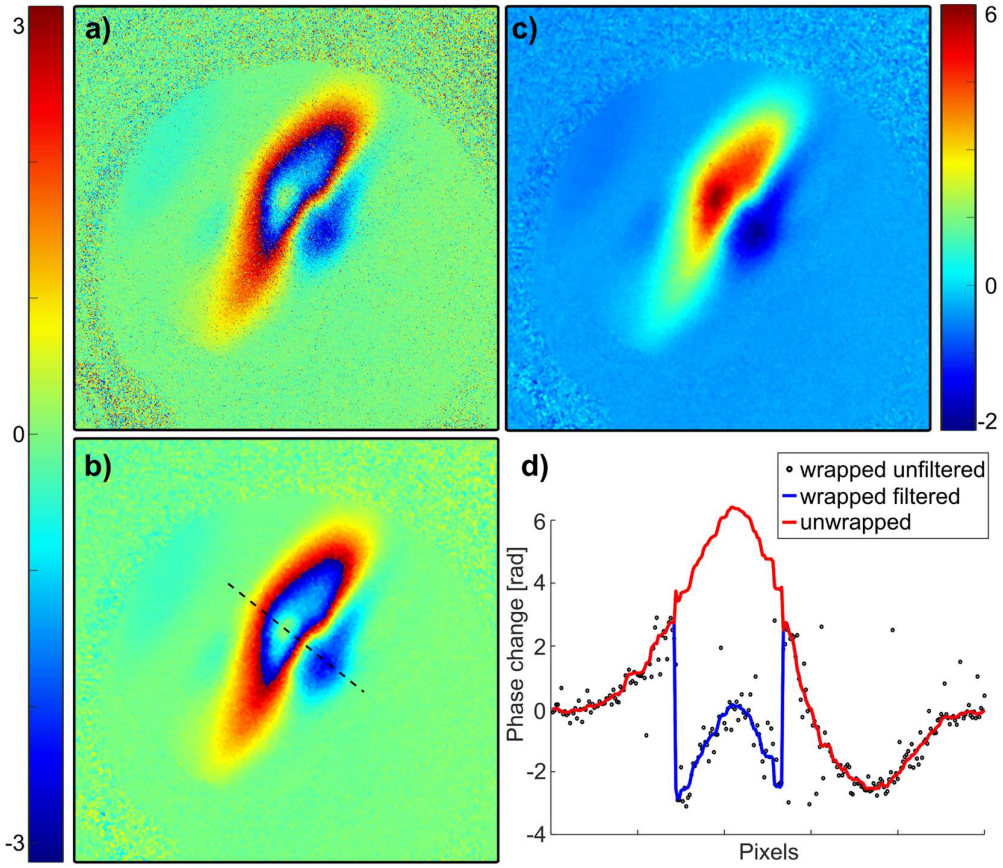

Figure 2.7 a) A raw phase difference image showing light induced displacements on a wing sample presented in Figure 2.5; b) The same image after filtering; c) The unwrapped phase; d) A phase profile along the dashed line shown in b).

The phase difference shown in Figure 2.7 a) is riddled with noise, as most experimentally obtained holographic recordings are. The origin of noise in digital holography is bipartite. There is the noise commonly termed as "technical", inherent to all digital light detecting systems. It is comprised of shot, electronic and quantization noise. Unlike conventional imaging, the coherent

nature of holography brings with it another undesirable noise source known as the laser speckle. Reducing noise in holographic intensity and phase recordings has been a subject of research for many years. While using white light holography provides inherent noise suppression, the toll of the complicated setups is often too heavy. Thus, researchers frequently resort to filtering algorithms known from conventional digital image processing. For example, median filtering with different sized kernels ranked quite high in performance, even compared to techniques developed specifically for filtering of holographic recordings [118]. The two-dimensional phase maps with values in radians are pseudo-colored using a jet colormap available in MATLAB.

However, the holographer must be careful when low pass filtering a noisy phase wrapped image. Reducing the noise may in turn degrade the distinctive 2π jump, lowering the chances of a successful phase unwrap. One approach to preserve the jump advises to abstain from filtering the phase difference image directly. Instead, it suggests to first calculate the sine and cosine of the phase removing the jumps, filter the calculated matrices separately, and then obtain the filtered phase by using the $atan()$ function once again [119].

$$\Delta\varphi_{filt} = atan\left\{\frac{median\_filter(\sin(\Delta\varphi))}{median\_filter(\cos(\Delta\varphi))}\right\}, \quad (23)$$

The outlined approach was implemented to filter the phase from Figure 2.7 a) using a median3x3 filter on the sine and cosine matrices, after which the median5x5 filter was used to further denoise the phase difference. The results of this filtering procedure are presented in Figure 2.7 b). A demonstration of a phase unwrapping algorithm presented in [117] resulted in an unwrapped phase shown in Figure 2.7 c). Finally, raw, filtered and unwrapped phase profiles along the dashed line of Figure 2.7 b) are presented in Figure 2.7 d) for comparison.

2.4 Holographic microscopy

The origins of holography are strongly rooted in the requirements of the field of microscopy. Thus, it is not unexpected to find many microscopic applications of the outlined holographic principles. Demonstrated approaches of holographic microscopy vary. However, based on the magnification mechanism they utilize they can roughly be divided into two categories. One category covers all holographic setups, constructed using microscope objectives (MO) and magnification lenses in general [101,120,121]. The other is comprised of different lensless approaches, using diverging beams as the origin of magnification [107,122–124]. While other types of categorizations exist, that divide the approaches by the recording geometry – in-line/off-axis, or – reflective/transmissive, they are general to all holographic recordings, not just microscopy.

Using the MO to magnify the imaged object field does not influence the holographic process greatly. While the recording remains unchanged, the reconstruction requires the user to adapt the distance z in order to focus not onto the plane of the originally recorded object, but onto the plane of its image, formed by the MO. The limitations imposed by the MO in classical optical microscopy, such as unavoidable aberrations, limited numerical aperture, depth of field and field of view are all present in holographic recordings as well.

The lensless approach offers great advantages in reduced price and complexity of the optical setups, compared to setups utilizing MOs. It also provides a large field of view and enables focusing on different parts of the reconstructed field of the imaged three-dimensional objects. However, the price of those benefits is paid through the cumbersome reconstruction procedure. Most of the lensless setups are constructed in an in-line geometry, producing the problem of the overlapping DC term-object-twin image in the reconstruction. Elimination of the parasitic fields in the reconstruction can be accomplished using multiple holographic recordings, recordings of the background etc. However, this increases the recording time, as well as the required computational cost. Other approaches,

iterative in nature, such as the implementation of the Gerchberg-Saxton algorithm (GSA) [125] are also presented [126].

A simple in-line digital holographic microscope♦ is presented in Figure 2.8 [94]. The focusing lens in front of the pinhole only increases the intensity throughput of the pinhole, not influencing the magnification, determined by the distances between the pinhole, the object, and the camera. The details of the setup, its applications, and utilized algorithms for reconstruction are thoroughly discussed in the paper [94].

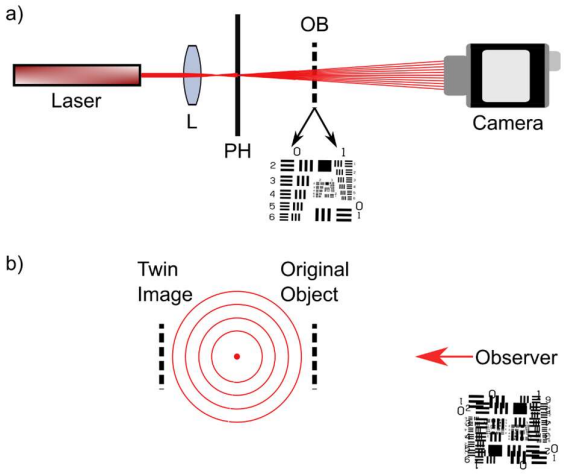

Figure 2.8 a) A simple lensless digital holographic microscope (without a microscope objective). L-Lens; PH – Pinhole; OB – Object. b) Reconstruction of the object field, showing the overlapping object and twin images.

The reconstruction algorithms based on the Fresnel integral fail to present useful results in these kinds of setups, due to the very short propagation distances which impose limitations on the introduced paraxial approximation. In order to implement the GSA, diffraction calculation is usually conducted using another approach with no inherent approximations to the diffraction integral, useful for short propagation distances, known as the Angular Spectrum Method [101,111,112,127].

♦ The optical setups in this thesis are drawn using the Ray Optics extension in Inkscape [161].

Chapter 3. Materials and sample preparation

The investigation of imaging capabilities of holographically interrogated *Morpho* butterfly wings was performed on a *Morpho didius* species of the *Morpho* butterfly genus [128]. *M. didius* is recognizable by its vivid blue color, originating not only from the interferometric reflection but from diffraction and significant absorption as well [75]. Strong reflection in the blue-green part of the spectrum ensures the quality of the holographic recording using a laser with a $532\ nm$ wavelength. Together with the significant absorption in red, ultraviolet (UV), and NIR parts of the spectrum, this makes the chosen species of *Morphos* a very good candidate for the experiments of this thesis.

A photograph of a *M. didius* with two out of four wings attached is shown in Figure 3.1 a) and b). Both the iridescent blue and the non-iridescent brown side of the wings are shown.

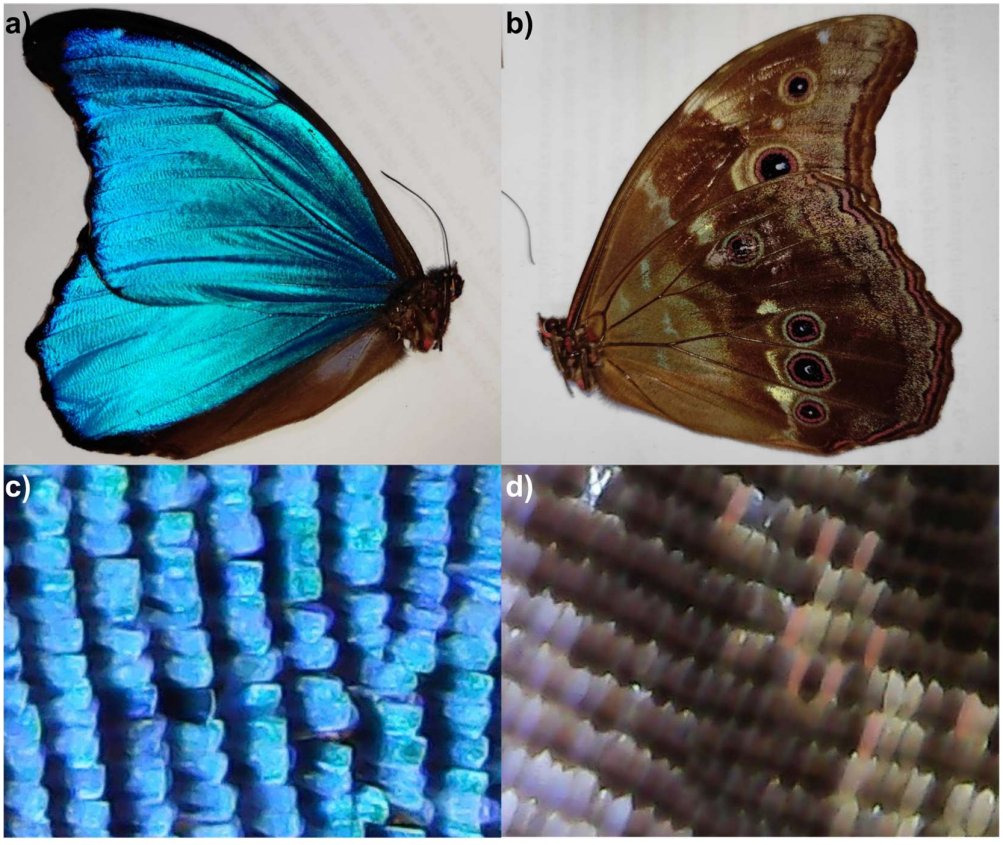

Figure 3.1 a) A photograph of *M. didius* – iridescent (dorsal) side; b) A photograph of *M. didius* – non-iridescent (ventral) side; c) A microscopic image of the iridescent scales; d) A microscopic image of the non-iridescent scales.

The wings of butterflies are made up of two membranes, permeated with the wing veins. The veins are mechanically supporting the membrane, thus constricting its movements. The membrane is covered with wing scales to which all of the *Lepidoptera* owe their name. Different butterflies evolved different colorations and motifs on the upper and lower wing sides, usually for the purpose of diverting predators, or attracting the opposite sex. The scales of butterflies can be divided into cover scales and ground scales, based on their location (the top or the bottom scale layer). Depending on the species, either cover scales or ground scales are responsible for the structural coloration. In the case of *Morphos* it is the ground scales that produce the blue on the upper (dorsal) side, while the cover scales are mostly translucent. The scales on the lower (ventral) side of the wing membrane are usually highly pigmented and non-iridescent [129]. The scales are flat in appearance and ordered in overlapping rows, as visible in an optical microscopic image shown in Figure 3.1 c) and d) respectively.

The size of the wing scales varies from species to species. For the *Morphos* the scale dimensions found in literature are on the order of $200 \times 100\ \mu m$ [81,130]. The scales are not parallel to the membrane surface. Instead, they make a small sharp angle with the membrane, to which they are connected by a peduncle. While the outer surface of the scales is covered with $\sim 2\ \mu m$ spaced ridges of Christmas tree multilayered structures, the lower surface is flat. An illustration of the wing scales positioned on the membrane is shown in Figure 3.2 a). The Christmas tree structures producing the interferometric reflection are illustrated in a single scale cross-section shown in Figure 3.2 b).

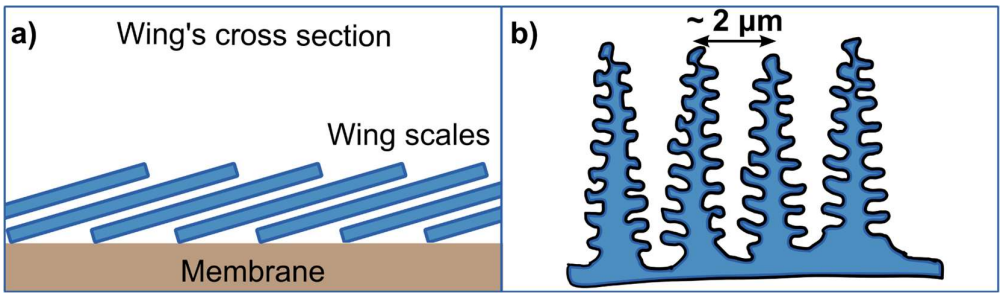

Figure 3.2 Illustrations of the *M. didius* a) wing's cross section (dorsal scales) b) Christmas tree structures (ridges cross section). The second illustration is based on a SEM image published in [81].

Reconstructed intensity and phase images of the *M. didius* wing scales recorded using a holographic microscope presented in Figure 2.8 are shown in Figure 3.3 a) and b), respectively. The Figure shows two differently shaped scales, with visible longitudinal ridges. The observed dimensions of the scales match the literature. The holographic imaging of the scales, still attached to the membrane, is achievable only in reflective holographic microscope geometry. The example of an intensity image of a reconstructed hologram is presented in Figure 3.3 c). The hologram of the scales attached to the membrane is recorded using a Mach-Zehnder-like holographic setup further described in Section 4.1, modified to incorporate a MO in the object path.

3.1 Preparation procedures

To prepare a wing sample for the holographic interrogation, a part of the wing must be cut, without damaging the scales, or disrupting their fragile attachment to the membrane. The first attempts to cut the wing using sharp circular punching knives proved to be suboptimal, as the wing often wrinkled and tore during the process. To avoid this type of damages, CO_2 laser was used for precise cutting. During the cutting procedure, the protective air stream of the laser was turned off to avoid damaging the sample.

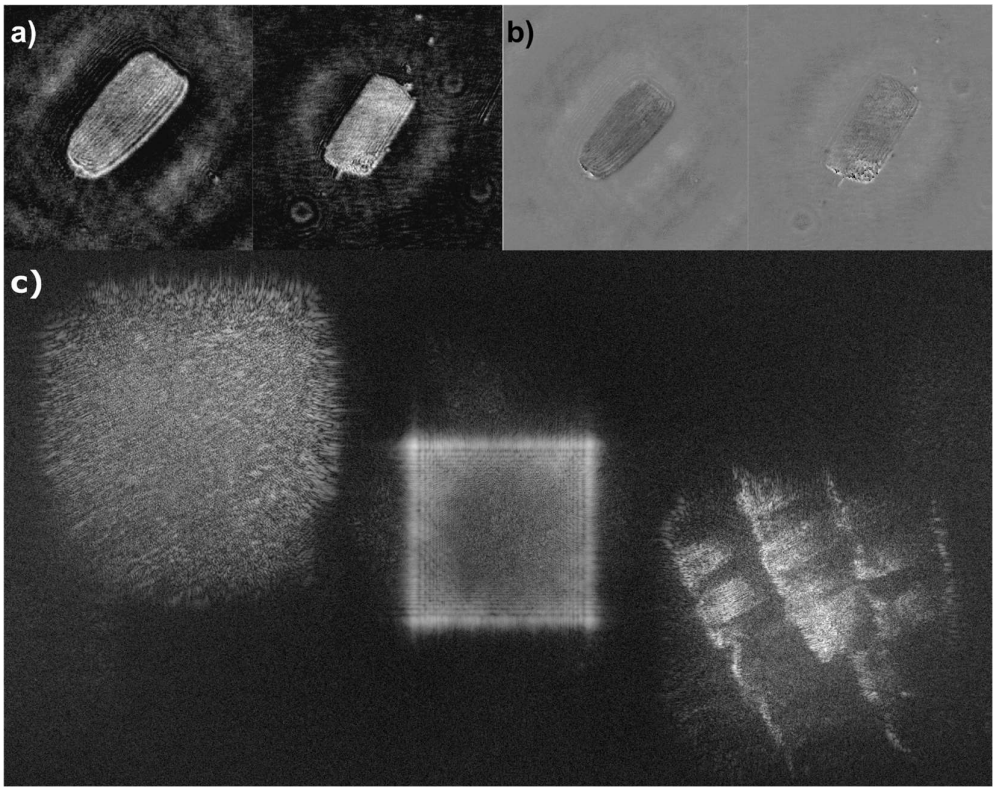

Figure 3.3 Reconstructed images a) intensity; b) phase; of two different types of scales of a *M. didius* butterfly, acquired using a digital holographic microscope shown in Figure 2.8. c) Reconstructed intensity image of the scales attached to the wing using a reflective holographic microscope (a Mach-Zehnder-like holographic setup further described in Section 4.1, modified to incorporate a MO in the object path).

The size and shape of the sample to be cut was chosen based on the position of the wing veins. Avoiding the veins proved to be important in improving the overall response of the designed sensor. The presence of veins in the sample constricted the movement of the surrounding membrane in response to radiation, thus resulting in membrane counter-bending and holographic response of the non-illuminated areas. The examples of this unwanted effect will be demonstrated and discussed further in the following chapters. The space between the veins was limited, thus yielding the circular samples of $5 - 10\ mm$ in diameter. The process of cutting the wing using a CO_2 laser is shown in Figure 3.4 a), while Figure 3.4 b) shows the prepared circular samples next to the wing with holes.

During the research, another approach was attempted, where instead of one larger circular sample, a higher number of small rectangular samples were cut from the wing. This provided the opportunity to test the response of the scales to light, without the membrane interconnection between a large number of scales. Figure 3.4 c) shows the photograph and the microscopic image of the aforementioned rectangular samples, respectively. The microscopic image shows ~ 5 rows of wing scales inside of the rectangular samples, which corresponds to the scale – sample dimensions. The laser induced severe burning of the scales is visible near the sample edges.

After cutting the sample, it was necessary to mount it to the aluminum holder using an adhesive material. The material was chosen to provide a good sample to mount adhesion over the whole sample area. Otherwise, unwanted membrane movement was observed. The main adhesive material used in this thesis was a uniform layer of beeswax deposited on a plastic strip. The sample was placed on the strip with wax, while the strip was adhered to the aluminum mount using a piece of double adhesive tape, as shown in Figure 3.4 d).

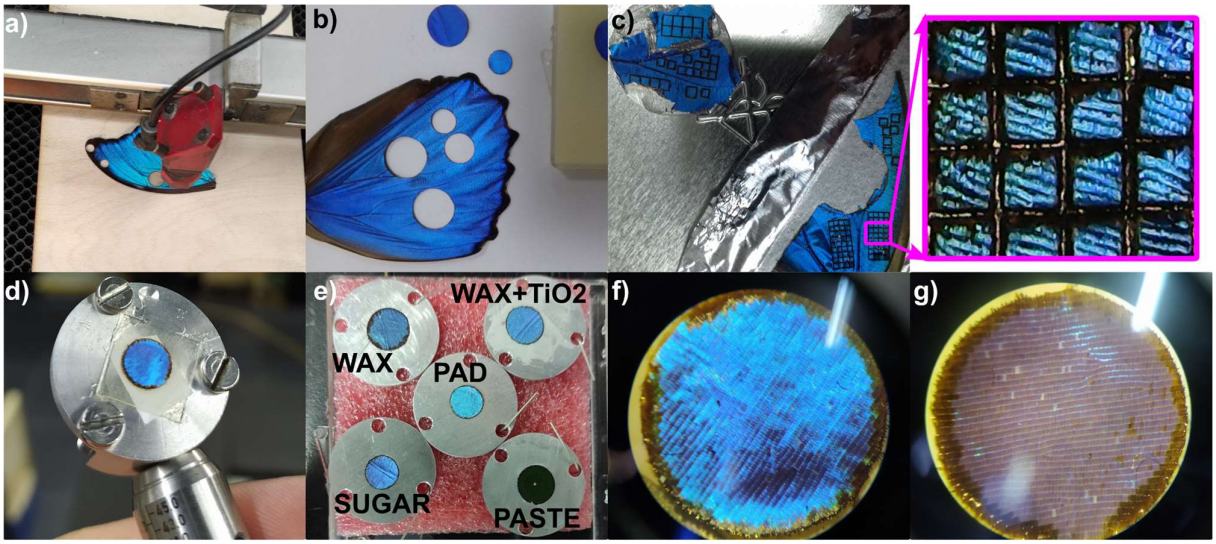

Figure 3.4 a) Cutting of the wing using a CO_2 laser; b) Circular samples cut from the wing; c) A group of rectangular samples cut from the wing, and a microscopic image of the 1 mm rectangular samples; d) A circular sample mounted on an aluminum mount using a plastic strip with wax and a double adhesive tape; e) Samples using different adhesive materials; f) A microscopic photograph of a circular sample rotated to achieve strong reflection; g) A microscopic photograph of a rotated weakly reflecting circular sample.

To investigate the influence of the adhesive material on the cooling, and consequently temporal response of the proposed sensor, a sample with the reduced thickness of wax without the plastic strip was prepared. Other tested adhering materials were wax with TiO_2, double adhesive heatsink pad commonly used in electronics with a thermal conductivity of $240\ W/mK$, and a saturated sugar solution. Using thermal paste to attach the sample to the mount was also attempted. Even though the wing is hydrophobic, the capillary action of the wing scales resulted in thermal paste filling the air gaps on the dorsal side of the wing as well, destroying the iridescence. Prepared samples are shown in Figure 3.4 e). The orientation dependent iridescence under an optical microscope is shown in Figure 3.4 f) and g). As the intensity of light reflected from the sample is dependent on its orientation, careful consideration of the angle of the scales was necessary during mounting for holographic recordings.

Placing the sample to the adhering materials with liquid interface (different types of wax, sugar solution) proved to be easier compared to their counterparts with glue (heatsink pads, double adhesive tapes), due to the capillary action of the ventral wing scales. In the case of wax, a soldering iron was used to heat up the aluminum mount, and consequently melt the wax to improve adhesion. Heatsink pads and double adhesive tape required the sample to be pressed on to the tape, to remove any excess air between the sample and the tape. However, this proved to be difficult, as pressing on the sample would inadvertently damage the scales. To overcome this issue, a technique was devised, in which the sample was first attached to a plastic balloon using static electricity. Then, the balloon was used to gently place the sample onto the tape/pads, providing enough pressure to ensure adhesion, while not damaging the scales.

3.2 Reflection, absorption and transmission measurements

The movement of scales due to heating by absorbed light creates a foundation of the operating principle of the proposed imaging sensor. Furthermore, good reflection, and low absorption and transmission properties are expected at the wavelength of the laser used for holographic interrogation of the sample. Thus, determination of the reflection (R), transmission (T) and absorption (A) curves

of the *M. didius* wing proved vital in the upcoming analysis of sensitivity. Measurement of such spectral properties is nontrivial, as the direct light is diffusely reflected in a large solid angle. The spectral distribution of the reflected light depends on the angles of incidence and observation, due to a multilayered structure on the wing scales [129]. To overcome this issue and obtain the spectral dependence of R, T and A, the use of an integrating sphere was suggested in literature [74,75]. The integrating sphere provides spectral data proportional to the total light level diffusely reflected or transmitted by a biological specimen [131]. From these curves, the absorption curve is found, considering the fluorescence is negligible. The spectral data presented by Kinoshita et al. [74,75] show a distinct blue-green reflection peak. Transmission is negligible at lower wavelengths, increasing rapidly towards the NIR part of the spectrum. The resulting absorption is high near the UV due to melanin, while it shows a minimum at $460\ nm$ and a maximum at $570\ nm$ due to the interferometric effects [74,75]. Analyzing the spectral properties of intact wings, *M. didius* species proves to be favorable for light absorption applications compared to i.e., *M. sulkowskyi* species with higher R and T curves [74], known to be used for MWIR detection [83].

While the results of Kinoshita et al. provide useful information in the visible spectral region, they lack data in the NIR. Furthermore, analysis of these results cannot distinguish between the contributions of different types of scales to the overall R, T and A distributions. To overcome these questions, we measured the diffuse reflectance spectra of an intact *M. didius* wing, and a wing without the scales on the back. The measurement was performed using a reflectance sphere (Edmund Optics RSA-FO-150) for wavelengths ranging from 390 to $1000\ nm$. The transmittance spectra of the same specimens were measured in transmission geometry. The scales were removed from the back surface of the wing by gentle mechanical actions of a soft paint brush. The images of both sides of the modified specimen are shown in Figure 3.5. The iridescent side of the modified specimen appears to be of a lighter blue color, compared to the specimens shown in Figure 3.4. This suggests what will soon be confirmed as less absorption of the colors complementary to blue.

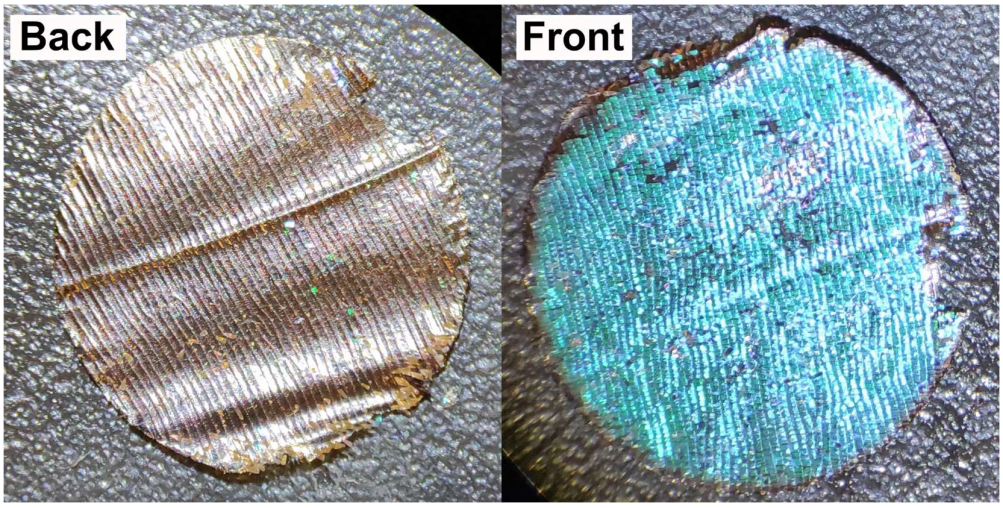

Figure 3.5 An optical microscope image of a sample with the scales from the back side of the membrane removed.

The results of Figure 3.6 show the R, T and A measurements of our samples, both intact and modified. Once again, a distinct interferometric reflectance peak similar to the one observed by Kinoshita et al. dominates the blue-green spectral domain, suggesting the use of a laser in that region for holographic interrogation should result in higher quality holograms. Absorption of the intact specimen exhibits a peak in the orange-red part of the spectrum, and decreases towards the NIR, on the account of increase in both R and T. While the removal of the back scales seems not to affect the reflectance spectra of the iridescent side of the wing greatly, it significantly lowers the absorption of

the specimen in the red to NIR part of the spectrum. This result suggests that the presence of back scales will in fact determine the total absorption, and consequently heating of the wing, influencing the overall light induced displacement together with the scales on the iridescent side.

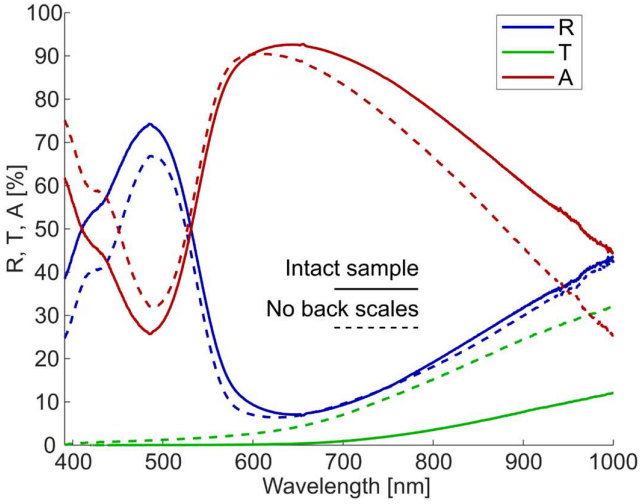

Figure 3.6 Measured reflected, transmitted and absorbed portions of light, incident on a *M. didius* wing. Full lines indicate the measurements for an intact sample, while the dashed lines correspond to the spectral distributions of the wing without the back scales.

Chapter 4. Holographic experiments, custom-designed electronic devices, and software

This Chapter thoroughly describes the utilized methods for holographic and thermographic recordings, used for measurements throughout the rest of the thesis. Two holographic setups and their complementary applications are proposed and discussed. The devised sample mount for back surface temperature control is presented and its functional properties explained. Custom-designed electronic devices for temperature control and laser diode current drive are introduced and described. Finally, the key algorithm design points of the software solutions utilized throughout the experiments are communicated.

4.1 Design of holographic experiments

The design of the main holographic experiment required synchronous monitoring of displacement using DHI and the illumination induced temperature changes using classical thermal imaging (with a commercial thermal camera). The experimental setup for DHI, described in this section, is an adjusted form of a single-beam dual-view setup, proposed for monitoring strain measurements in biological samples [132]. The schematic of the setup is provided in Figure 4.1 a).

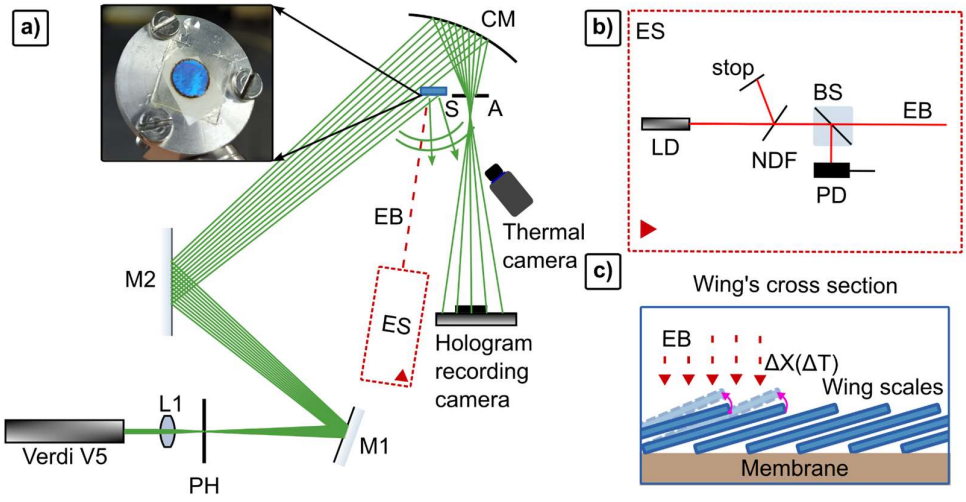

Figure 4.1 a) Experimental setup for DHI, incorporating a place for the excitation part of the setup (ES) and a thermal camera; b) Excitation section used for wing calibration; c) An illustration of illumination induced displacement ΔX of wing scales, due to a temperature increase ΔT. L1 – Lens; M1, M2 – Plane Mirrors; CM – Concave Mirror; EB – Excitation Beam; PH – Pinhole; S – Sample; A – Aperture; LD – Laser Diode; PD – Photodiode; NDF – Neutral Density Filter; BS – Beam Splitter.

The setup is simple, and easily adjustable, utilizing wavefront division for generation of the object and the reference wave. The laser beam from the Coherent Verdi V5 DPSS laser with a

wavelength of $532\ nm$ is spatially filtered using a system of a focusing lens (L1) and a pin hole (PH). The filtered beam is redirected towards the sample (S) using a system of plane mirrors (M1, M2), leaving the space in the setup for both the thermal camera, as well as the excitation section of the setup (ES). The average irradiance of the beam incident on the sample was set to $35\ \mu W/mm^2$ keeping the influence of the holographic recording on the sample minimal, and homogenous. The part of the wavefront not reflected by the sample is collected by a concave mirror (CM) and redirected towards the CMOS camera. There, it interferes with the object beam, creating a digitally recorded hologram. To avoid unnecessary light in the recording, CM is covered with a nontransparent screen with an aperture (A), large enough to let only the direct light at the CM's focus pass towards the CMOS imager.

The CMOS camera, used in the experiment, is a Nikon 1V3 digital camera with a resolution of 5232×3488, and the acquisition frame rate of $60\ fps$. It has a buffer of 40 images, resulting in recording length of approximately $667\ ms$. The $2.51\ \mu m$ value of this detector's pixel pitch is used in the hologram reconstruction procedures. Thermal imaging was done using the FLIR A65 thermal camera, with a 640×512 resolution, and a $30\ fps$ acquisition frame rate with temperature linear mode turned off. Even though this thermal imager performs a non-uniformity calibration periodically, additional flat field correction was performed before every acquisition to compensate for the influence of lens vignetting and different pixel to pixel sensitivities.

The ES of the setup used in wing calibration and temporal response measurements consisted of a microcontroller-controlled laser diode (LD), with a neutral density filter (NDF) manipulating the power of the excitation beam (EB) illuminating the sample (Figure 4.1 b)). To monitor the power, a beam splitter (BS) was used to redirect a part of the beam towards the monitoring photodiode (PD). LDs with wavelengths of $405, 450, 660$ and $980\ nm$ were used for calibration of a sample shown in Figure 3.4 d), covering the visible as well as a small part of the NIR part of the spectrum.

An illustration of the EB induced temperature change ΔT, and the consequent displacement of the wing scales ΔX is shown in Figure 4.1 c). The proper correlation of the measured DHI phase change $\Delta\varphi$ with the light induced displacement requires the use of Equation (20), while knowing the setup specific angle $\theta = 40°$. The resulting expression is given by:

$$\Delta X = 0.283\frac{\Delta\varphi\lambda}{\pi}. \tag{24}$$

Taking signs into consideration, we can conclude that the positive/negative phase changes correspond to displacements of the specimen away/towards the CMOS camera respectively. The conditions forcing the movement of the specimen one way, or the other, will be discussed at a later stage of this thesis. A photograph of the discussed experimental setup is shown in Figure 4.2.

Further experiments using the same basic holographic configuration were conducted, utilizing a sample suspended in air, excited using LDs with 1310 and $1450\ nm$ wavelengths (L1310G1 and L1450G1, Thorlabs). The results of these experiments were recorded using a compact $532\ nm$ DPSS laser module (CPS532, Thorlabs) and a Basler acA2440-75um CMOS camera. Its sensor has a 2448×2048 resolution, at a maximum of 75 fps, with no inherent buffer limitation, thus enabling acquisitions of several seconds. EB LDs used in these experiments required high operating currents, necessitating a development of a dedicated programmable current driver described in Section 4.2.

The synchronization of different parts of the setup was conducted through software control of the instruments using dedicated applications (VIs) developed in LabVIEW. The synchronization software is described in detail in Section 4.3.

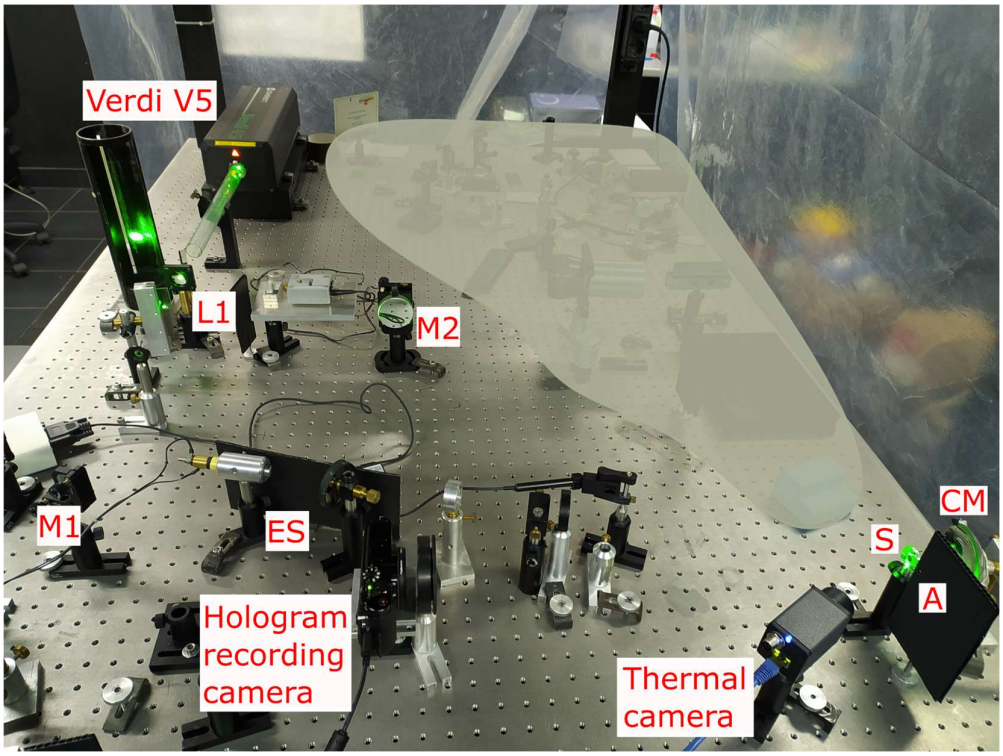

Figure 4.2 A photograph of a setup illustrated in Figure 4.1.

While testing the temporal response of the proposed image sensor, a need arose for a setup enabling a stable temperature control of the wing sample. A temperature control mount was designed to achieve this purpose. Due to its dimensions, the previous holographic setup was abandoned in temperature control experiments, and the second holographic setup devised.

The illustration of the utilized temperature-controlled mount is presented in Figure 4.3.

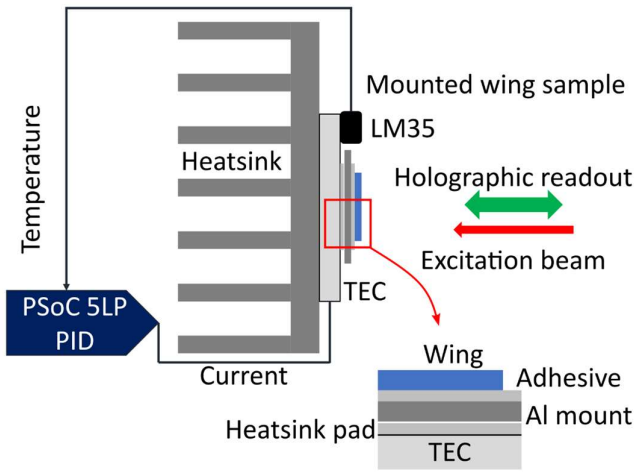

Figure 4.3 A mount for temperature control of the wing sample. PSoC – Programmable System on a Chip microcontroller; TEC – thermoelectric temperature controller; PID – Proportional Integral Differential control; LM35 – analog temperature sensor.

The sample is adhered to the aluminum sample holder using one of the adhering materials, discussed in the previous Chapter. The aluminum sample holder is then adhered to the thermoelectric

temperature controller (TEC) – Peltier element, using a double adhesive heatsink pad. The excess heat from the hot side of the TEC is conducted through a large heatsink (attached to the TEC using thermal paste) to the surrounding air. The heating/cooling operation of the mount is controlled using current flow through the TEC. A detailed operation of the electronics, used for temperature control of the proposed mount is provided in Section 4.2.

The aforementioned second holographic setup, used for measurements with the temperature-controlled mount is shown in Figure 4.4. The setup provides the required space behind the sample holder for the temperature control mount and the heatsink. It incorporates a Mach-Zehnder-like architecture, differing from the standard solutions in the beam combining section. The NDF is used as the first BS to divide the collimated incident laser light into two paths, the object path (light transmitted through the NDF), and the reference path (light reflected on the NDF). The reference part of the wave is redirected towards the CMOS camera using two plane mirrors and expended using a short focal length lens. The object part of the wave is expanded using a two-lens beam expander, made up of a short focal length input negative lens, and a large focal length, large aperture output positive lens. The expanded beam is transmitted through the second BS towards the object (wing sample, mounted on a temperature-controlled mount), where it is reflected (scattered) back to the second BS and redirected to the camera. The rotation of the second BS enabled another degree of freedom regarding the adjustment of the angle between the object and reference waves, while eliminating the influence of parasitic internal BS reflections on the reconstruction. The representative recordings and reconstructions made by the setup shown in Figure 4.4 were previously presented in Figure 2.1 b), Figure 2.3, and Figure 3.3 c) (the MO is placed between the sample and the second BS).

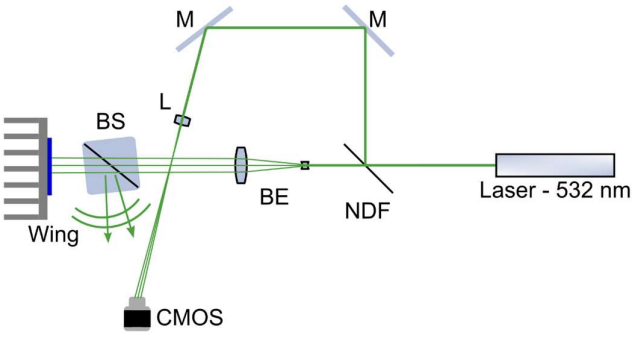

Figure 4.4 A Mach-Zehnder – like holographic setup for examination of the temperature-controlled wing sample. NDF – Neutral Density Filter; BS – Beam Splitter; BE – Beam Expander; M – Mirror; L – Lens.

The obvious drawback of the presented holographic approach is the loss of power of the object beam – resulting from the two passes through the second BS. The apparent solution utilizing a quarter-wave plate and two polarizing BSs was avoided on account of the compactness, complexity, and cost of the final setup. The problem of low holographic fringes visibility was solved by implementing the first BS as a NDF, serving as a variable reflectance BS, and adjusting the power ratio between the object and the reference waves.

The length of the object and the reference branches of the holographic setup was adjusted to satisfy the constraints, imposed by the coherence length of the utilized laser, measured to be on the order of 10 cm. Special consideration was necessary when aligning the holographic setup in order to minimize the angle between the object and the reference waves. Thus, the focus of the lens (considered as a point source), expanding the reference wave, was positioned very close to the second BS. Apart from the benefit of the small angle between the waves, this ensured that no part of the reference wavefront was obscured (reflected) by the BS.

Another considerable advantage of the described setup is its potential for a relatively small footprint, as the dimensions of the setup are above all limited by the size of the utilized components. The only other limiting factor is the required distance from the camera to the recorded sample allowing the use of the approximated formulas for the diffraction integral. The total length of the setup was under $50\ cm$ in the experiments. The footprint of the setup could be further reduced, if needed, for implementation in a stand-alone device configuration.

The previously mentioned compact $532\ nm$ DPSS laser module (CPS532, Thorlabs) was used for holographic interrogation. The excitation used in the experiments investigating the influence of heating/cooling of the wing's response originated from a He-Ne laser with a $5\ mW$ output Gaussian beam (Thorlabs, HNL050L). The utilized CMOS camera was Basler acA2440-75um. The software for acquisition and measurement in these experiments is further described in Section 4.3. Due to the higher coherence length laser, and the higher resolution camera, the setup from Figure 4.1 a) resulted in higher quality holograms compared to the setup from Figure 4.4. This is why its use was preferred, except in Section 6.4, where it was restricted by the dimensions of the sample mount.

4.2 Custom-designed electronic devices

The 1310 and $1450\ nm$ NIR LDs (L1310G1 and L1450G1) were utilized as the excitation in experiments testing the NIR response of the wing due to their very high output powers, ensuring the wing is illuminated with enough energy to induce the holographic response. Both LDs are rated with $2-2.5\ W$ continuous wave optical output power, when pumped with a direct current (DC) of $5\ A$, and have threshold currents (needed to achieve lasing) at about $0.5\ A$. The commercially available laser drivers which enable safe operation at such high currents are usually expensive and bulky. The solutions found in literature are often complicated, and offer very high-performance parameters, not required in our applications [133–135]. This led to the development of a dedicated laser driver solution. At $1\ A$ of drive current, the chosen LDs are expected to dissipate more than $1.1\ W$ of power, resulting in heating, performance decrease and possible permanent damage to the LDs. This is why the custom-designed driver incorporates a temperature control system apart from the current source needed to drive the LD. The basic considerations in driver design will be commented upon in the following text, while the details of the realization are presented in paper **V** [95].

The schematic of the custom-designed LD current driver is presented in Figure 4.5 a).

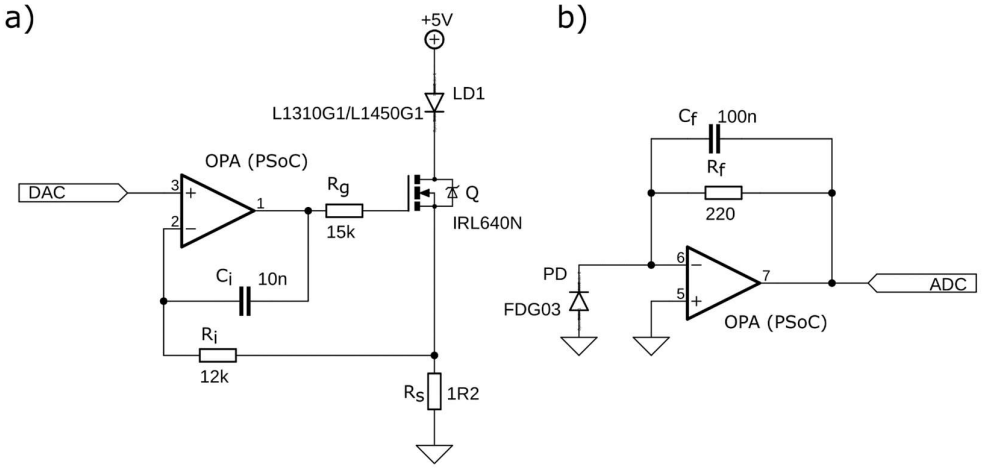

Figure 4.5 a) LD current driver. b) PD with TIA for optical power monitoring.

To achieve a small footprint, programmability and reconfigurability of the proposed driver, most of the active driver components, such as operational amplifiers (OPA), digital-to-analog (DAC)

and analog-to-digital converters (ADC) are used as integrated functional blocks, readily available within the utilized microcontroller board (Infineon FreeSoC2 – programmable system-on-chip PSoC5LP). Ensuring a linear OPA operation regime, while assuming no significant DC currents through resistor R_i, the voltage of resistor R_s is driven to the value of the DAC voltage V_{dac}, set by the microcontroller. Thus, this voltage sets the current:

$$I = \frac{V_{dac}}{R_s} \tag{25}$$

through the branch comprised of a MOSFET Q, and the LD. The IRL640N logic level MOSFET is the only active component outside of the PSoC, apart from the LD itself. It is used to increase the current output of the designed driver to be in the $0 - 1\ A$ range. The output of the OPA controls the gate of the MOSFET, thus controlling its channel, providing enough current to keep the OPA in the linear regime. The resistor R_g is added between the OPA output and the gate to prevent OPA oscillations due to capacitive loading, while the integrator R_i - C_i feedback is added to ensure controller stability. The driver exhibits a full-scale error of 0.11 %, 0.084 % long-term stability and a modulation bandwidth of $2\ kHz$. Furthermore, a soft-start feature was implemented within the microcontroller software to ensure the LD's safe operation during the turn-on procedure [136].

To monitor a part of the LD output power, a PD (FDG03, Thorlabs) is connected in a trans-impedance amplifier (TIA) configuration shown in Figure 4.5 b). With PD's responsivity of 0.7 and $0.8\ A/W$ at 1310 and $1450\ nm$ wavelengths, the respective sensitivities of the TIA voltage output are calculated to be 154 and $176\ mV$ per $1\ mW$ of optical power. The TIA is overcompensated to a bandwidth of $\sim 7\ kHz$, a value still well above the bandwidth of the current driver.

The temperature controller of the proposed LD driver relies on a current driven TEC, onto which the lasers are mounted. The TEC current driver shares the same design as the LD driver discussed in the above text. The two drivers only differ in the choice of the resistor R_s. The R_s for the LD driver has twice the resistance of the TEC driver's R_s due to the decreased precision and increased output current requirements of the TEC driver. The TEC driver's output current is software limited to a $0 - 2\ A$ range. The LD temperature is monitored using a KTY82-210 temperature sensor, driven by a PSoC integrated $1.4\ mA$ current DAC, and readout using PSoC's Δ/Σ type ADC with $1\ mV$ resolution. A version of a proportional integral differential (PID) control algorithm for temperature regulation was implemented digitally on a microcontroller [137], ensuring fast controller response and no measurable steady state error between the set and measured temperatures.

The user communication and parameter setup of the driver are conducted through serial communication, enabling the driver to be controlled thorough software applications running on a personal computer (PC).

The hardware-software implementation of the driver for the temperature-controlled mount is similar to the LD driver's TEC controller. Yet, the PSoC microcontroller in this device was used only for control (using the aforementioned PID algorithm), processing, and data acquisition tasks. The current driver circuit was realized as a separate device using a configuration known as a Howland current pump [138,139], based on readily available, general-purpose components. The current pump is shown in Figure 4.6.

The working principle of the Howland current pump is based on a differential amplifier, comprised of the OPA (LM358 – IC1A) with two input and two feedback resistors, R_i and R_f, respectively. The circuit amplifies the voltage difference between the two inputs (DAC and ground in this case) with a predefined gain R_f/R_i. In the Howland pump configuration, the output and reference potentials of the differential amplifier are connected across a shunt resistor R_s, defining its current, thus setting the current through the load (in this case, the TEC). The MOSFET IRF540N is used as a current booster, while the capacitor C_f prevents circuit oscillations. Finally, the unity gain

buffer (LM358 – IC1B) is added to decouple the influence of the branch with the load on the accuracy of the feedback. The current through the TEC is governed by equation:

$$I_{TEC} = \frac{V_{dac} \cdot \frac{R_f}{R_i}}{R_s}, \quad (26)$$

where in our case the R_f/R_i ratio equals 0.1 in order to adjust the $0 - 4096\,mV$ range of the V_{dac} output voltage to the driver's output current range of $0 - 4\,A$. The utilization of the LM358 general purpose OPA in this current driver results in non-negligible DC errors of the set current due to its high input offset voltage (~mV). However, the choice of this OPA is justified by its low cost, stability, and ease of use, noting that the induced DC errors of the current source play no role in temperature regulation using a PID algorithm. The circuit is powered using a single voltage supply, resulting in unipolar operation of the current source. Thus, to achieve both heating and cooling using the temperature-controlled mount, the TEC polarity and the direction of the PID were changed between measurements.

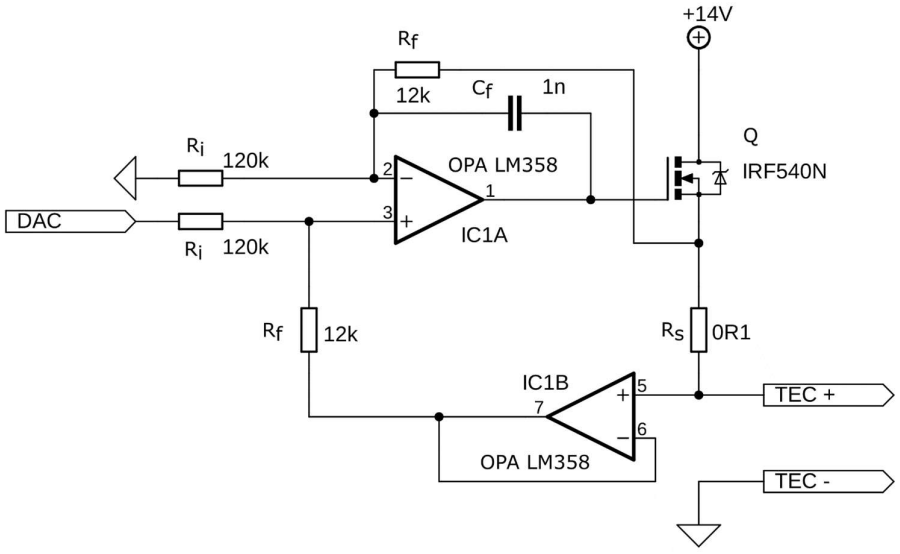

Figure 4.6 Unipolar Howland current pump for Peltier element drive.

The measurement of the mount's temperature was accomplished using an analog temperature sensor LM35 with $10\,mV/℃$ sensitivity. The PSoC's 12-bit ADC with a range of $0 - 2048\,mV$ was used to monitor the temperature sensor output, resulting in mount's temperature control accuracy of 0.05 ℃. The temperature control range of the mount was determined to be between 5 and 65 ℃.

4.3 Software

The simplified flow chart of the main LabVIEW VI for synchronization, acquisition, and control is presented in Figure 4.7. The program is designed to ask the user during startup which of the system components will be utilized. The available options are Nikon 1V3, FLIR A65, and a microcontroller (Arduino MEGA 2560 or PSoC5LP, depending on experiments). Communication with a microcontroller turning on the EB LD is realized through VISA serial communication functions, while the Nikon 1V3 is controlled through a C# SDK wrapper [140]. It is used in LabVIEW through .NET constructor, property and invoke nodes. FLIR A65 is accessed through commonly used NI-IMAQdx drivers. The VI is comprised of two parallel while loops, with one way communication

from the main loop to the loop used for FLIR A65 acquisition. The main loop is designed as a simple event driven state machine, enabling easy and prompt user interaction with the hardware. It enables multiple functionalities (not shown on the flow chart to avoid cluttering) such as the Nikon setup and battery check, EB turn-on for experiment alignment, parameter change for the FLIR A65, and most importantly the start of synchronous acquisition.

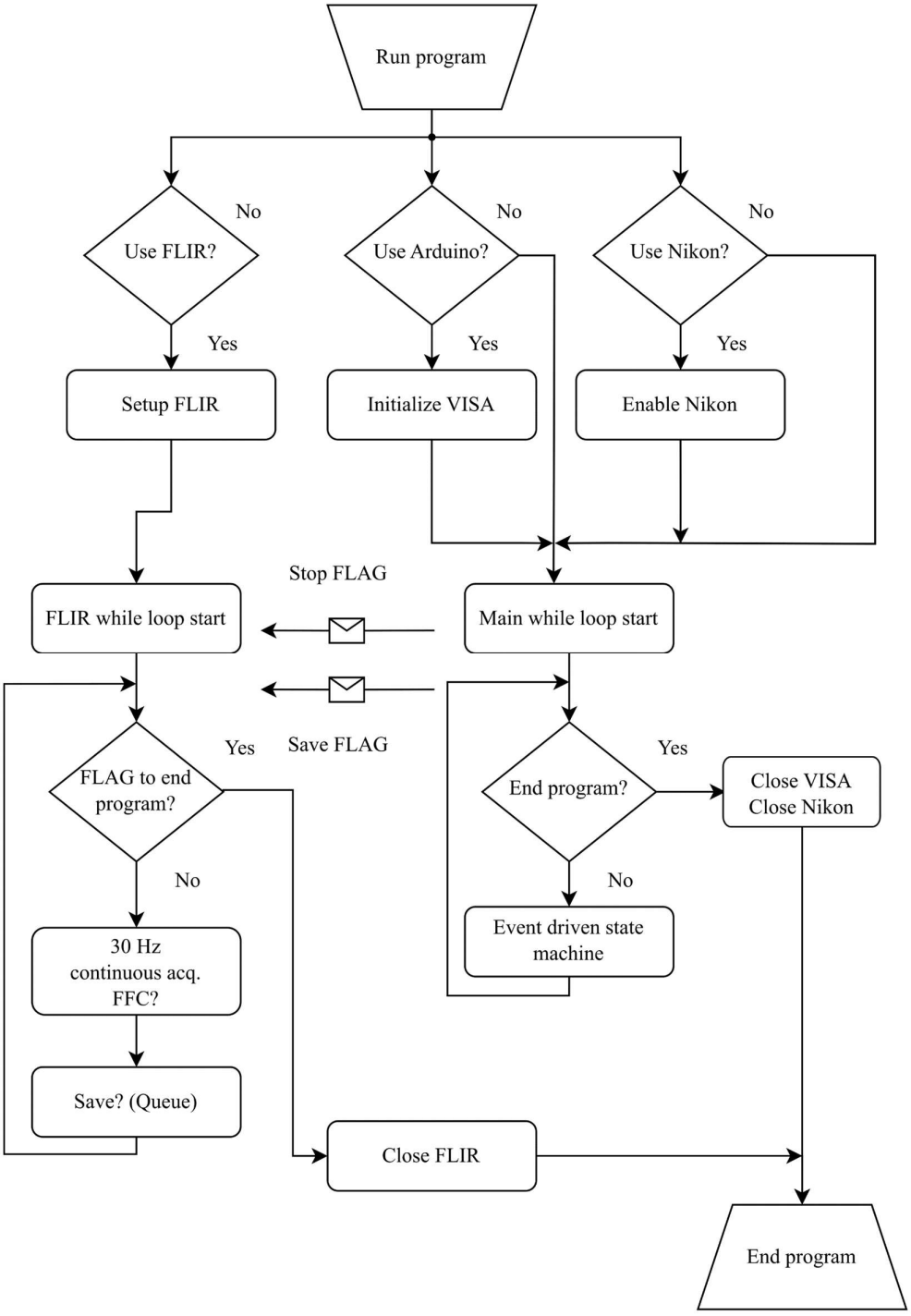

Figure 4.7 A simplified flow chart of the LabVIEW VI, designed for acquisition and control. FFC – Flat field correction.

When the synchronous acquisition is started, the LabVIEW sends the signal to the microcontroller in the form of a string containing the number of required laser pulses, their delay and duration in milliseconds. The saving of the FLIR A65 is turned on by sending the save flag to the second while loop. Finally, Nikon is requested to start filling the buffer with 40 high-resolution images. The signal flow is forced through the connection of error signals between components on the block diagram. The hardware synchronization was deemed unnecessary at this research stage, as no significant delays were encountered. The thermal images are saved outside of the FLIR A65 loop, in an additional while loop (called upon only when required) to preserve the 30 fps operation of the thermal imager. The loop for saving thermal images reads the images from a queue, whereas the images are enqueued in the FLIR A65 loop. Prior to saving, the user has the option to perform a thermal image acquisition of an object having a flat surface with uniform temperature and emissivity. With this image, flat field correction can be done using an integrated LabVIEW VI, thus correcting the vignetting effect of the camera's lens.

Additionally, the main loop provides hologram reconstruction and thermal image analysis features, used for quick recorded result examination. For the hologram reconstruction, the parameters of the utilized setup are required as input by the user. The reconstruction is performed in LabVIEW by calling a MATLAB script with a numerically implemented Shifted-Fresnel algorithm. For thermal image analysis, the data is imported from the folder where it was recorded and a dedicated SubVI is called. The front panel of the SubVI is presented in Figure 4.8. The panel shows an acquired thermal image of a wing sample, illuminated by an X shaped, 660 nm EB. The developed software enables measurements of temperature change across a defined profile, or through time in a selected region of interest. The software provides multiple colormap and intensity scaling options.

After the user presses the Stop button, the main loop stops and sends a flag to the FLIR A65 loop to stop. Before the end, all of the open communication channels are closed.

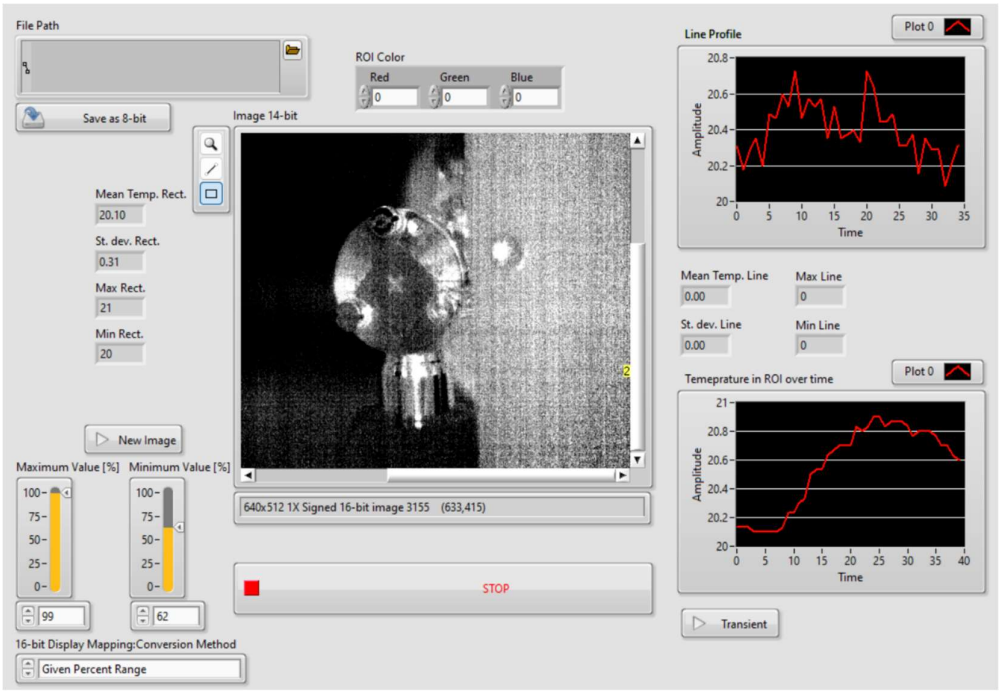

Figure 4.8 A screenshot of a VI for thermal image analysis. The VI shows an acquired thermal image of a wing sample, illuminated by an X shaped, 660 nm EB.

Due to the very different properties of PC communication with Nikon 1V3 and Basler acA2440-75um CMOS cameras, the latter required its own VI application. The application utilized

the same basic principles as its previously discussed counterpart, differing in utilization of NI-IMAQdx drivers for control and acquisition. The program was structured according to the Producer/Consumer design pattern. The main loop (producer) is once again designed as an event driven state machine in which the acquisition with a user definable frame rate is achieved and the acquired images are enqueued. The second loop (consumer) dequeued the images and was used for time consuming hologram saving. This VI application did not incorporate the FLIR A65 camera, as no experiments during the work of this thesis required simultaneous use of both Basler acA2440-75um and FLIR A65.

Chapter 5. Calibration and spectral properties

After holographic interrogation of a sample, and processing of the obtained data (as per DHI instructions of Chapter 2), the resulting two-dimensional displacement map of a sample is calculated. Using this displacement map as a readout of the proposed imaging sensor requires determining its relationship to the power/irradiance of the light illuminating the sample. The process of finding this dependence is what will be further referenced as wing calibration. It will be repeated for multiple wavelengths of incident light, finally enabling the correlation between the displacement's spectral sensitivity and the wing's absorption curve. Apart from this, the chapter will further discuss the reproducibility of the radiation induced response, as well as the difference in response of a sample suspended in air, compared to the sample from Figure 3.4 d).

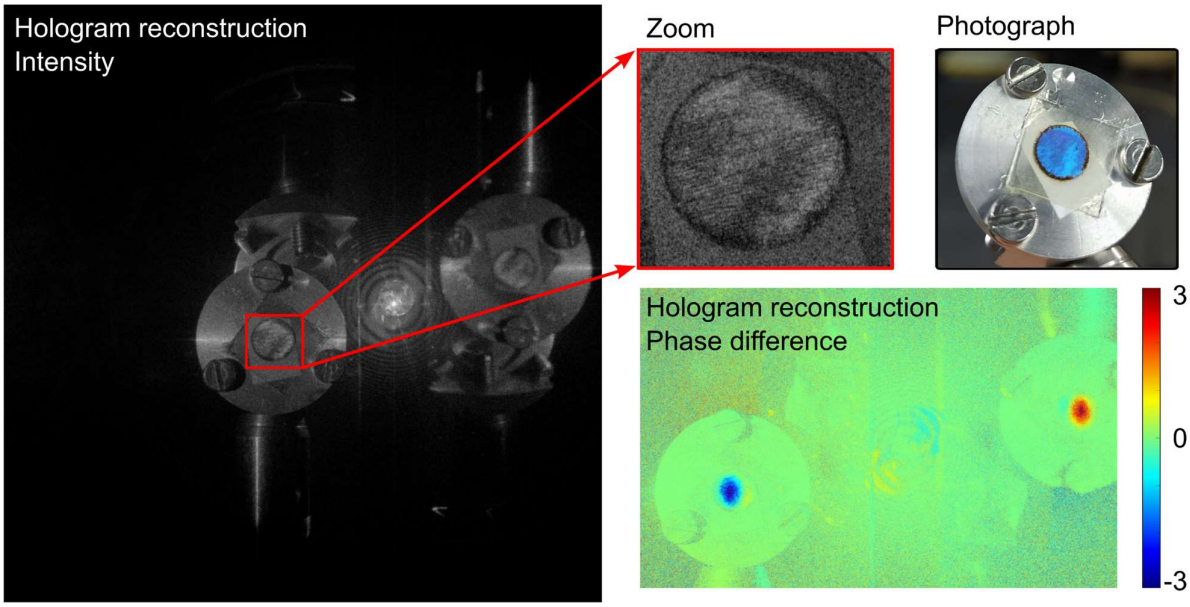

Figure 5.1 An example of a hologram reconstruction (intensity and light induced phase difference), showing a mounted wing sample, with a photograph of a mounted sample for comparison.

5.1 Light induced displacements

Using the setup described in Chapter 4 resulted in a hologram reconstruction shown in Figure 5.1. Both the intensity and phase difference images show the focused object image (left) and its out of focus, conjugated twin (right). A zoomed part of the intensity image shows discernable rows of scales, under 200 μm apart. Comparing the provided photograph of a mounted sample with the reconstruction illustrates the level of detail achievable with the utilized technique. The phase map shows a sample's light induced response, as a light to dark blue, pseudo-colored region over a large

part of the sample area. Based on Equation (24), the visible phase change going down to $-\pi\, rad$ corresponds to a displacement of up to $151\ nm$ of the illuminated scales.

The reproducibility of the light induced displacement as an opto-mechanical response of an actual biological structure was a natural concern. To address this issue, the $8\, mW$ EB with a wavelength of $405\ nm$ was used to illuminate one of the samples three times separately, ensuring the same experiment conditions. The time between measurements was 5 minutes. Figure 5.2 shows the obtained response. A complex phase wrapped pattern is visible in all three phase difference images. Although not identical, the complex patterns show remarkable similarity, leading to a conclusion that the response is reproducible. The difference in response between measurements $2-1$ and $3-1$ around the point indicated by an arrow in Figure 5.2 was -0.0013 and $-0.303\, rad$, respectively. Knowing the first measurement's unwrapped response value of $11.6597\ rad$ around the same point, relative errors of -0.01 and -2.60 % were calculated. The higher change in the $3-1$ case can be explained by the imperfect sample to mount adhesion, as the adhesive for this sample was an adhesive tape. Further tests of reproducibility, concerning the reproduction of the temporal response trend at different EB powers will be analyzed in Chapter 6.

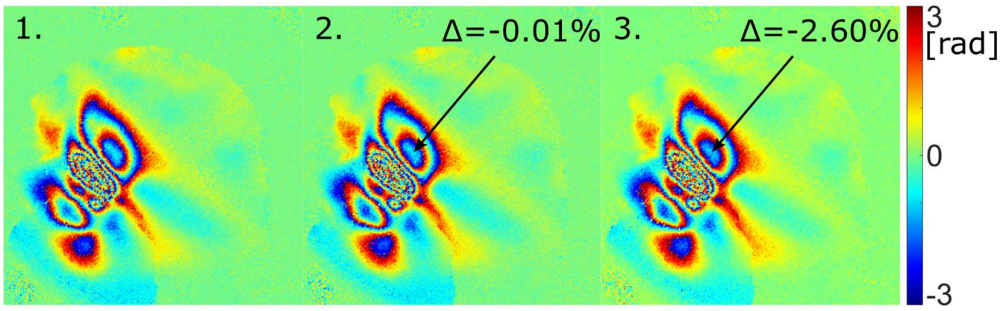

Figure 5.2 Testing the reproducibility of the light induced displacement. Three separate reconstructions after the repeated $8\, mW$, $405\ nm$ excitation.

During experiments, a phenomenon of counter-bending of the wing sample was observed around the light induced displacement, in the non-illuminated areas. It was more pronounced in samples with a freestanding wing, suspended in air, without a mount supporting the back side. The counter-bending was presumed to occur due to the movement and twisting of the wing membrane, and not just the scales. To test this hypothesis, the single-beam, dual-view setup was utilized to its full extent, allowing the simultaneous holographic monitoring of both the front (iridescent) and the back (non-iridescent) sides of the wing. During the experiment, the wing's front (iridescent) side was illuminated for $110\ ms$ using a $2\, mW$ EB with a wavelength of $660\ nm$. The results are shown in Figure 5.3 a). The phase wrapped maps of both sides are clearly visible, and remarkably similar, apart from the difference in direction of the displacement. While the central, illuminated part of the membrane in the frontal image moves to positive phases, the surrounding bending occurs in the other direction. However, the displacements of the back side are complementary to those of the front, leading to a conclusion that the whole membrane has a tendency to move, and not just the scales.

Further experiments concerning the movement of the non-iridescent side were conducted, examining its response to direct illumination, and comparing it to the response of the iridescent side. The sample was first positioned in the intended way, with the iridescent side exposed to the EB, facing the CMOS detector. The response of this setup to $980\ nm$, $2\, mW$ EB with $110\ ms$ duration was recorded. The sample was then flipped in order to expose the non-iridescent side to the same EB and record its holographic response. The resulting phase maps are shown in Figure 5.3 b). Once again, the response is complementary. The iridescent side moved to produce positive phase changes going over $10\, rad$, and the non-iridescent side moved the other way, producing the phase changes going under $-10\, rad$. This is expected, assuming similar absorption properties of the sample at this

wavelength irrespective of the side facing the EB, knowing that the whole membrane moves. Thus, no benefits are obtained by examining the non-iridescent side of the wing, while the quality of the holographic recording decreases as less green light is reflected from the non-iridescent scales. Cleaning the membrane completely out of scales from both sides was attempted, in order to discern the contribution of the membrane vs. scales displacements to the overall response. However, the membrane alone was mostly transparent, leading to a negligible holographically observable response.

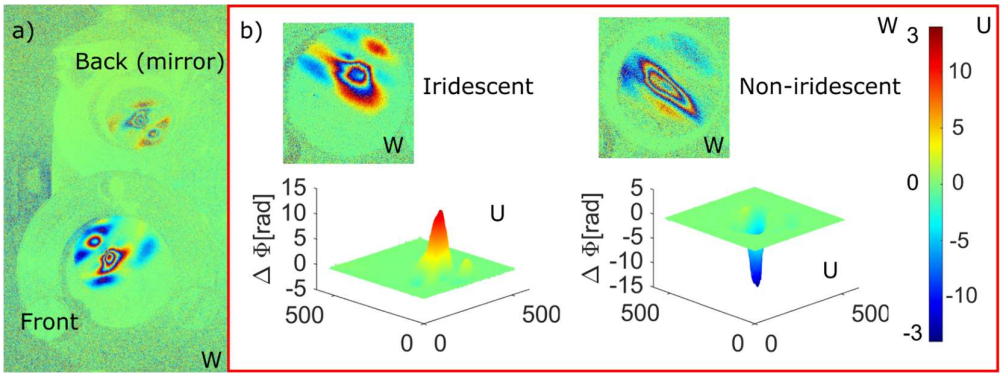

Figure 5.3 Iridescent vs. non-iridescent light induced response: a) simultaneous recording of both sides of the wing; b) responses of both sides of the wing, when exposed to the same EB. W – wrapped phase maps; U – unwrapped phase maps.

Contrary to the previously discussed examples, the sample from Figure 3.4 d) showed far less (although still present) counter-bending of the membrane (phase image shown in Figure 5.1), because its back side was attached to the holder using wax. The reduced influence of counter-bending makes these types of samples better candidates for imaging applications, as the light induced response is better confined within the illuminated area. However, due to the reduced membrane movement, the overall response to the same EB was less pronounced. On the other hand, the samples exhibiting the counter-bending still have light detection capacity, functioning as power meters with a broad spectral range. Differences in temporal response of the freestanding and the mounted samples will be discussed in Chapter 6.

The unwanted bending and wrapping of the membrane are not the only observed side effects of wing's opto-thermo-mechanical response. Samples with no strong support of the wing's back side, such as a freestanding sample suspended in air, are shown to be prone to light induced vibrations, due to abrupt, high-power excitations. The vibrational response of the sample manifests in both intensity and phase images of holographic recordings. While the phase information becomes unreadable due to the high frequency changes of sample's position, the intensity images show characteristic fringe patterns, illustrating the excited modes of membrane oscillation. An example of the influence of light induced vibrations on the intensity and phase difference images is presented in Figure 5.4.

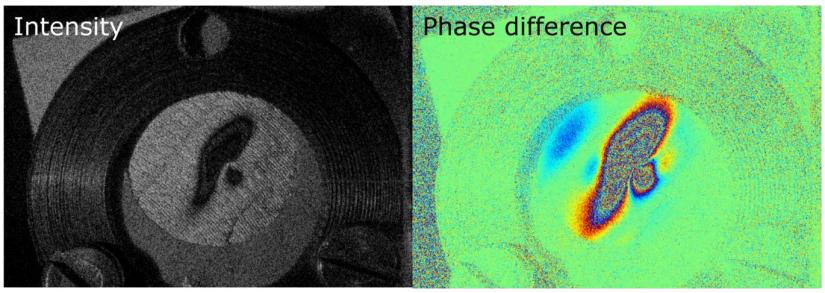

Figure 5.4 Influence of light excited wing vibrations on the holographic recording. The 19 mW, 110 ms, 980 nm EB illumination was used. The Figure shows the sample, 17 ms after the exposure.

The vibrating pattern appears right at the start of the EB illumination, when it is at its most pronounced. During the continuing illumination, the vibrations start to fade away, only to be excited once again at the falling edge of the illumination intensity, although this time to a lesser extent. The illustration of the time evolution of the light induced sample vibrations, due to a $19\,mW$, $110\,ms$, $980\,nm$ EB pulse is provided in Appendix B. The appearance of vibrations was limited to samples with a freestanding membrane, while samples such the one shown in Figure 3.4 d) exhibited a vibration free response.

Another approach in detector design involved artificial pixelization of the proposed detector, creating samples shown in Figure 3.4 c). The main goal was to reduce the influence of membrane interaction between the illuminated and non-illuminated areas of the wing. The pixels were cut in sizes of 0.5×0.5, 1×1 and $2 \times 2\,mm$, allowing for investigation of differences in reaction due to the changing number of scales, confined within a single pixel square. The resulting intensity image of a reconstructed hologram, fused with the phase difference image due to the $110\,ms$, $3\,mW$, $660\,nm$ EB is presented in Figure 5.5. The Figure also shows a 3D view of the induced phase change. Unfortunately, unwanted counter-bending of the pixel edge is visible from the overlayed phase map, deeming this approach unsatisfactory. Moreover, some of the smaller pixels expressed highly reduced responsivity, leading to the conclusion that the laser cutting of the sample during manufacture caused severe burning of the sample.

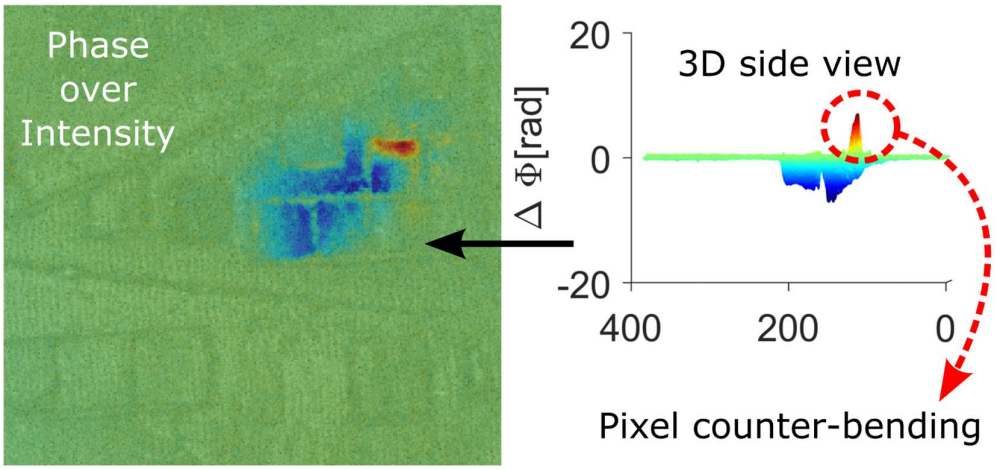

Figure 5.5 A fused image of intensity and light induced phase difference map of an artificially pixelized (laser-cut) sample (left). A 3D map of the phase response (right).

Unlike CMOS or CCD sensors, limited by bit depth (quantization), the readout of the proposed bioderived sensor is limited by the DHI's phase noise. To quantify the noise contribution, a standard deviation of phase noise of a typical non-irradiated sample was measured to be $0.046\,rad$. This corresponds to displacements of $2.2\,nm$, stability hard to maintain long-term outside of vacuum conditions. With the utilization of the phase unwrapping algorithms, the highest observable light induced phase changes ranged from 15 to $45\,rad$, depending on the sample. From these measurements, the dynamic range of the sensor was calculated to be in the range of 50 to $60\,dB$.

5.2 Wing's calibration and spectral sensitivity

The sample from Figure 3.4 d) was chosen as the optimum solution for further experiments regarding calibration of light detection capacity and image formation. To calibrate the sample, pulsed EBs with $405, 450, 660$ and $980\,nm$ wavelengths were utilized. The sample was exposed to EB pulses with varying power levels and $200\,ms$ durations, and the resulting phase map at the end of exposure was regarded as the measured quantity. The relationship between the total EB power P_{tot}

and the light induced displacement $\Delta\varphi_i$ at any point (denoted by an index i) was believed to be linear, an assumption confirmed by the experimental results of Figure 5.6 a) and b).

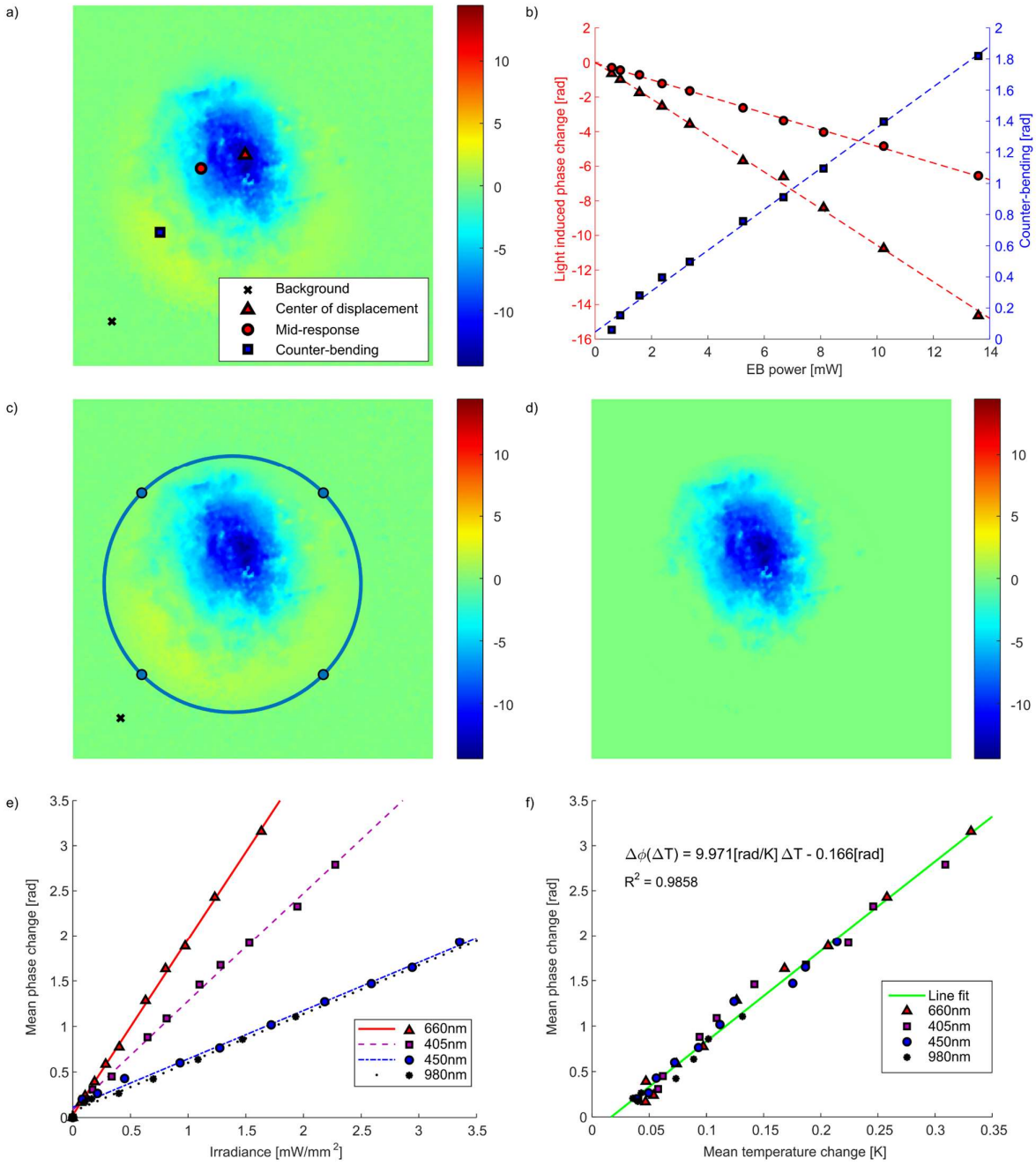

Figure 5.6 a) Phase difference map of the illuminated sample after the 200 ms EB exposure; b) The dependence of phase change on EB power for different sample points, shown in a). Direct light induced displacement – negative phases; counter-bending – positive phases; c) Depiction of the manual process of region of interest and background selection; d) Light induced phase change, without the counter-bending; e) The dependence of φ_{avg} on EB irradiance for different EB wavelengths; f) The dependence of φ_{avg} on the induced temperature change of the sample T_{avg}.

Similar linear trend was observed for light induced temperature changes, measured using a thermal camera. From the obtained results, we deduced that the response is non-uniform, due to

different beam shapes and irradiance distributions of the utilized EB LDs. Counter-bending of non-illuminated areas is also evident along the sample edges, yielding positive phase changes instead of negative (corresponding to the direct response). Thus, we conclude that analyzing any given single point of the sample cannot provide useful information, needed to compare the wing's response sensitivity at different wavelengths. Furthermore, utilization of the scaling parameter of the Shifted-Fresnel holographic reconstruction method will greatly influence the readout, as the pixel distance is scaled, thus scaling the region of the measured $\Delta\varphi_i$. The same goes for utilization of alternative reconstruction methods such as a single Fourier transform reconstruction, where the pixel distance highly depends on the hologram recording distance. Such results would of course be valid only for one recording geometry, even under the assumption of uniform, constant beam irradiance for all the utilized EBs.

Addressing the issue of generality and comparability of the obtained results requires a new readout metric to be devised. This metric must take into account that the reaction of different parts of the wing relates to the spatial power density of the illumination at that particular region – EB's irradiance distribution. To devise such a metric, we assume that the wing's response is homogenous, localized, and that a single point readout $\Delta\varphi_i$ is proportional to the absorbed EB power at that particular point, regardless of the pixel distance. Thus, a summation of the response over all of the N excited pixels should be proportional to the total EB power:

$$\sum_{i=1}^{N} \Delta\varphi_i \sim P_{tot}. \tag{27}$$

Measuring the EB covered area S_{EB} using a CMOS detector without a lens, we can calculate the average irradiance of the EB (denoted by I_{avg}), and relate it to the average response:

$$\varphi_{avg} = \frac{1}{N}\sum_{i=1}^{N} \Delta\varphi_i = K_\lambda \cdot \frac{P_{tot}}{S_{EB}} = K_\lambda \cdot I_{avg} \tag{28}$$

creating a metric which should be immune to the previously outlined issues. A proportionality constant K_λ takes the role of measurement sensitivity, having the units of $[rad/(mW \cdot m^{-2})]$. The constant's index λ symbolizes its wavelength dependence.

To compensate for the counter-bending of the non-illuminated sample regions, a condition is introduced into the previous equation. The value of a point $\Delta\varphi_i$ will be introduced into the summation only if its phase changes in the correct direction and it is larger than the background (eliminating the positive counter-bending). The point should also belong to the region of interest of holographic recording (i.e. the sample area). The representative process of selecting the region of interest for $\Delta\varphi_i$ summation, as well as the background region used for threshold determination is shown in Figure 5.6 c). The resulting phase change map, with the counter-bending eliminated is presented in Figure 5.6 d).

Table 1 Comparison of the average phase change calculations for different pixel scaling of the Shifted-Fresnel reconstruction.

Shifted-Fresnel method	**Pixel size $[\mu m]$**	φ_{avg} $[rad]$
$s = 5$	12.55	-3.6652
$s = 10$	25.1	-3.6779
$s = 14$	35.14	-3.7391

To validate the benefits of the proposed metric, φ_{avg} was calculated for three different scaling parameters of the Shifted-Fresnel reconstruction algorithm. The obtained results are outlined in Table

1. The calculated values vary up to 2%, a deviation easily explainable by a manual background and region of interest selection processes.

Using a similar procedure, the temperature change map of the sample, acquired using a thermal camera, was used to calculate the sample's average light induced temperature change T_{avg}. This enabled us to relate the two relevant quantities φ_{avg} and T_{avg}. The experimental calibration data for different wavelengths, showing the dependence of φ_{avg} on I_{avg} is shown in Figure 5.6 e), while its dependence on T_{avg} is presented in Figure 5.6 f). The sign of φ_{avg} was changed from negative to positive, to make the graphs easily interpretable. The response of the average phase change to the EB irradiance is highly linear, which is to be expected after the point response analysis of Figure 5.6 b).

The sensitivity is highest in the red spectral region, followed by the region nearing the UV. Lower sensitivities are obtained in the blue and NIR spectral regions due to the increase in reflection/transmission of the wing, previously discussed in Chapter 3. However, the dependence of average phase change on the induced temperature change is shown to be wavelength independent. This is expected as the induced temperature change is a direct cause of the sample deformation and displacements. Thus, a single straight line is fitted through all the data. The sensitivity of the average phase change to the average temperature change is $9.971\ rad/K$, corresponding to a $0.478\ \mu m/K$ displacement.

The induced displacement due to heating is proportional to absorption of light in the particular spectral region. To confirm this hypothesis, the spectral dependence of sensitivity K_λ is plotted alongside the absorption curve of the specimen, obtained from the results shown in Figure 3.6. The plot is shown in Figure 5.7.

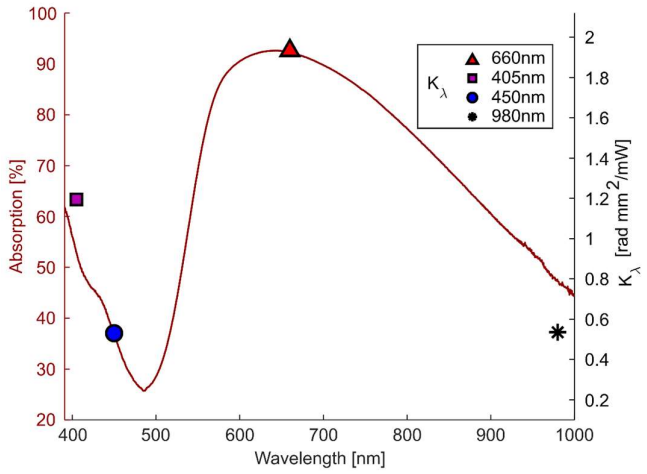

Figure 5.7 Spectral dependence of absorption (left, dark red), and sensitivity (right).

Based on the four K_λ points, we can conclude that the presented spectral dependencies follow the same trend. This indicates the applicability of the discussed sensing mechanism, as the response is above all governed by absorption of the sensing material. Based on the absorption, sensitivity in the spectral region of interest can be estimated. The specimen can be functionalized to increase absorption (e.g. using SWCNT [83], as discussed) and thus, sensitivity. This is favorable compared to quantum image detectors, as their sensitivity has a fundamental limit imposed by the semiconductor energy bandgap [7]. Furthermore, φ_{avg} can be related to the average photon flux Φ_{avg} by:

$$\varphi_{avg} = K_\lambda \cdot \Phi_{avg} \cdot \frac{hc}{\lambda}, \tag{29}$$

where h is the Planck's constant, and c is the speed of light in vacuum. The sensitivity S_λ of the proposed image sensor to the average incoming photon flux is inversely proportional to the wavelength:

$$S_\lambda = K_\lambda \cdot \frac{hc}{\lambda}. \quad (30)$$

Thus, the excess energy of the higher frequency photons is not wasted (as is the case for the quantum detectors) but used to heat the sensing material more efficiently. This, along with the increased absorption of melanin in the UV, explains the expected rise in sensitivity to the number of incident photons in the lower wavelength region.

To validate the possibility of radiation detection above the limits of silicon-based imagers, the wing's response was tested at wavelengths of 1310 and 1450 nm, as discussed in the Chapter 4. The investigated sample was freestanding in air on both membrane sides, to increase the sensitivity. The monitoring PD was not utilized during the experiments, as the EB powers in these experiments surpassed its absolute maximum ratings. Instead, the LD currents were set with high accuracy, enabling the use of the light-current (L-I) characteristics from the datasheet. The LDs were temperature controlled, keeping their case temperature at 26 ℃. Beam profiles of both LDs were highly nonuniform, with most of the power confined within the diverging TE polarization mode. Because of that, a focusing lens was used to redirect most of the available power onto the sample area. However, no means of EB area measurements were available, thus preventing the measurement of the average irradiance during experiments. The obtained phase map for 1450 nm, 1500 ms illumination is presented in Figure 5.8 a). The obtained results, relating the average phase change after 1500 ms exposure to the LD current for both LDs, are presented in Figure 5.8 b). The sign of φ_{avg} was changed from negative to positive, to make the graphs easily interpretable. The obtained lines match the L-I characteristics of the utilized LDs. From the fitted lines, L1310G1 and L1450G1 LDs' threshold currents are calculated to be 489 and 553 mA, respectively. Both diodes are rated with the same slope efficiency of $g = 0.45\ mW/mA$ [141]. Knowing the slopes of the fitted lines (Figure 5.8 b)), measurement sensitivities, normalized with the unknown EB area $\frac{K_\lambda}{S_{EB}}$ at 1310 and 1450 nm are calculated to be 154 and 134 $mrad/mW$, respectively.

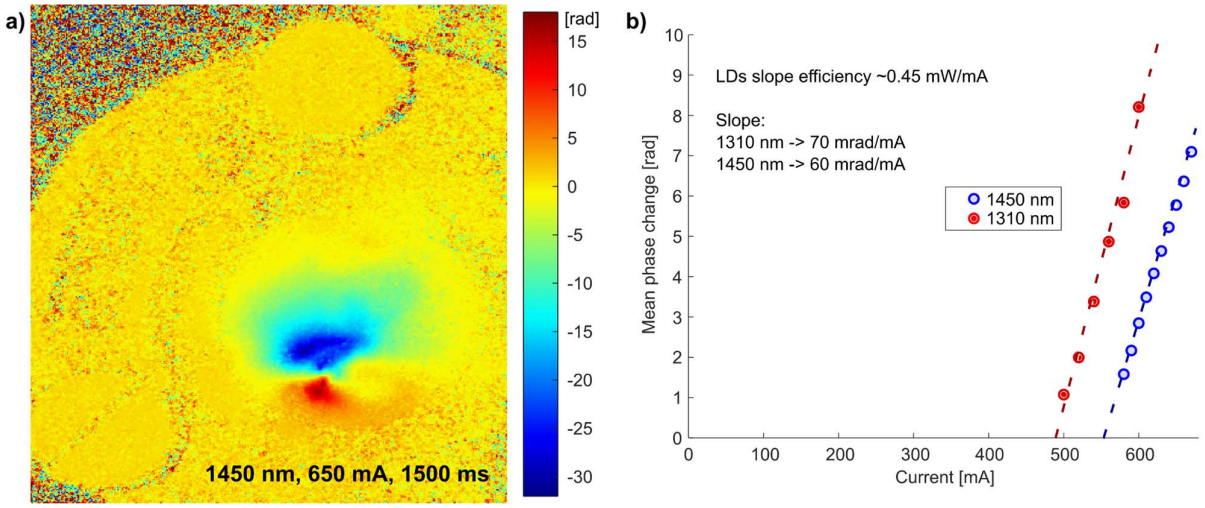

Figure 5.8 a) The phase response to 1450 nm, 1500 ms illumination; b) The dependence of φ_{avg} on LD currents for 1310 and 1450 nm EB wavelengths.

As the EB was highly nonuniform, it is interesting to note that the sensitivities in the regions of the highest displacement reached 517 and 882 $mrad/mW$, respectively. The calculated

sensitivities are not directly comparable to the K_λ values due to the previously discussed problems regarding the EB area and irradiance measurements. Even so, the results conclusively prove the IR detection capability of a non-modified *M. didius* wing, surpassing the silicon detectors' spectral range.

Chapter 6. Wing's temporal response

A sensor of any kind is characterized not only by its sensitivity related characteristics, but also by its response time, defining its measurement bandwidth. Based on the order of a differential equation governing the sensing process, we can differentiate between the zeroth, first, second, and higher order sensing systems. Different order systems are described best using different parameters. The first order system is described by its time constant, and the second order system with its natural frequency and damping ratio. Depending on the system order, its response may even exhibit some special features, such as resonance. The details of the physical phenomena occurring during sensing are often far more complicated compared to the ultimate treatment of the problem when analyzing the sensor's response. Even so, the approximations we assume yield sufficient results for everyday engineering practice.

This chapter will go over the analysis of the temporal response of the examined imaging sensor, explaining its behavior and limitations using the simplest satisfactory physical models of the sensing mechanism of interest. The results of Chapter 5 determined a strong causation between the average induced temperature change and the holographically measurable displacement of the wing scales. Therefore, the first analysis we will discuss is the analysis of the local illumination induced average temperature increase. A step response to the incident EB power will be analyzed, providing useful foundation in treatment of a large number of results obtained during the calibration process.

6.1 Time evolution of the wing's average temperature increase

Let us consider a part of a butterfly's wing described by its mass m and specific heat c_b, exposed to the air on one side, while connected to the aluminum mount on the other. Further considerations assume a thermal equilibrium at a temperature T_A before the radiative heating of the sample using a laser. Once the laser is turned on, the heat transfer equation, determining the incremental temperature increase dT of the sample during the dt time interval becomes:

$$mc_b\, dT = P_{tot}\, dt - \frac{T - T_A}{\theta_E}\, dt. \qquad (31)$$

Here, P_{tot} denotes the total EB power incident on the sample, while θ_E represents an equivalent thermal resistance, incorporating both the convective cooling of the sample towards the surrounding air and the conductive cooling of the sample through the adhesive material and towards the aluminum mount. The radiative cooling towards the ambient is assumed to be negligible compared to two other cooling mechanisms ♦. A reasonable approach is to also assume that the air and mount temperatures stay at a value of T_A despite the sample's temperature increase. With integration:

♦ Future research will further investigate the overall influence of radiative cooling on the response for different adhesive materials.

$$\int_{T_A}^{T} \frac{mc_b\, dT}{\left(P_{tot} - \frac{T - T_A}{\theta_E}\right)} = \int_0^t dt \tag{32}$$

a time evolution of the average wing temperature is obtained, and described by:

$$T = P_{tot}\theta_E \left[1 - exp\left(-\frac{t}{mc_b\theta_E}\right)\right] + T_A. \tag{33}$$

After the laser is turned off, we are left with the following form of the heat transfer equation:

$$mc_b\, dT = -\frac{T - T_A}{\theta_E} dt. \tag{34}$$

Integrating the previous equation using the starting temperature of the heated wing (T_{max}) as a lower limit:

$$\int_{T_{max}}^{T} \frac{dT}{T - T_A} = -\int_0^t \frac{dt}{mc_b\theta_E} \tag{35}$$

we obtain the time evolution of the average wing temperature after the illumination:

$$T = (T_{max} - T_A)\, exp\left(-\frac{t}{mc_b\theta_E}\right) + T_A. \tag{36}$$

Both equations governing the step response incorporate a common parameter $mc_b\theta_E$, which takes a role of a time constant τ, defining the response speed of the process.

From the obtained differential equations, governing the heating and cooling of the wing, we ascribe a first order system behavior to our sensor. Thus, we fit the response equations to the induced sample's temperature change experimental data, measured using a thermal camera. The fitted curves are shown in Figure 6.1. The data is obtained for prolonged exposure of the sample from Figure 3.4 d) to the 660 nm EB. The fitting parameters τ for heating and cooling are calculated to be 343 ms and 360 ms, respectively, yielding a 352 ms average measurement of this sample's time constant.

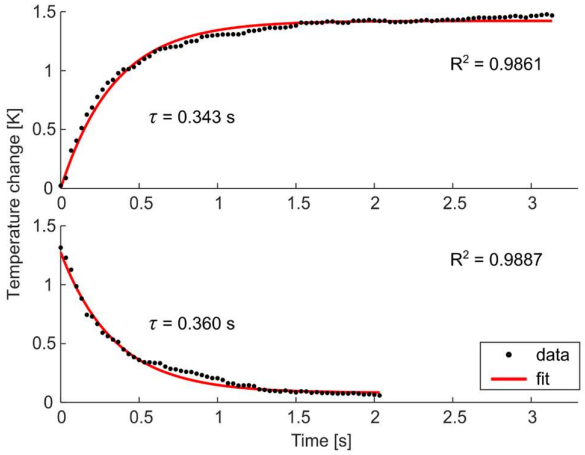

Figure 6.1 Time dependence of the wing sample's temperature change measured with a thermal camera, for heating (upper plot) and cooling (lower plot) periods.

Using the Laplace transform, the differential Equation (31) becomes:

$$\tau s\Delta T(s) + \Delta T(s) = P_{tot}(s). \quad (37)$$

Thus, the amplitude frequency characteristics is calculated by finding the modulus of a ratio $G(s) = \Delta T(s)/P_{tot}(s)$:

$$|G(j\omega)| = \frac{1}{\sqrt{1+(\omega\tau)^2}}, \quad (38)$$

where $\omega = 2\pi f$, and f is frequency. Finally, the attenuation in dB, denoted by Q_{dB} is:

$$Q_{dB} = 10\log_{10}\left(\frac{1}{\sqrt{1+(2\pi f\tau)^2}}\right). \quad (39)$$

The amplitude frequency response of a first order system is a monotonically decreasing curve, determined only by τ. For $\tau = 352\ ms$, the cut-off frequency for a $-3\ dB$ attenuation is calculated to be $0.8\ Hz$. Hihger limiting attenuations of -10 and $-20\ dB$ correspond to frequencies of 4.5 and $45\ Hz$, respectively.

6.2 Thermally induced deflection

The holographically observable response measures thermally induced displacements of both wing scales and the membrane to which they are attached. However, these displacements do not occur due to the observable average temperature increase, but due to the temperature gradient, formed across their lateral dimension. Even though this gradient is difficult to measure, we can adopt a simple physical model, concluding that at a steady state, it will be directly proportional to the average temperature increase of the scale/membrane [84]:

$$grad(T) \sim \Delta T_{avg}. \quad (40)$$

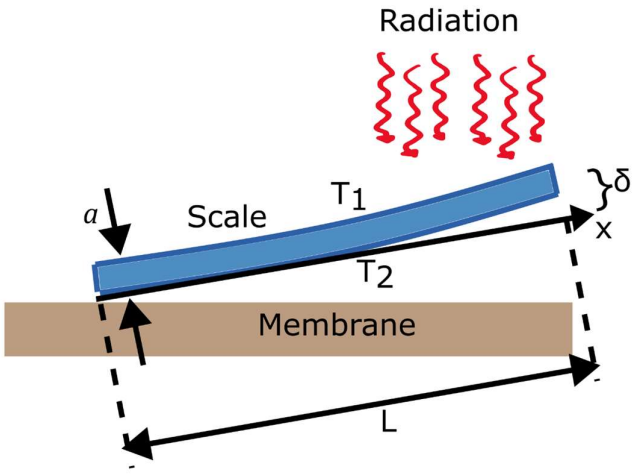

Figure 6.2 Illustration of a single wing scale as a cantilever beam, bending due to the induced temperature gradient.

Treating a single scale, fixed to a membrane at one end, as a cantilever beam of the length L, thickness a, and the coefficient of linear thermal expansion α, we can relate the displacement δ along the beam's longitudinal coordinate x:

$$\delta(x) = \frac{\alpha(T_2 - T_1)}{2a}x^2. \quad (41)$$

to the temperature difference of the scale's surfaces $(T_2 - T_1)$ [142]. An illustration of the scale as a cantilever beam is presented in Figure 6.2.

Similarly, the membrane displacement is proportional to the induced temperature difference of the back and front surfaces $(T_{front} - T_{back})$ as well, leading to a conclusion that the holographic response will finally be determined by the induced temperature gradients at any given time.

It is important to note however, that the assumption of equivalence between the displacement (controlled by the temperature gradient) and the average temperature change may break apart in the transient regime, as the previously outlined analysis represents a quasi-steady state treatment. To account for the heat propagation across the scale/membrane during transients in various experiment conditions, a more complex thermomechanical approach is necessary. Here, we present a simplified model, assuming a one-dimensional heat propagation problem through bulk material, as illustrated in Figure 6.3 a).

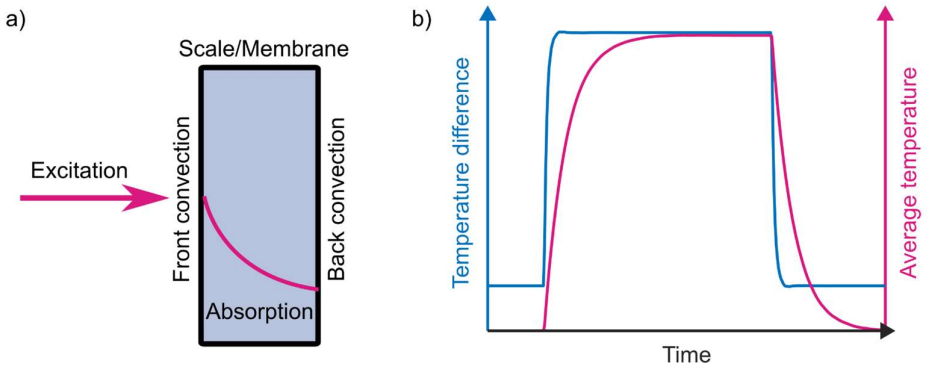

Figure 6.3 a) A simplified heat propagation model, used to calculate the time evolution of the temperature gradient; b) Simulated time evolution of membrane's/scale's average temperature and the induced temperature difference between the front and back surfaces.

The model predicts an exponentially decaying internal heat source inside of the scale/membrane, due to incident light absorption. The absorbed heat is then transported away to the surrounding air/mount due to the convective cooling on the wing's front, and convective/conductive cooling of its back surface. The time evolution of heat propagation, and the induced temperature gradient is obtained by solving the following partial differential heat equation using MATLAB:

$$\rho c \frac{\partial T_{(x,t)}}{\partial t} - \nabla \cdot \left(k \nabla T_{(x,t)}\right) = Q_{(x,t)}. \quad (42)$$

In the equation, ρ is the chitin density, c is its specific heat, k is the thermal conductivity, T is the absolute temperature, and t is time. Q denotes the internal heat source, present only during the period the exciting laser is turned on. The front/back surface heat transports are introduced in the model as boundary conditions. Solving the Equation (42) numerically provided the time evolution of temperature distribution across the scale/membrane. From these results, the average temperature of the scale/membrane, as well as the temperature difference $\delta t = T_{front} - T_{back}$ between its front and back surfaces are calculated. Their time evolutions are presented in Figure 6.3 b).

The results demonstrate similar response trends, with different response times for ΔT_{avg} and δt, leading to a conclusion that the holographic bending and the average temperature responses may differ in speed due to heat propagation through the structure.

6.3 Time evolution of the holographic response

The time evolution of the experimentally observed holographic response to the $660\ nm$ EBs with $200\ ms$ durations, recorded during the calibration measurements of Chapter 5 is presented in Figure 6.4 a). The response is observed to follow the same heating/cooling laws of Equations (33) and (36), confirming the validity of the previously established assumptions for this sample. The higher EB power induces a proportionally higher temperature gradient (and thus average temperature increase) causing an increase in the observed sample displacement. To examine the reproducibility of the time evolution trend, assumed to be independent of the incident EB power, all 10 response curves form Figure 6.4 a) are normalized. The average normalized response is plotted in Figure 6.4 b), together with the standard deviation of every response point. Considering the magnitude of response deviations, we conclude that the response trend is highly reproducible, both during the heating (Laser on) and cooling (Laser off) time periods, irrespective of the incident EB power. Due to a large thermal time constant τ of the examined sample, measured in Section 6.1, the response does not saturate during the $200\ ms$ exposure, giving a way to a further increase in sensitivity for prolonged exposure times.

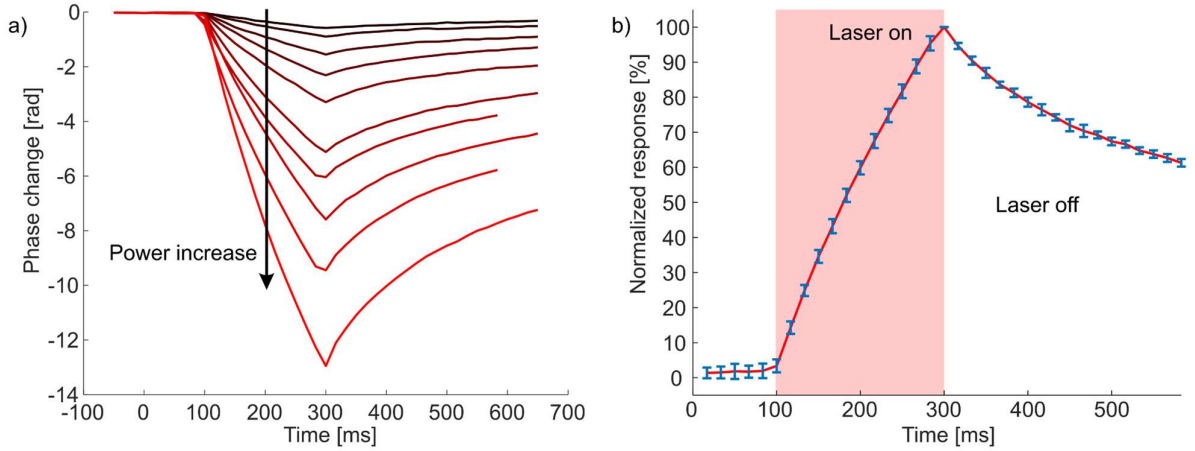

Figure 6.4 a) Time evolution of a holographic response to $200\ ms$, $660\ nm$ EB pulses with different powers; b) The average normalized response, with standard deviations.

The examined sample provides the benefits of a stable thermo-mechanical response and high sensitivity due to a high thermal resistance tape-plastic-wax adhesive structure between the sample and the aluminum. However, these benefits come at the expense of decrease in detectors response time, confining the bandwidth to very low frequencies. This tradeoff is common in thermal detectors such as bolometers, meaning that sensitive thermal radiation detectors are usually slow [143]. To address the issue of speed, experiments were conducted regarding the choice of adhesive material between the sample and the aluminum mount. The choice of the examined adhesive materials is outlined in Chapter 3.

The $2/3\ s$ recording time of the Nikon 1V3 camera proved to be a limiting factor in examining the temporal response from the start of the exposure to response saturation. Thus, the CMOS imager was changed to Basler acA2440-75um in further experiments regarding the temporal response examinations. The frame rate of the camera was set to $70\ fps$, a bit under the rated maximum of $75\ fps$, ensuring no loss of data during the recording. Due to low response time constants for the new samples, thermal camera measurements with a sampling period of $33\ ms$ did not provide useful information of the wing's temperature transient response.

The results showing the influence of the adhesive material on the rise and fall times of the normalized holographic temporal response are presented in Figure 6.5 a). The thermal time constants, presented in the Figure, are obtained by fitting the Equation (33) and (36) curves to data points near the transient, before long term response saturation. The comparison of these results to the previously presented response of Figure 6.1 leads to a conclusion that the change in the adhesive material resulted in a two to sixfold increase in response speed. The lowest average response time of only $53\ ms$ is obtained for a sample adhered with a heatsink pad. However, the adhesion of the pad to the sample in this case was subpar. Thus, a thin layer of wax with TiO_2 is the next best option, exhibiting proper adhesion and an average time constant of $55\ ms$. The time evolution of the illumination induced phase change of a freestanding wing, suspended in air is shown in Figure 6.5 b) for comparison (the result corresponds to the measurement of Figure 5.8 a)). While most of the samples from Figure 6.5 a) reach a steady state in less than $0.35\ s$, the freestanding sample requires an order of magnitude more time. On the other hand, it exhibits very high sensitivity, once again illustrating the compromise between response speed and measurement sensitivity.

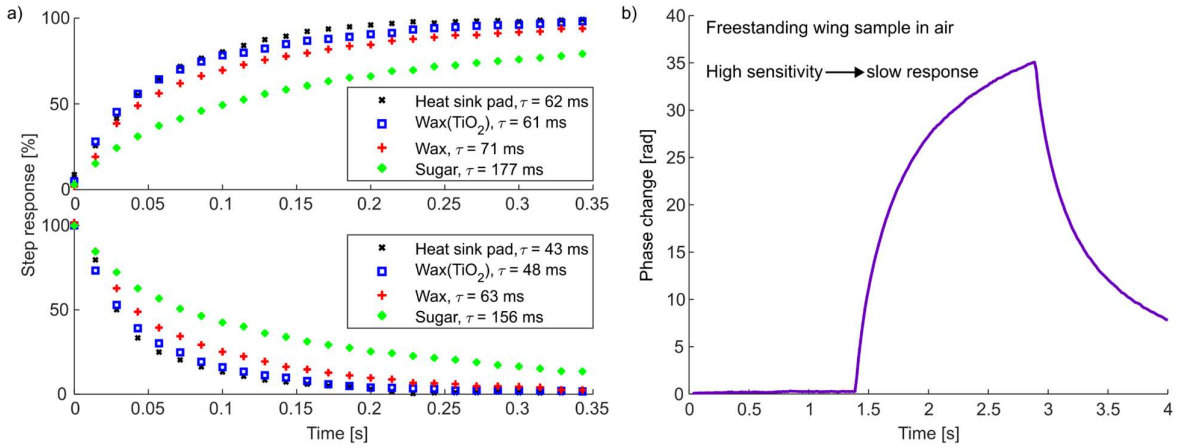

Figure 6.5 a) Normalized holographic temporal response: rising (upper) and falling (lower) edge response; b) Phase change of a freestanding sample.

According to Equation (39), the TiO_2 sample exhibits a $-3\ dB$ cut-off frequency of $5\ Hz$, a result which is comparable to the f_{-10d} cut-off of the sample from Figure 3.4 d). Furthermore, the f_{-10dB} for the TiO_2 sample reaches a value of $29\ Hz$, nearing the $30\ Hz$ acquisition frame rate of many commercially available cameras.

6.4 Thermoelectric control of the back surface temperature

As most thermal detectors are cooled to achieve faster response times, we tried to examine the influence of back surface temperature on the holographic readout of the proposed detector. To control the temperature of the sample, we developed a temperature-controlled mount with electronics for thermal regulation described in Chapter 4. The second holographic setup (shown in Figure 4.4) was used for the interrogation of the wing, due to the large dimensions of the mounted wing sample.

The sample's back surface temperature set by the temperature-controlled mount was varied in the range of 10 to 65 ℃ in different increments, depending on the behavior of the holographic response. Measurements of the response at the ambient temperature of 23 ℃, before the turn on of the temperature-controlled mount were conducted for reference purposes. The obtained results are shown in Figure 6.6 and Figure 6.7. The former shows a set of plots with time evolutions of the EB induced phase differences, obtained for different back surface temperatures. The latter shows the

obtained phase difference maps seconds after the response a)-d), and during the response e), f) obtained during the same experiments.

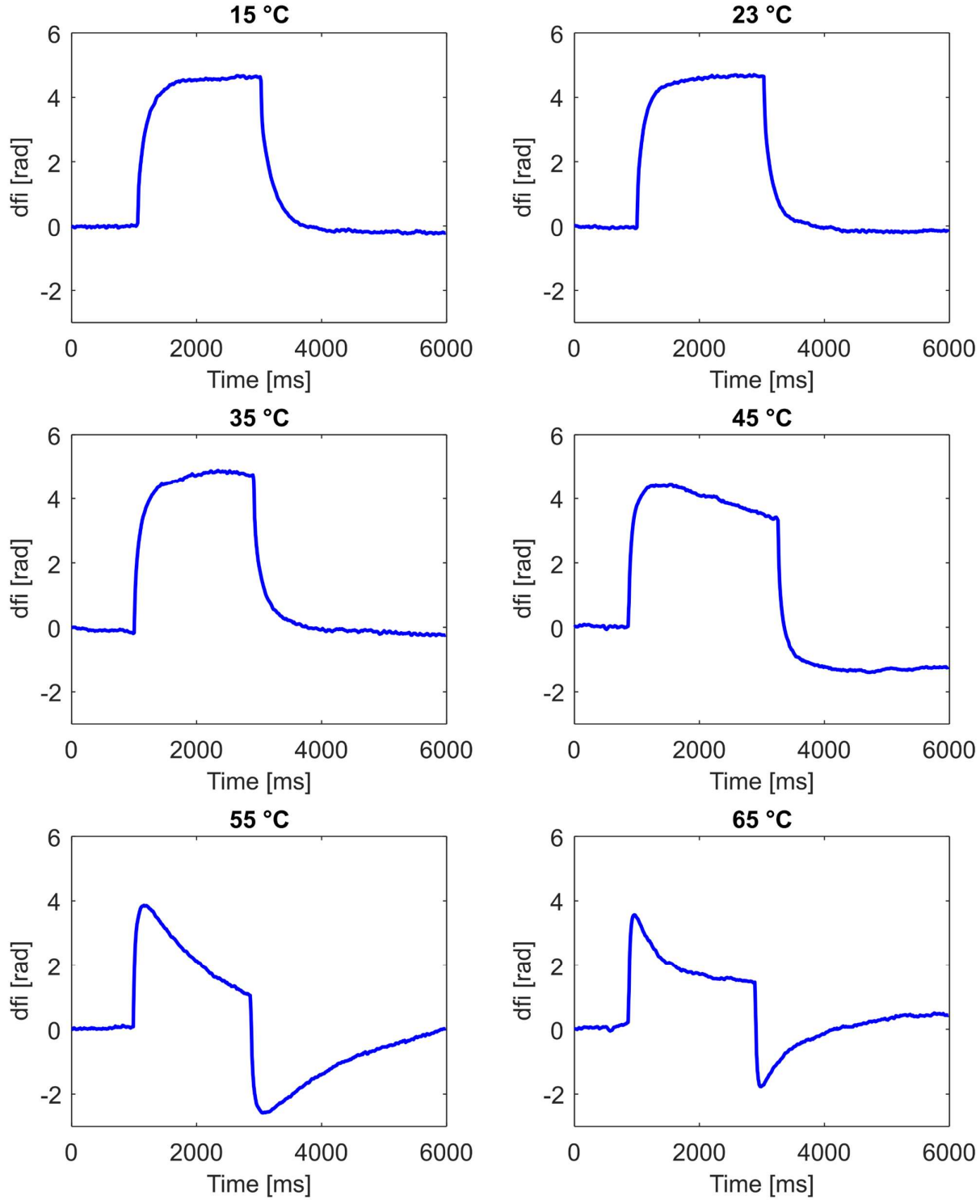

Figure 6.6 Time evolution of the induced phase change, shown for different sample temperatures, regulated using a system for temperature control presented in Figure 4.3. Ambient temperature is 23 ℃.

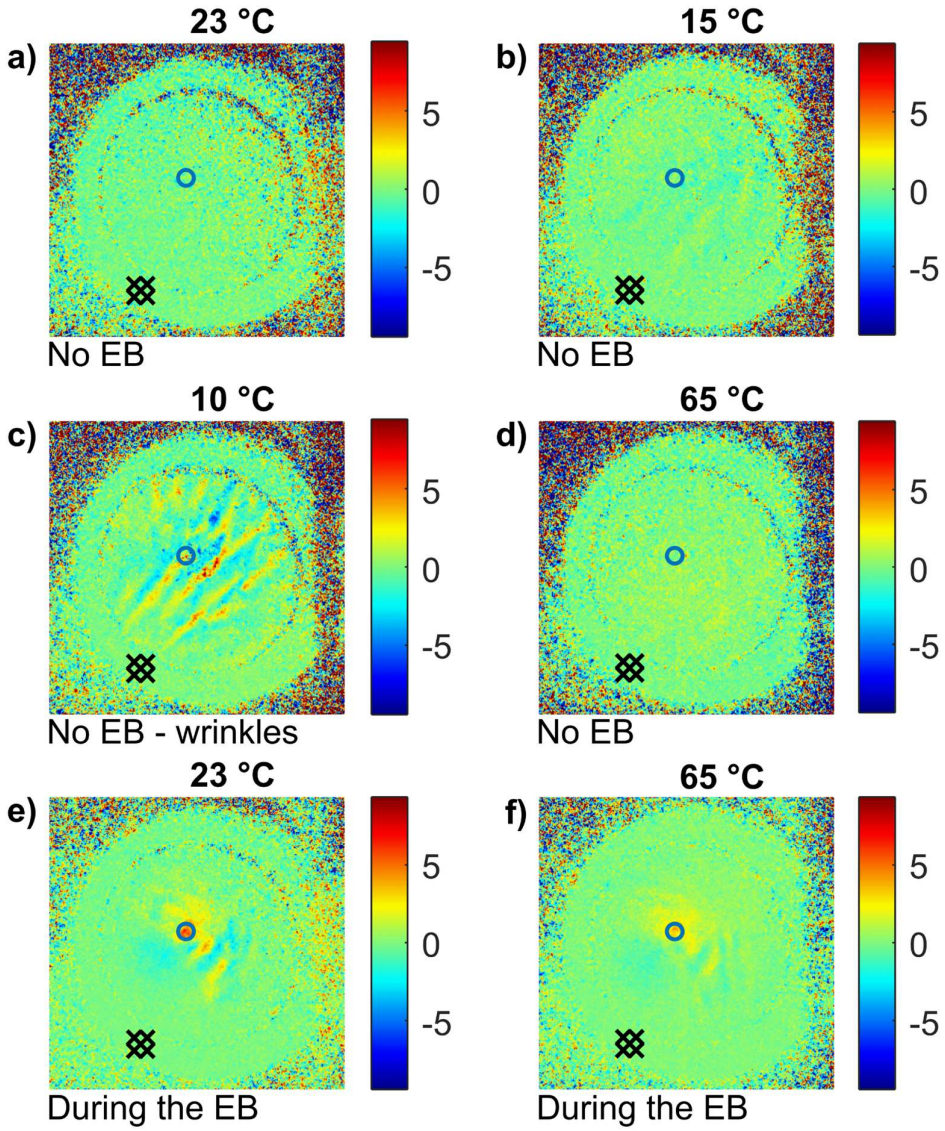

Figure 6.7 A phase difference map of the sample regulated to a temperature of: a) 23 ℃ in a steady state, long after the EB exposure; b) 15 ℃ in a steady state, long after the EB exposure; c) 10 ℃ in a steady state, long after the EB exposure; d) 65 ℃ in a steady state, long after the EB exposure; e) 23 ℃ during the EB exposure; f) 65 ℃ during the EB exposure. The blue circle shows a region where the response is analyzed, while the black "x" points mark a region on the sample holder where the reference phase difference offset is calculated and subtracted from the whole image.

The response of the wing without temperature control (23 ℃) is in agreement with previously obtained results. An active decrease of the sample's temperature to 15 ℃ showed no apparent influence on the time evolution of the sample's response, as the trends for 23 and 15 ℃ (Figure 6.6) are close to identical. Increasing the temperature to 35 ℃ lead to a similar conclusion. However, decreasing the temperature further (10 ℃ and below) resulted in unwanted wrinkling of the sample during measurement, rendering those temperatures useless for the current measurement approaches. Figure 6.7 c) demonstrates the aforementioned wrinkling, present long after the EB was turned off. Higher temperatures demonstrate no such effect, as shown in Figure 6.7 a), b) and d).

The spatial distribution of the EB induced phase response during the exposure is observed not to change with increasing sample temperature, as shown in Figure 6.7 e) and f), leading to a conclusion that no spatial response disturbing effects take place at higher temperatures. However, an unexpected change in time evolution trend due to sample's temperature increase to 45 ℃ and beyond was observed during measurement, presented in Figure 6.6. The response at higher temperatures exhibits an abrupt increase at the rising edge of the excitation, reaching a peak and decreasing to a new steady state value. Similarly, the falling edge of the excitation resulted in an abrupt decrease in the induced phase difference to negative values, after which the phase approaches zero from the negative side. The time after the peak, required to reach the new steady state value is observed to depend on the set sample temperature, where higher temperatures resulted in a faster response. The observed trend thus resembles having a high-pass filtering nature, reacting strongly to sudden excitation changes.

To explain the behavior of the proposed sensor at higher back surface temperatures, we need to take into account the time evolution of the induced temperature gradient governing the bending, by numerically solving the Equation (42). The simulation results at higher back surface temperatures, depicting the average, and gradient temperature changes are shown in Figure 6.8.

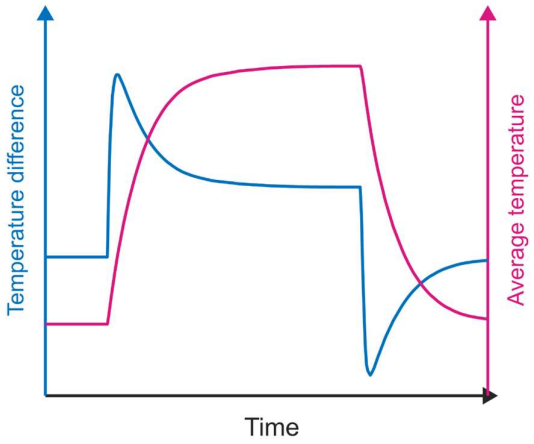

Figure 6.8 Simulated time evolution of the temperature gradient and average temperature change, where sample's back surface heating changes the heat transfer coefficients.

To obtain the results of Figure 6.8, mimicking the experiment, the temperature at the boundary of the sample's back surface was increased. Furthermore, the introduced heat transfer coefficient at the wing's back surface was decreased compared to the simulation results shown in Figure 6.3 b). Before the illumination, the heat flows through the sample from the back to the front. When the EB is turned on, another component of the heat flow from the front to the back is introduced. Due to the exponential decay of absorption, it heats the front surface more than the back. This induces a gradient compared to the steady state. The heat then propagates from the front to the back, accumulating there due to the decreased back surface heat transfer coefficient. This decreases the gradient, causing the decrease in the holographic response after the peak, observable at the rising edge.

The temperature dependence of the heat transfer coefficient, although often neglected for smaller temperature variations, is a known phenomenon [144,145]. However, due to the complex nanoscale structure of the wing scales influencing the laws of heat transfer greatly [146], detailed investigation into this effect was deemed outside the scope of this thesis. It is noteworthy that while the temperature gradient exhibits a change in trend due to the back surface heating, the simulated average temperature follows similar trends in both Figure 6.3 b) and Figure 6.8. The only difference is the offset (steady state) temperature, determined by both the ambient temperature and the heater.

Based on the results of the temperature control experiments, we conclude that the wing's temperature should be stabilized near the ambient to achieve the intended operation. Setting the wing's temperature too high or low either decreases the sensitivity, degrades the response, or completely changes its dynamics. This further emphasizes the benefits of the proposed detector compared to the cooled infrared FPAs. Not only does it not require cooling, but its uncooled operation provides the optimum response.

Chapter 7. Spatial response and image formation

When characterizing an imaging sensor, one of its most important qualities (if not the single most important quality) is the ability to record images, i.e. to record, and faithfully reproduce (usually digitally) the distribution of light intensity. In conventional image acquisition systems, this ability is characterized by multiple parameters, and quantified using well established universal metrics. The goal of this chapter is to attempt to apply these principles to our, rather unusual detector, providing a figure of merit of imaging capabilities of the holographically interrogated butterfly's wing. To achieve this, the main holographic setup described in Chapter 5 is utilized.

Some of the usual parameters of the image acquisition system affecting the image formation are its working distance, field of view, depth of field and depth of focus, and ultimately spatial resolution. Although this is not a complete list, it is sufficient for the upcoming discussion. The first four parameters are determined by the design of the objective lens, its aperture and focal length. These are not applicable to our sensor, as no objective lens is currently used due to the directivity of LD EB light. On the other hand, spatial resolution is regarded as the capability of the whole imaging system to resolve details. It is determined by a multitude of system design parameters including, but not limited to the objective lens, lighting, and the imaging sensor itself. The influence of the latter is usually defined by its pixel size and pitch. The resolution is usually expressed in units of line pairs per millimeter (lp/mm), a unit of spatial frequency, signifying the critical drop of contrast (blur) of the otherwise ideal black and white line pair. Furthermore, we can usually discern between two types of resolution, image plane resolution ξ_{im} and object plane resolution ξ_{ob}. The former represents the limit of resolving capabilities in the image plane, after the imaging optics, while the latter limits the resolvable details of the imaged object. The two resolution types are connected through system magnification.

The theoretical upper limit in a system's resolving ability is the diffraction limit, derived from the Rayleigh criterion as the point where the two adjacent Airy patterns arising from diffraction are no longer distinguishable [147,148]. The limit in distance d_{res} between resolvable points (inversely proportional to spatial frequency determining resolution) is defined by the f-number ($f/\#$) of the imaging lens, and the wavelength λ of the incoming light:

$$d_{res} = 1.22 \cdot \lambda \cdot f/\#; \tag{43}$$

e.g. for λ in the visible light range and an $f/4.0$ lens, the d_{res} is between 1 and 4 μm.

However, reaching a diffraction limited performance is not simple, as each component in the system has a non-ideal, generally complex transfer function, known as the optical transfer function (OTF), usually attenuating higher spatial frequencies. This attenuation is quantified through the magnitude of the OTF, known as the modulation transfer function (MTF):

$$OTF(f_x, f_y) = \left|OTF(f_x, f_y)\right| \exp\left\{-j \cdot \operatorname{atan}\left(\frac{Im\{OTF(f_x, f_y)\}}{Re\{OTF(f_x, f_y)\}}\right)\right\}$$
$$MTF = \left|OTF(f_x, f_y)\right|, \qquad PTF = \operatorname{atan}\left(\frac{Im\{OTF(f_x, f_y)\}}{Re\{OTF(f_x, f_y)\}}\right) \tag{44}$$

where f_x and f_y are the spatial frequencies, and PTF is the phase transfer function, present due to the complex nature of the OTF. The MTF of the system is a product of the MTFs of individual system elements. This product defines the transfer of contrast (modulation) from the object to the image plane. When quantifying this drop of contrast, a value of spatial frequency is usually given, for which a predefined contrast (50%, 20% or 10%) is reached.

To investigate the imaging capabilities of the proposed butterfly's wing, the overall response uniformity of the wing will first be tested. The MTF of the wing, imaged holographically, will be measured, and limiting frequencies for characteristic MTF values will be given as a figure of merit. Finally, the provided examples of images, acquired using the proposed sensor, will be considered as conclusive proof of the sensor's imaging performance.

7.1 Response uniformity

To test the response uniformity of the butterfly's wing, an illumination source with a well-known intensity distribution and low level of high spatial frequency details was required. An expanded Gaussian beam was a reasonable choice in these experiments. It has a well-defined beam profile, readily available in a large number of metrology lasers today. Furthermore, the expansion of the Gaussian beam using a lens, or a mirror ensures the maintenance of the beam's Gaussian nature, while changing the beam parameters [149,150]. The intensity of the Gaussian beam is given by equation:

$$I(\rho, z) = I_0 \left[\frac{W_0}{W(z)}\right]^2 \exp\left\{-\frac{2\rho^2}{W^2(z)}\right\}, \tag{45}$$

where z and ρ are the axial and radial coordinates respectively, while I_0 denotes the beam intensity on the optical axis ($\rho = 0$) at the beam waist ($z = 0$). $W(z)$ is the beam radius, exhibiting a minimum W_0 at the beam waist, and increasing following the expression:

$$W(z) = W_0 \sqrt{1 + \left(\frac{z}{z_R}\right)^2}. \tag{46}$$

where $z_R = \frac{\pi W_0^2}{\lambda}$ is the Reyleigh range. Another benefit of the Gaussian beam is that it is easily characterized by multiple methods, out of which the knife edge method [151,152] stands out as one of the simplest. Alternatively, it can be imaged using a camera without a lens as a beam profiler.

To modify the Gaussian beam before the sample illumination, and monitor its power, a new excitation section (ES2) is implemented within the excitation section region of Figure 4.1 a). It is comprised of a $632.8\ nm$ He-Ne laser, outputting a Gaussian beam with a $5\ mW$ rated output power, as shown in Figure 7.1. The beam is expanded using a converging lens, before it is split into the signal and the monitoring PD part. A simple shutter is constructed using a microcontroller, a servo motor with a dedicated motor driver, and a piece of cardboard, to enable synchronization between the acquisition software and the excitation.

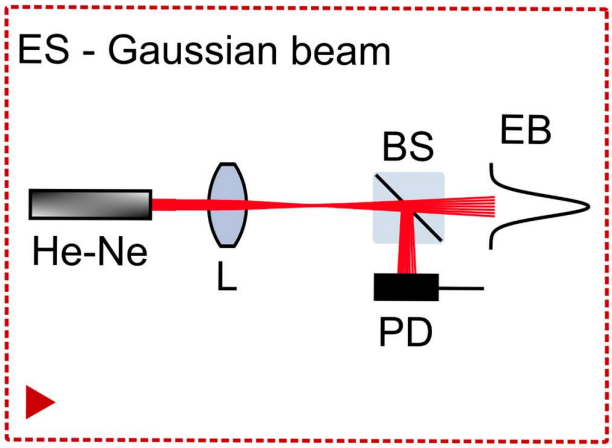

Figure 7.1 The second ES, used for the expanded Gaussian beam illumination. L – lens; BS – beam splitter; PD – photodiode; EB – excitation beam.

The beam was expanded to cover the whole surface area of the 7 mm diameter sample, thus characterizing its response uniformity with a single shot exposure. In order to characterize the beam's intensity profile after the expansion, the expanded beam was photographed using a Nikon 1V3 digital camera without a lens. The acquired image, and its three-dimensional representation are shown in Figure 7.2. The images are pseudo-colored to emphasize the Gaussian nature of the beam's intensity profile. The exposure time of the camera was lowered well below the saturation limit of the 8-bit depth pixels (255) to ensure linear operation.

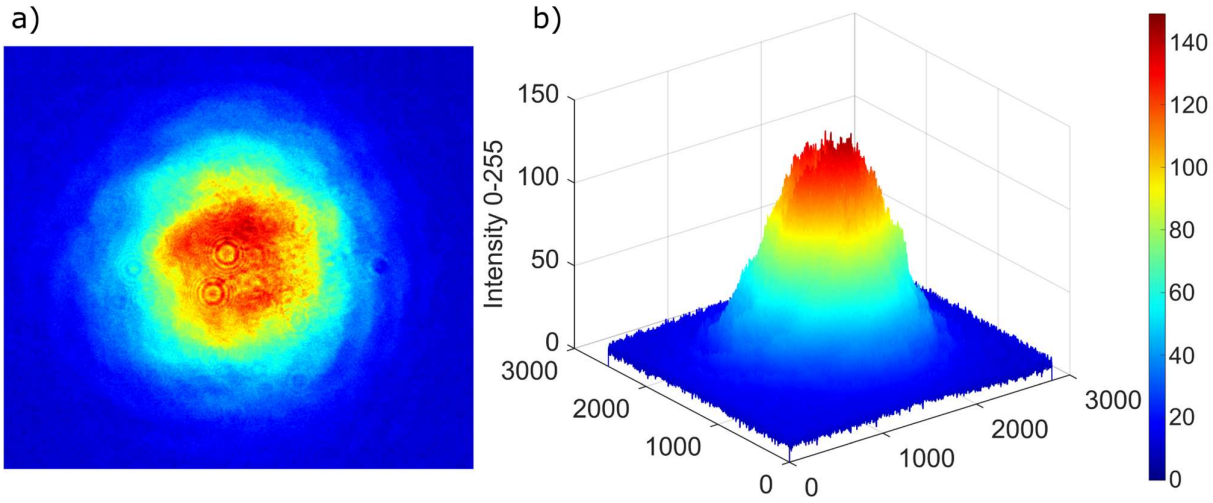

Figure 7.2 A photograph of a Gaussian EB, used for single-shot characterization of the spatial response of the wing: a) two-dimensional; b) three-dimensional image.

The presented two-dimensional intensity distribution was fitted to a two-dimensional Gaussian distribution:

$$F(X,Y) = C_1 \cdot \exp\left\{-\frac{1}{2}\left[\left(\frac{X-x_0}{\sigma_1}\right)^2 + \left(\frac{Y-y_0}{\sigma_2}\right)^2\right]\right\} + C_2, \qquad (47)$$

assuming a general case of different beam widths in two orthogonal directions, i.e. an elliptical Gaussian beam. Parameters $x_0 = 3.20\ mm$ and $y_0 = 3.53\ mm$ represent the offsets of the Gaussian's center with respect to the $(0,0)$ coordinates of the image, while $\sigma_1 = 1.18\ mm$ and $\sigma_2 = 1.16\ mm$ denote the respective standard deviations. $C_1 = 121.6$ and $C_2 = 10.09$ are introduced to account for the maximum value of the Gaussian, and the offset due to the background illumination. The R^2 value of 0.9788 suggests a good fit of the data to the distribution. The total width of the beam was measured (based on the pixel pitch of the camera $2.51\ \mu m$) as the width of $3 \cdot W(z)$, or $6 \cdot \sigma_{1,2}$, noting that this region of the beam contains 99% of the beam's total power. The results show that the beam is $6.96\ mm$ and $7.06\ mm$ wide in the horizontal and vertical directions respectively – expected values as it was set to cover a $7\ mm$ sample. The difference in widths is rather small – under 1.5%, and can be attributed to the laser itself, a small misalignment during the camera setup, or the artefacts induced by the converging lens.

Exposing the wing to the aforementioned Gaussian EB resulted in a phase difference distribution which is shown in Figure 7.3.

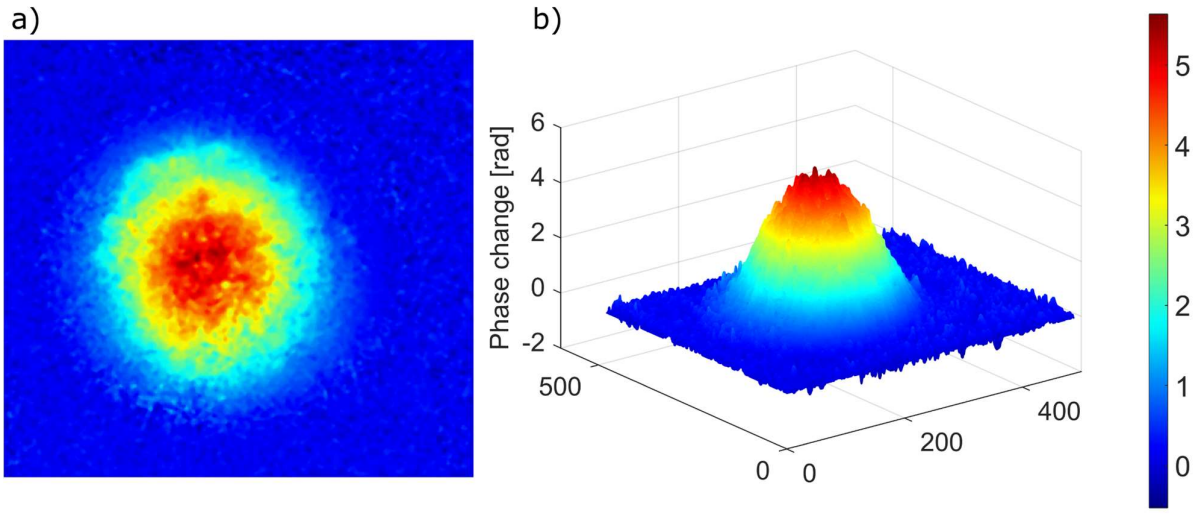

Figure 7.3 A phase response of the wing, induced by a Gaussian beam from Figure 7.2: a) two-dimensional; b) three-dimensional image

The presented phase difference is a result of a $617\ ms$ exposure time. Once again, the results are pseudo-colored and presented in two and three dimensions to enable the comparison of the wing's light induced response with the excitation shown in Figure 7.2. Using the same fitting procedure as before, $7.48\ mm$ horizontal and $8.55\ mm$ vertical beam widths were measured. The R^2 value of 0.9755 was obtained, indicating a high goodness of fit. The remaining fitting parameters are $x_0 = 4.45\ mm,\ y_0 = 3.81\ mm,\ \sigma_1 = 1.42\ mm,\ \sigma_2 = 1.25\ mm,\ C_1 = 5.24\ rad,\ C_2 = 0.05\ rad$. The reconstruction of the holographic images was done using a Shifted-Fresnel method, with a scale factor of $s = 10$. Knowing the $2.51\ \mu m$ pixel pitch of the Nikon 1V3 used for hologram recording, this was expected to yield a pixel distance of $25.1\ \mu m$ in the reconstruction plane. However, taking this value for granted can easily result in an erroneous distance measurement in the reconstructed image. This is due to the error in estimation of the true physical distances between the camera and the sample z, and the reference point source and the sample z_0. While the image with an erroneous z, z_0 pair can still appear sharp (in focus), it exhibits some degree of magnification, influencing the intended pixel distance of the reconstruction. To account for this effect in our measurements of beam widths, the pixel distance in the reconstruction plane was calibrated manually by fitting a circle to a reconstructed

image of a sample. Knowing that the radii of the imaged sample and the fitted circle are $3.5\ mm$ and $195\ pix$ respectively, we estimated the pixel distance in the reconstruction plane to be $17.9\ \mu m$.

The higher beam width values then expected are a consequence of the unwanted lateral heat transport, and the collective membrane and scales displacement, causing the broadening of the otherwise sharper transitions in the EB light intensity, later limiting the spatial resolution. Furthermore, the measured horizontal and vertical beam widths differ by 14.3% this time. This result is an order of magnitude worse compared to the previous measurement using a CMOS detector. The difference occurs due to the inherent asymmetry of the pixels of the proposed sensor – wing scales – as their length is twice the size of their width. The higher overestimation of the beam width is naturally obtained for the vertical axis, set along the length of the scales.

The presented results show that, although the butterfly's wing is not a completely uniform imager, it can reproduce the trend of the illumination distribution it is exposed to. Also, the particular sample used in these experiments showed no areas insensitive to light, apart from the regions nearing the edges. The wax in these regions covered the top layer of the membrane and scales, limiting their movement, while also limiting the movement of the adjacent membrane. Furthermore, the edges were burned during the laser cutting of the sample decreasing their sensitivity. The short video, illustrating the time evolution of the wing's Gaussian induced displacements during the exposure is provided in the supplementary of the online version of the paper [91].

7.2 Resolution measurements

The most commonly used techniques for resolution measurements of optical imaging systems require the utilization of specially designed resolution test charts. The charts contain elements which, when illuminated, produce excitation with varying spatial frequency. Depending on the chart design, the variation in spatial frequency may be continuous (Star target) or have predefined discrete values (USAF 1951). Charts further differ in their ability to simultaneously test the resolution of the system across the whole field of view, or in their ability to simultaneously test the system's resolution in different directions. Finally, it is important to emphasize that all of these approaches test the system's resolution in the plane of the object – ξ_{ob}, and can provide the information regarding the drop of contrast transfer with increasing spatial frequency [153,154].

Unlike the aforementioned approaches, there are methods which rely on illumination using a light source mimicking a single point, line or an edge transition (Heaviside excitation). Based on the system's response to this type of excitation, a MTF of a system can be calculated using numerical methods. Out of the three stated excitations, the edge transition is by far the easiest to implement experimentally. All that is required is a well-defined, sharp edge transition between the light and dark regions, or vice versa (keeping in mind that the light region should not saturate the sensor). From the acquired response to an edge illumination, the edge spread function (ESF) of the system is calculated. Knowing the ESF, a system's line spread function (LSF) is obtained by numerical differentiation:

$$LSF = \frac{d}{dx}\{ESF\}. \tag{48}$$

The LSF itself represents the system's impulse response along the axis perpendicular to the edge. Thus, by Fourier transforming the LSF, MTF is calculated:

$$MTF = \mathcal{F}\{LSF\} \tag{49}$$

along the dimension defined by the orthogonal to the edge transition [155]. While numerical differentiation of Equation (48), in its simplest form, comes down to subtraction of successive array elements, the Fourier transform is once again numerically implemented using the FFT algorithm.

Due to the nature of the outlined method, some conclusions can be drawn. Firstly, the method directly measures the image plane resolution – ξ_{im}. Additionally, the sampling of the ESF is limited by the pixel pitch of the imaging sensor. To overcome this limitation, the oversampling of the ESF is proposed, by the introduction of a small angle (usually $4 - 6°$) between the edge illumination and the pixel array. This approach is known as the slanted edge method, utilized as a standard form of MTF measurement in imaging systems [156–160].

The slanted edge method is adapted to measure the MTF of the holographically interrogated butterfly wing as an imaging sensor. The wing is illuminated using an expanded EB, with one half masked using a nontransparent screen with a straight edge. A photograph of the mounted sample, illuminated by both the green laser light for holographic interrogation and the red EB used for slanted edge measurements is shown in Figure 7.4 a) with the induced phase response after the hologram reconstruction. The usual oversampling techniques were unnecessary as the holographic method provided the phase difference maps with sampling of $15\ \mu m$, six to thirteen times smaller than the wing scales ($100 - 200\ \mu m$) – the resolution limit of the sample.

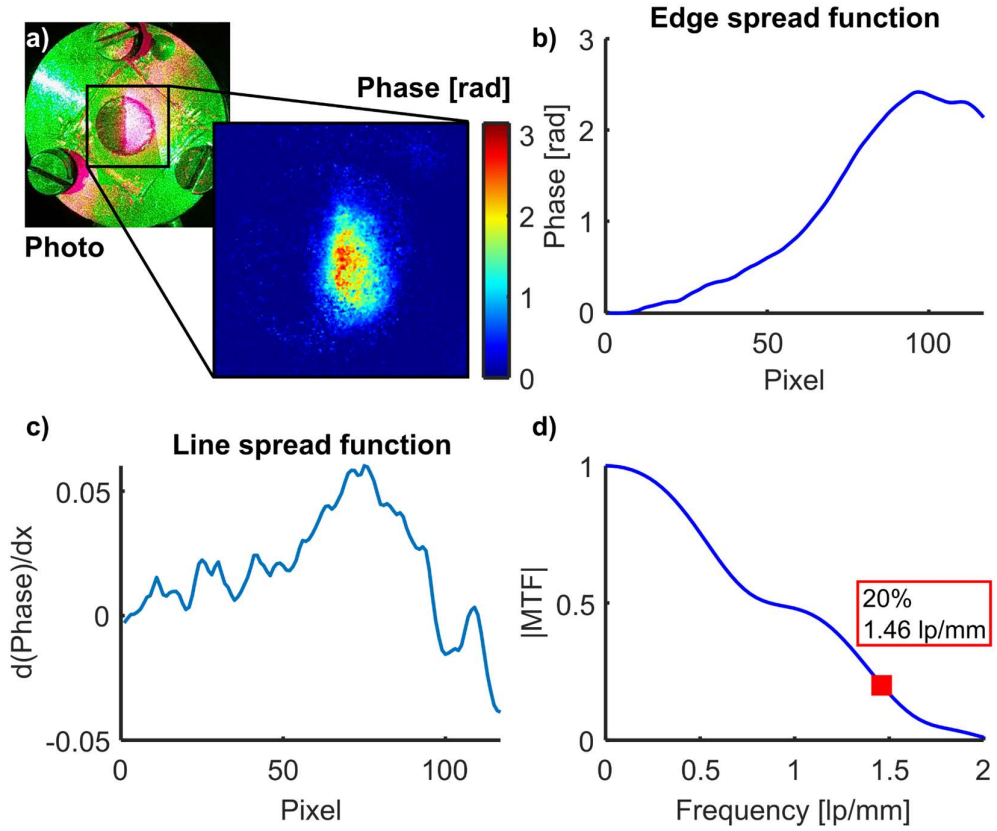

Figure 7.4 MTF measurement of the wing; a) photograph and the acquired phase difference image of the edge illuminated wing; b) ESF of the wing; c) LSF of the wing; d) MTF of the wing with a marked 20% point.

Figure 7.4 b) shows the wing's ESF, obtained by averaging 50 rows along the edge of the phase map and filtering using a 10 pixel moving average filter. The averaging and filtering were necessary due to noise, present in part due to the coherent nature of both the EB and the holographic technique. Numerical differentiation of the ESF yielded the LSF, shown in Figure 7.4 c). The LSF exhibits a peak near the middle of the edge because of the sign change of the ESF's second derivative. However, the LSF becomes negative due to the decrease of phase values near the end of the ESF, in

the illuminated region. The decrease is caused both by the drop in intensity of the EB, and the drop in sensitivity of the wing near the sample boundary.

The Fourier transformation of the LSF resulted in the MTF, shown in Figure 7.4 d). The spatial frequencies of 0.9 and $1.46\ lp/mm$ corresponding to the 50% and 20% MTF amplitude values (contrast) respectively, are obtained from the presented MTF curve. These values, although quite small when compared to commercially available image sensors, are near the $2.5\ lp/mm$ theoretical limit of the wing. The limit is imposed by dimensions of the wing scale pixels, as one line pair can theoretically be imaged with two $200\ \mu m$ adjacent scales. The discrepancy between theory and experiment in this case occurs due to the movement of the membrane interconnecting the scales, causing crosstalk. Additionally, crosstalk is increased by inevitable lateral heat transport, heating the "dark" scales nearing the illuminating edge.

Given the unusual nature of the proposed sensing mechanism, further experiments testing the sensor's resolving capabilities were beneficial in order to verify the results of the slanted edge method. Thus, an experiment measuring the wing's point spread function (PSF) was devised. Unlike the LSF, the impulse response of the system along one of its axis, the PSF represents the system's impulse response in two dimensions. Knowing the PSF, a two-dimensional MTF can be calculated using the Fourier transformation.

The PSF is usually measured by focusing an imaging system to a point source illumination and analyzing the spread of the imaged point induced by the system. However, due to the lack of an objective lens in our system, this was not possible. Instead, the PSF of the holographically interrogated butterfly's wing was acquired by imaging a Gaussian beam, focused to a narrow point on the wing. To provide the required point source illumination, the $632.8\ nm$ output of a $5\ mW$ He-Ne laser was utilized. In order to avoid damage due to heating and problems with phase unwrapping algorithms due to a large and rapid displacement of the illuminated wing scales, the beam was attenuated to $830\ \mu W$ prior to focusing.

In order for the lens focused Gaussian beam to be regarded as a point source illumination, it was necessary to decrease its radius w to the values comparable with the dimensions of the wing scales. Focusing the beam too much (under $100\ \mu m$) would heat only a part of a single scale, causing an effect localized to a single pixel. The opposing case of a beam with dimensions larger than a couple of scales contradicts the assumption of a point source illumination. Thus, the optimal beam radius values were on the order of $\sim 200\ \mu m$. The measurements of the focused beam radius were performed using the knife edge method. In this method, the examined Gaussian beam is increasingly covered using a sharp non-transparent knife edge (swept with a micrometer head precision). The power of the transmitted portion of the beam is recorded using a PD. The expected power P, vs. edge position x dependence is governed by equation:

$$P(x) = P_{offset} + \frac{P_{max}}{2}\left(1 - erf\left(\sqrt{2}\left(\frac{x - x_0}{w}\right)\right)\right), \qquad (50)$$

where P_{offset} represents the non-zero offset power due to the background illumination, P_{max} is the total power of the beam, and erf is the error function.

The setup, used for Gaussian beam focusing, with the added knife edge measurement equipment is presented in Figure 7.5 a). The setup is integrated within the experiment depicted in Figure 4.1 a) as an ES. During the PSF measurement, the knife edge and PD are removed, and the wing sample is put in their place. The knife edge measurements of a Gaussian beam focused on the wing are presented in Figure 7.5 b). The red and blue markers represent the data obtained for the horizontal and vertical beam axes respectively. The Equation (50) curves are fitted through the points with R^2 values over 0.99. The measured beam radii for the horizontal and vertical directions are 167

and 202 μm, correspondingly. These results match the aforementioned requirements regarding the dimensions of the point source illumination.

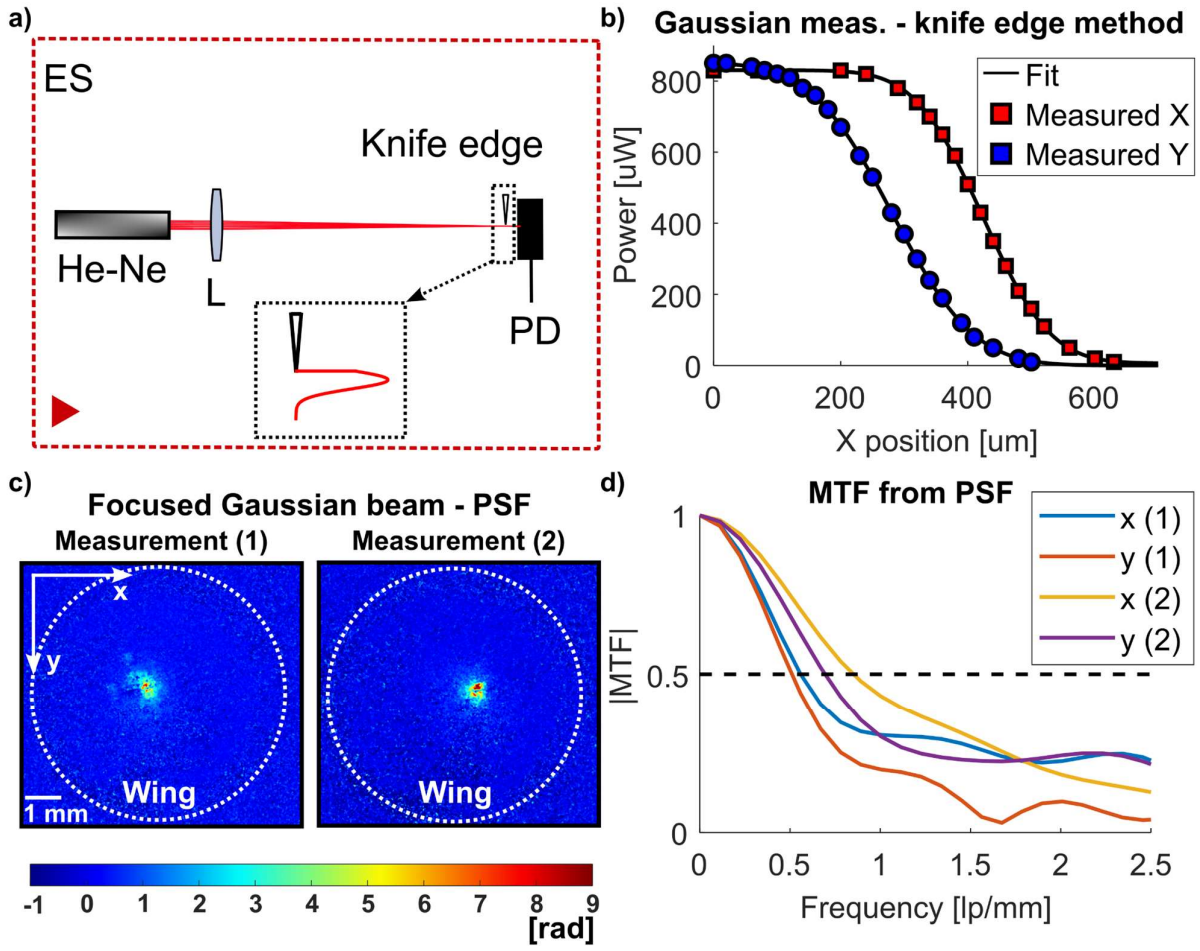

Figure 7.5 Determination of MTF using a focused Gaussian beam: a) a knife edge setup (the third ES) for Gaussian beam width measurement; b) knife edge measurement results; c) focused Gaussian beam at two different spots on the wing; d) MTF curves along x and y axis for measurements (1) and (2); PD – photodiode.

The point source induced phase difference images, representing the PSFs are presented in Figure 7.5 c). Two different sets of results are recorded for two different positions of the point source illumination on the wing, to ensure comparative analysis of different parts of the wing. The two measurements are denoted by numbers (1) and (2) in Figure 7.5 c) and d). Line profiles across the light induced response, along the horizontal and vertical axes (denoted by x and y in Figure 7.5 c) and d)) were further regarded as orthogonal PSFs. The profiles were Fourier transformed to find the respective MTFs, plotted in Figure 7.5 d). The MTFs, although not identical, follow a similar trend, which corresponds to the slanted edge results of Figure 7.4 d). A small difference between the two sets of results is discernable, owing to the nonuniformity of the response of the natural structure. The dashed line in the plot denotes the representative MTF 50% value, measured to be in the 0.5 to 0.9 lp/mm spatial frequency range, similar to the slanted edge result. Both PSF measurements exhibit a slightly higher limiting resolution along the horizontal axis. This is due to the predominantly vertical orientation of the scales (a consequence of the positioning during the mounting procedure), as their length is approximately twice their height.

From the aforesaid resolution measurements, a drop of contrast is expected for spatial frequencies ranging from 0.5 to 1.5 lp/mm, with very low contrast expected for frequencies higher than the upper boundary. This result was put to a test when the wing was illuminated using a periodic bright and dark fringe pattern with a spatial frequency of approximately 1 lp/mm. The total power of the utilized 660 nm illumination was 12 mW. The photograph of the illuminated sample is shown in Figure 7.6 a). The obtained phase difference image after a 100 ms exposure is shown in Figure 7.6 b). The phase image shows a discernable periodic phase change pattern which corresponds to the periodic line illumination. The light induced phase changes drop on average towards the sample boundaries, as discussed previously for the expanded Gaussian beam. The line profile across the periodic phase change is shown in Figure 7.6 c). The length axis of the plot is calculated based on the pixel distance in the reconstruction plane. The profile is obtained by averaging 70 successive rows in the exposed region of the phase difference image. It evidently shows multiple peaks and dips corresponding to the illuminated and nonilluminated spatial regions. The contrast of the profile varies depending on the part of the wing which is illuminated. The highest contrast value of 73% is calculated around the fourth peak from the left in the distribution. By performing the FFT of the signal the peak around the 1 lp/mm frequency is observed (as shown in the inset of Figure 7.6 c)). The value is obtained without taking into account the prior knowledge of the line frequency, thus confirming spatial measurement capabilities of the wing as an image sensor.

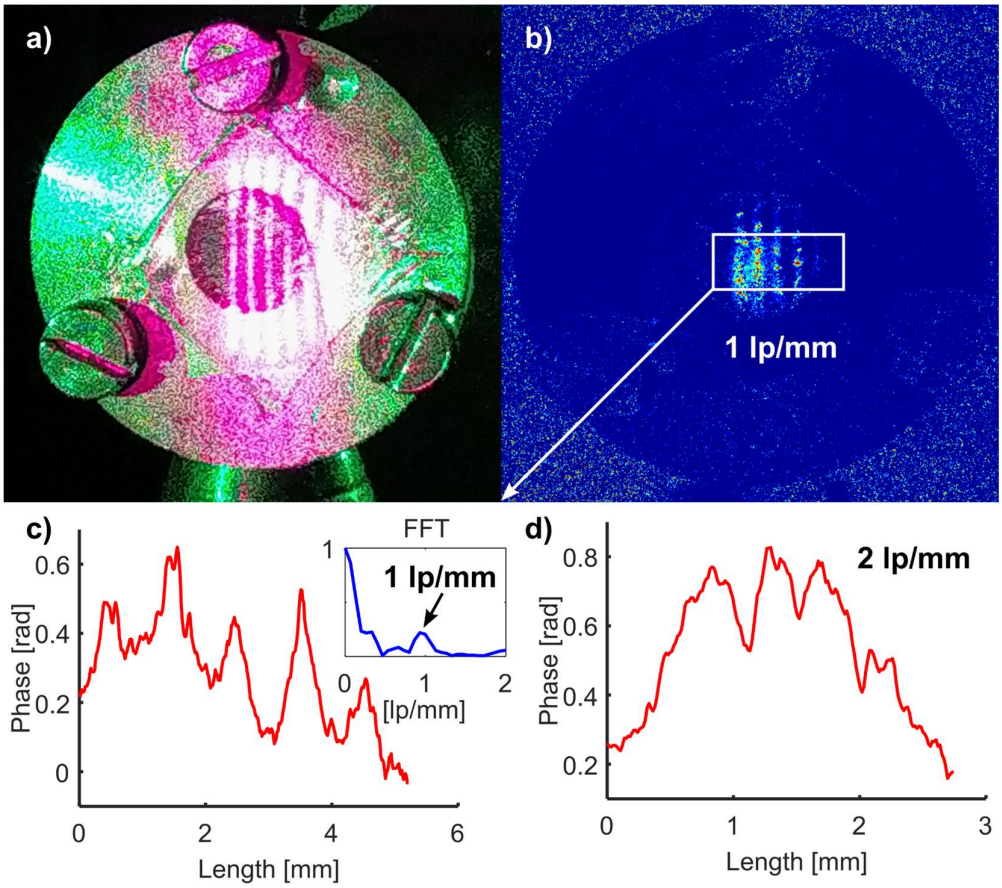

Figure 7.6 A wing sample, illuminated with periodic light distribution (EB): a) photograph; b) phase difference image; c) averaged phase line profile across the 1 lp/mm periodic lines; the inset shows the FFT of the signal; d) averaged phase line profile across the 2 lp/mm periodic lines.

The increase in frequency of the periodic lines to a value of 2 lp/mm expectedly resulted in a significant drop of contrast. The total beam power during this measurement was lowered to 5 mW,

to account for the increased illumination intensity. Using the same procedure as before, the line profile across the periodic phase change for the 2 lp/mm case is shown in Figure 7.6 d). The bright lines are almost indistinguishable, superimposed over a high average phase change. Thus, the previously established conclusions regarding the limits of the wing's spatial resolution are valid.

7.3 Image acquisition

The previous Chapters conclusively demonstrated the ability of the wing to detect visible and NIR light. The previous subsections of this Chapter established the limits and discussed the limiting factors regarding the spatial response of the wing as an imaging sensor. The final stage in response characterization of the proposed imaging sensor is image acquisition. To investigate this, a new ES shown in Figure 7.7, is devised. The presented ES is integrated within the holographic setup shown in Figure 4.1 a). The ES is comprised of a three-lens system, with a mask between the lenses used for defining the shape of the illuminating EB. The first lens is a negative lens, used only for beam expansion. The expended beam is masked, and further transferred to the wing using the second and third lens, both positive. The three-lens system for image generation and transfer to the wing is utilized instead of a two-lens system to acquire additional degrees of freedom during the set up. In this way, the beam dimensions and focusing can be performed freely by the movement of different lenses, ensuring that the ES components do not get in the way of the beams utilized for holographic imaging. Due to the construction of the ES, the image projected to the wing is inverted with respect to the shape displayed on the mask.

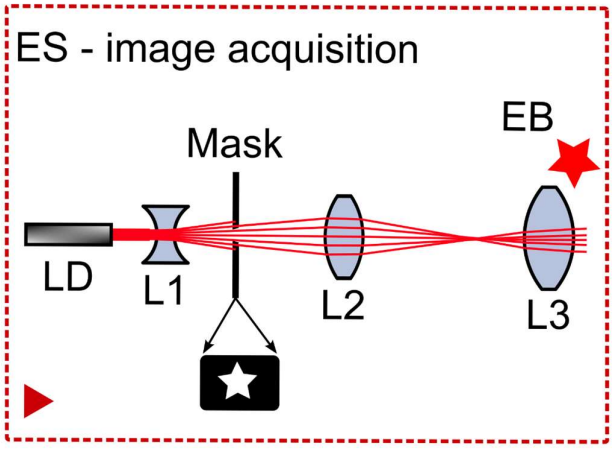

Figure 7.7 The fourth ES, used for image acquisition tests. LD – laser diode; L1, L2, L3 – lenses; EB – excitation beam.

Using the aforesaid ES for image acquisition, results shown in Figure 7.8 are obtained. Each measurement was performed using a different mask. Photographs of the sample illuminated using masks showing a group of concentric circles, an X sign, and a star are presented in Figure 7.8 a), c) and e), respectively. Their corresponding phase difference images, acquired by the wing, are shown in Figure 7.8 b), d) and f). A comparative analysis of both the photographs and the induced phase changes leads to a conclusion that the object's shape is discernable from the images acquired by the wing. On the other hand, no easily discernable illumination induced changes in the intensity images of the holograms were observed during measurements, as shown in Figure 7.8 g).The light induced temperature change for a rotated star shaped illumination was imaged using a thermal camera, and shown in Figure 7.8 h). Similarly, the light induced temperature change due to the X shaped EB was previously presented as an example thermal image in Figure 4.8, Section 4.3. Notably, the distribution of the light induced temperature change is observed to follow the shape of the EB as well.

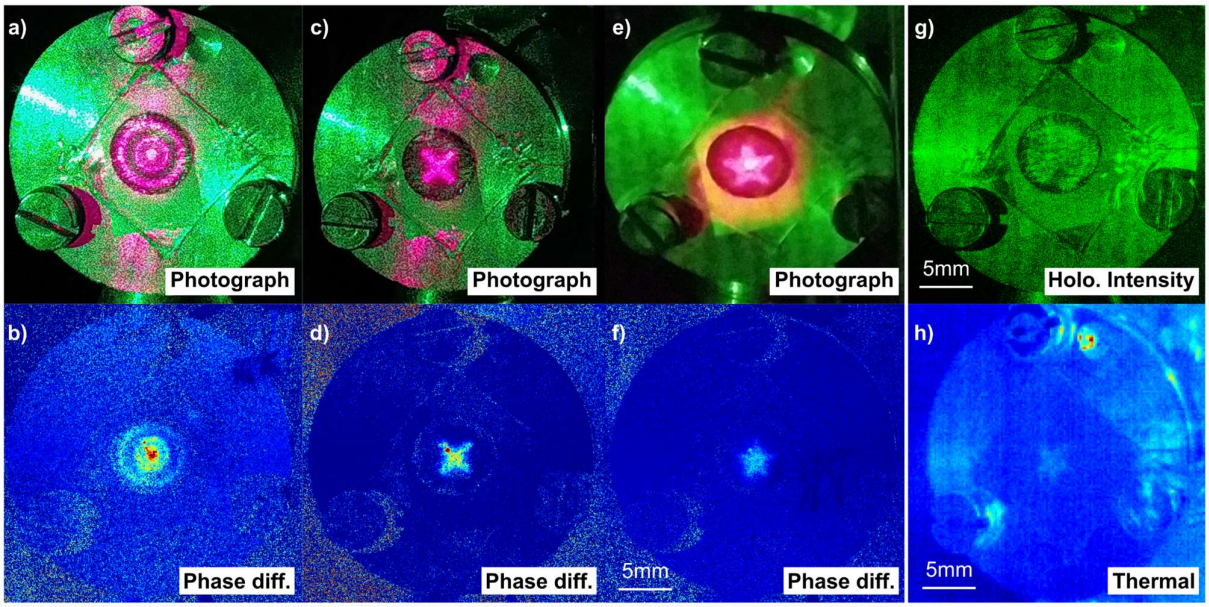

Figure 7.8 A demonstration of image acquisition using a butterfly's wing: a) photograph of the sample illuminated by 660 nm laser radiation shaped like a group of concentric circles; b) phase difference induced by the concentric circles, imaged holographically by the wing; c) photograph of the sample illuminated by 660 nm laser radiation shaped like an X sign; d) phase difference induced by the X sign, imaged holographically by the wing; e) photograph of the sample illuminated by 660 nm laser radiation shaped like a star; f) phase difference induced by the star, imaged holographically by the wing; g) hologram intensity, showing no change due to illumination; h) thermal image, showing a star induced temperature change.

To further demonstrate the light detection capacity of the proposed sensor, the measurement of total beam power for star shaped and X shaped beams was conducted using the algorithm proposed in Section 5.2. Firstly, the area of the wing, and the reference background point were selected, as shown in Figure 5.6 c). The average phase change φ_{avg} over the total wing area was calculated for the hologram corresponding to the 200 ms EB exposure, as per instructions of Section 5.2. Finally, the beam area S_{EB} was calculated by multiplication of the number of illuminated pixels (pixels exhibiting a phase change higher than the predefined threshold) with the pixel area in the reconstruction plane ($15.06 \times 15.06\ \mu m$). Knowing the sensitivity for the 660 nm wavelength $K_{660nm} = 1.93\ \frac{rad \cdot mm^2}{mW}$ the total EB power was calculated according to equation:

$$P_{tot} = \frac{\varphi_{avg} S_{EB}}{K_{\lambda}}, \tag{51}$$

derived from Equation (27). The results of the total EB power measurements using a wing, and a reference PD are compared in Table 2. Keeping in mind that the wing is a natural biological structure, and that the image acquisition measurements were conducted about a year after the calibration measurements, the calculated relative errors are remarkably low. However, the measurement is susceptible to variations due to the manual selection process of the wing and background areas (Figure 5.6 c)). This can be remedied in practical applications by fixing the parameters of the holographic setup and reconstruction, defining the wing area once, and then performing the calibration.

The presented phase images, acquired by the holographically interrogated wing, provide a conclusive proof of its imaging capacity. The images are of the highest quality achievable with the utilized natural structure. Thus, we can conclude that the proposed imaging principle is not currently

limited by the proposed readout principle, but by the material itself. With future advances in fabrication of new materials inspired by the *Morphos*, the capacity of the proposed imaging principle is expected only to increase.

Table 2 Comparison of the total power measurements of the EB using a PD and using a wing.

$\boldsymbol{K_{660nm} = 1.93\ \frac{rad \cdot mm^2}{mW}}$	**Power - PD** $[\boldsymbol{mW}]$	**Power – wing** $[\boldsymbol{mW}]$	$\boldsymbol{\varepsilon}$ [%]
Star	3.86	3.65	-5.4
X sign	3.6	3.7	2.7

Chapter 8. Discussion

The previous Chapters 5, 6 and 7 contain both the results and discussion of spectral, temporal and spatial response characterization of the presented imaging sensor, individually. In turn, the discussion in Chapter 8 is introduced to provide a broader context to the overall imaging capacity of the approach presented in this thesis, commenting on its advantages and shortcomings compared to the previously published state of the art. The presented holographically interrogated butterfly's wing FPA is by nature a thermal electromagnetic radiation detector. As such, it provides fundamental benefits of a naturally broad spectral range (which is not bandgap limited), and no cryogenic cooling required by the photon detecting FPAs. Compared to microbolometers, the proposed detector presents a viable potential alternative, providing the benefits of no on-chip ROIC, known to have a significant noise and reflection influence on the readout. Yet, similar tradeoffs, regarding the sensitivity and response time, limit the performance of both the microbolometer and the wing scale pixels. Based on its working principles the proposed detector highly resembles the microcantilever FPAs discussed in Section 1.2 of Chapter 1. The major difference between the two is the fact that our approach uses a natural cantilever structure – a wing scale, with no functionalization, and no bimaterial properties. The list of some of the most high-performing approaches in the field of microcantilever FPAs are presented in Table 3.

Table 3 The reported performance parameters of the state-of-the-art microcantilever sensors. The superscript * represents theoretical results.

Reference	*Type*	*Interrogation type*	*Readout technique*	*Pixel pitch* $[\mu m]$	*Response time* $[ms]$	*Sensitivity* $\left[\frac{nm}{K}\right]$	*Imaging*
Hunter et al. [30]	Artificial	Electrical	Capacitance to voltage	$25-50$	$5-10^{*}$	$300-400^{*}$	Yes
Gong et al. [57]	Artificial	Optical	Angle to intensity	~150	/	42	Yes
Lim et al. [32]	Artificial	Optical	White light interferometry	100	/	180	No
Guo et al. [51]	Artificial	Optical	Angle to intensity	~180	/	77.4	Yes
Dong et al. [50]	Artificial	Optical	Angle to intensity	120	70	< 138	Yes
Grbović et al. [35]	Artificial	Optical	Angle to intensity	75	6	50	Yes
Grbović et al. [47]	Artificial	Optical	Position sensitive detection	220	$53.5-62.5$	$500-1000$	No
Our approach	Biological	Optical	Displacement to phase change	~200	$55\ ms$	478	Yes

Looking over the reported results, the methodology by Hunter et al. stands out as the main competitor to our approach due to the exceptionally fast and sensitive response, and the smallest pixel pitch. However, the remarkably low response time was estimated theoretically, while the details of the sensitivity measurements and the measurement data were not provided [30]. Furthermore, the electronic readout of their FPA inherently comes with the aforementioned ROIC limitations compared to the optical alternatives. Finally, the reported sensor fabrication yielded 15 % of "dead" pixels, unresponsive to the incoming light. The results reported by Grbović et al. most wonderfully illustrate the compromise between the sensor's sensitivity and response time. Their first solution exhibits the $6\,ms$ time constant, nearly ten times faster compared to our $55\,ms$ value. Yet, their $50\,nm/K$ sensitivity is nearly ten times lower than the sensitivity we report [35]. On the other hand, their second solution (with complex pixel structures) demonstrates values comparable to the results of our unmodified bioderived detector, both in speed and sensitivity. Yet, this time it was without the concrete imaging demonstration of the fabricated FPA [47].

It is important to note that one of the main limitations of our holographic readout approach compared to the "angle-to-intensity" measurements is the duration of hologram reconstruction. Currently, our approach allows for continuous hologram acquisition with the acquisition time sampling limited by the utilized CMOS detector. However, the hologram reconstruction is conducted separately, as it requires a couple of seconds per hologram on an AMD Ryzen 7 4800H processor. This limits the performance of our approach in real-time imaging applications. On the other hand, this boundary is not physical, and is purely determined by the performance of the processing hardware. Lower reconstruction times, reaching the real-time operation are expected to soon be achieved by utilizing the rapidly growing dedicated hardware such as the graphics processing units (GPU) and the field programmable gate arrays (FPGA).

The "angle-to-intensity" technique does come with its limitations, as discussed in Chapter 1. It is extremely sensitive to the reflecting angle of the fabricated cantilevers. The readout light exhibiting specular reflection from the cantilevers with angles which deviate from the projections is filtered out in the focal plane of the collecting lens, resulting in nonresponsive pixels throughout the FPA. On the contrary, the wing scales act as highly diffuse reflectors, enabling a simple simultaneous holographic interrogation of all of the pixels, no matter the initial scale angle. Thus, no "dead" pixels problem was observed. The response of the wing scales is not completely uniform over the sample area, as discussed previously in Section 7.1. Similarly to the microcantilever and microbolometer FPAs, the practical applications of the *Morpho* butterfly imager would require a periodic nonuniformity correction, compensating for the varying response of the individual pixels.

The comparison of our (infrared) light detection method to other approaches utilizing *Morpho* butterfly wings [83,85,86] proved to be more difficult to quantify than the comparison with the published work on microcantilever imagers due to the innate difference in the proposed readout principles. The choice of the spectral reflectance change $\Delta R(\lambda)$ as a readout quantity [83,85,86] comes with the difficulty of simultaneous precise measurements over the sample area, limiting the applicability of such a sensor as an FPA. Moreover, the response is expected to be nonlinear to the incoming infrared light, unlike the calibration functions demonstrated in this thesis. For example, the most sensitive of the three principles, relying on water vapor desorption [86], will inevitably exhibit the sensitivity drop, and the response saturation as soon as there is no more adsorbed water vapor. This limits the dynamic range of the proposed sensor. To compare the frequency response of the same method with our own, we calculate the expected induced displacement of $2.486\,\mu m$ for the same light induced temperature difference of 5.2 ℃ as reported in [86]. This displacement corresponds to a phase change of $51.87\,rad$ (based on Equation (24)). Noting that the $0.046\,rad$ phase noise was measured in Chapter 5, we calculate the limiting frequency of $54\,Hz$ for a signal to noise ratio of 60 (based on the time constant of $55\,ms$ and the Equations (38) and (39)). This is very close to the $60\,Hz$ value reported in [86].

When analyzing the performance of thermal imagers, the noise equivalent temperature difference (NETD) is often reported. In this thesis we do not report the NETD parameter, as it would require the utilization of a uniform black body emitter. It is important to emphasize that the NETD corresponds to the noise equivalent temperature difference of the emitting object, and not the radiation induced temperature difference of the sensor itself. Otherwise, the results can be misinterpreted [83,85,86].

Another major distinction between the previously published approaches using *Morphos* and the method of this thesis arises from the choice of the *Morpho* butterfly species, and the sample functionalization. While the methods reported in papers [83,85,86] functionalize the natural structure of a *Morpho sulkowsky* wing with the SWCNT, gold, or water vapor, the results of this thesis are obtained for an unmodified natural structure of a *Morpho didius* wing. This circumvents the complex procedures of sample doping prior to mounting and measurement. Additionally, based on the previously published absorption spectra for both the *didius* and the *sulkowsky* species, the unmodified *didius* wing is expected to outperform the *sulkowsky*, at least in the visible spectral region, as the *didius* exhibits higher absorption due to pigmentation [75].

If we were to compare the performance results of the presented sensor with the state-of-the-art photon detecting silicon CMOS/CCD FPAs, the latter would come out superior in regard to both the physical dimensions, spatial response, speed and sensitivity in the $0.4-1\ \mu m$ spectral range. Their pixel pitches easily reach $\sim 1\ \mu m$ dimensions, enabling megapixel resolutions at $\sim 1\ cm$ chip dimensions. This significantly outperforms the resolving capabilities of both our *Morpho* approach, as well as the generally utilized thermal detectors such as microbolometers. The high-speed readout of the top performing silicon imagers allows for acquisitions up to thousands of frames per second, compared to our $< 100\ Hz$ frame rates. Their dynamic ranges are usually 10 to $20\ dB$ higher than the $50-60\ dB$ limits, currently observed for the holographically interrogated wing. It is interesting to note that while the silicon imagers offer both the (low performing) rolling shutter, and the (usually preferable) global shutter exposure/readout options, the innate nature of holographic interrogation enables only the global shutter acquisition, beneficial to the imaging of moving scenes. On the other hand, the main advantage of our detector is its potential for a very broad spectral response. In this thesis, the sensitive illumination induced displacements were observed in a $0.4-1.45\ \mu m$ wavelength range. The response for wavelengths outside of the aforementioned range was not tested due to the lack of proper light sources, enabling light intensity control (required for calibration) at specific wavelengths. However, the spectral limits for detection are expected to go far beyond these values, as supported by the other proposed *Morpho* infrared detectors. Furthermore, the spectral response of the proposed bioderived FPA is governed by the specimen absorption (as shown in Chapter 5), which is not fundamentally limited, and directly determines the sensitivity. In turn, the absorption is susceptible to precise tailoring using the already proposed materials such as SWCNT or gold for surface functionalization. This makes the proposed sensor highly versatile, enabling simultaneous detection in multiple spectral regions. Even though the response in the visible and infrared was mostly discussed throughout the preceding text, the response in the UV is expected to highly outperform the silicon FPAs, due to the presence of melanin in the unmodified wing, as well as the energy increase of the incoming photons, as recognized and discussed in detail in Chapter 5.

Chapter 9. Conclusions and outlook

This thesis presents a novel bioderived thermal imager, aiming to advance the sensitive broad spectral range detection. The imager owes its functioning principles to the mechanism of radiation absorption, heating the wing scales of a *Morpho didius* butterfly wing acting as microcantilever pixels on a naturally available FPA. The heated scales bend/displace due to the induced thermal gradient, providing a measurable output quantity which is proportional to the intensity of the incoming radiation. The work of this thesis goes beyond the simple proof of concept radiation detection, providing a thorough characterization of the imaging sensor's response. After the results and performance limitations were established and discussed, we further demonstrated the image acquisition using the unmodified butterfly's wing as an FPA, showcasing its imaging capacity.

To measure the light induced displacements, we employed the well-established measurement techniques of digital holographic interferometry, relying on their high sensitivity, and two-dimensional imaging capability. Simultaneously, thermal infrared imaging was used to examine the light induced temperature changes, correlating them to the holographic response. Two different holographic setups were employed/developed, and dedicated hardware and software solutions were devised to accommodate for the requirements of the wing's response characterization experiments. The development of a versatile programmable system on a chip current source with high output currents was inspired by the drive requirements of the infrared LDs used for wing excitation. The LabVIEW application with synchronized parallel loops for wing excitation, hologram and thermal image acquisition was custom designed. The numerical hologram reconstruction methods with phase unwrapping and filtering were implemented in MATLAB, allowing for scalable, reduced noise reconstructions.

Using digital holography, the highly linear response trend, connecting the scale's displacement to the incoming light's input power was observed. A novel numerical output quantity was proposed, providing a useful calibration result irrespective of the choice of the hologram reconstruction method and parameters. Further calibration tests at different wavelengths throughout the visible and NIR parts of the spectrum ($0.4 - 1.45\ \mu m$ wavelengths of incident light) showed that the response sensitivity closely follows the spectral dependence of the wing's absorption, allowing us to conclude that our bioderived thermal imager shows great promise in broad spectral range detection. The holographic interrogation approach performed exceptionally well, resulting in the phase noise corresponding to $2\ nm$ displacements. This enabled our sensor to achieve the $50 - 60\ dB$ tested dynamic range. In future research, even higher values are expected by implementing advanced low-noise holographic techniques, such as white light holography.

Based on the observed results of simultaneous holographic and thermal imaging, a simple physical model of the sensor's response was devised. It was shown that the treatment of the sensor as a first order system, heated by the power of the absorbed incident light, results in a high agreement between the theory and most of the conducted experiments. Discrepancies were observed for a temperature-controlled sample, where the interplay of the sample structure and the heat flow dynamics governed by the heat equation resulted in unexpected response trends. These unusual

experiments allowed us to conclude that the uncooled wing sample shows the already optimized response, exhibiting no need for further cooling or heating. Based on the first order system dynamics, the time constant was introduced as a quantity which determines the sensor's frequency response bandwidth. Through the thesis, different mounting choices for the wing were tested, resulting in different response sensitivities and time constants. The freestanding wing, mounted in air, was shown to be incredibly sensitive, although very slow. It further showed the high degree of membrane bending and twisting, limiting the applicability of such a sensor in image acquisition tasks. Contrary to the freestanding wing, multiple adhesive materials were used to fix the wing samples to the aluminium mount, decreasing the unwanted membrane movement. This allowed us to test the optimal material satisfying both the proper adhesion and low time constant requirements. The wax with TiO_2 as an adhesive material performed the best, enabling the proposed detector to reach the near 30 Hz response at -10 dB attenuation, thus making it comparable to most of the commercially available detectors.

The tests regarding the spatial response of the bioderived FPA examined its uniformity, demonstrating its ability to faithfully reproduce the slowly varying intensity distribution of an expanded Gaussian beam. Further experiments applied the standard MTF measurement methods, yielding an estimated MTF 20 % resolution limit of $1.46\,lp/mm$. The value is close to the $2.5\,lp/mm$ limit, set by the 200 μm scales, acting as pixels. Similar limiting values are observed using several different resolution measurement approaches, validating the imagers spatial resolving performance. The thesis culminates with the representative imaging demonstrations, acquired using the natural FPA – the holographically interrogated butterfly's wing. The results showed some response variations between the individual scales, to be remedied by the nonuniformity correction which is common to all thermal detectors.

The proposed holographically interrogated bioderived sensor is shown to outperform the artificially manufactured microcantilever FPAs with reported imaging demonstrations, either in response speed, sensitivity, or both. When compared to the alternative *Morpho* based infrared detection ideas, our approach demonstrated inherent advantages of easily realized imaging, no necessity for wing functionalization, as well as the benefit of a linear response.

Up to this point several research directions were deemed preferable in the next development steps of our bioderived detector. They can generally be divided into two main groups. The first group will strive to miniaturize and perfect the experimental setups for the wing FPA interrogation, taking them to the portable device level. Novel combinations of techniques for illumination and interrogation, such as back (ventral) side illumination will be investigated, hoping to offer superior performance. The second group of future research goals is aimed toward analyzing and improving the response of the natural structure. The holographic microscopy setups are to be employed in the analysis of the light induced response of individual scales, discerning the contributions of scale vs. membrane deformations to the overall observable displacement. Apart from this, sample functionalization through chemical and/or physical pixel modification will be investigated, exploring the new limits of the enhanced broad spectral range detection.

References

1. Compton, K. T. High voltage. *Science (1979)* **78**, (1933).
2. Fernald, R. D. Casting a genetic light on the evolution of eyes. *Science (1979)* **313**, (2006).
3. Nilsson, D. E. The evolution of eyes and visually guided behaviour. *Philosophical Transactions of the Royal Society B: Biological Sciences* **364**, (2009).
4. Land, M. F. & Nilsson, D. E. General purpose and special purpose visual systems. in *Invertebrate Vision* (2006).
5. Darwin, C. The Origin of Species, by Means of Natural Selection, or the Preservation of Favored Races in the Struggle for Life. *The Crayon* **7**, (1860).
6. Guarnieri, M. The Rise of Light - Discovering Its Secrets [Scanning Our Past]. in *Proceedings of the IEEE* vol. 104 (2016).
7. Durini, D. *High Performance Silicon Imaging: Fundamentals and Applications of CMOS and CCD Sensors*. (2019). doi:10.1016/C2017-0-01564-1.
8. Roth, M. M. A brief history of image sensors in the optical. *Astronomische Nachrichten* (2023) doi:10.1002/asna.20230066.
9. Shin, D. *et al.* Photon-efficient imaging with a single-photon camera. *Nat Commun* **7**, (2016).
10. Wolff, L. B. & Andreou, A. G. Polarization camera sensors. *Image Vis Comput* **13**, (1995).
11. XIV. Experiments on the refrangibility of the invisible rays of the sun. *Philos Trans R Soc Lond* **90**, (1800).
12. Rogalski, A. History of infrared detectors. *Opto-Electronics Review* **20**, (2012).
13. Rogalski, A., Martyniuk, P. & Kopytko, M. Challenges of small-pixel infrared detectors: A review. *Reports on Progress in Physics* **79**, (2016).
14. Telops. High-Performance FAST Cameras. https://www.telops.com/products/high-performance-fast-cameras/.
15. Rogalski, A. *Infrared and Terahertz Detectors, Third Edition*. *Infrared and Terahertz Detectors, Third Edition* (2019). doi:10.1201/b21951.
16. Fusetto, S., Aprile, A., Malcovati, P. & Bonizzoni, E. Readout IC Architectures and Strategies for Uncooled Micro-Bolometers Infrared Focal Plane Arrays: A Review. *Sensors* **23**, (2023).
17. Rogalski, A., Kopytko, M., Hu, W. & Martyniuk, P. Infrared HOT Photodetectors: Status and Outlook. *Sensors* **23**, (2023).
18. Norton, P. R. Infrared detectors in the next millennium. in *Infrared Technology and Applications XXV* vol. 3698 (1999).

19. Barnes, J. R. *et al.* A femtojoule calorimeter using micromechanical sensors. *Review of Scientific Instruments* **65**, (1994).

20. Choi, J. *et al.* Design and control of a thermal stabilizing system for a MEMS optomechanical uncooled infrared imaging camera. *Sens Actuators A Phys* **104**, (2003).

21. Enemuo, A. N., Chaudhuri, R. R., Song, Y. & Seo, S. W. Thermo-optic sensor based on resonance waveguide grating for infrared/thermal imaging. *IEEE Sens J* **15**, (2015).

22. Razeghi, M., Dehzangi, A. & Li, J. Multi-band SWIR-MWIR-LWIR Type-II superlattice based infrared photodetector. *Results in Optics* **2**, (2021).

23. Khandekar, C., Jin, W. & Fan, S. Nanophotonic detector array to enable direct thermal infrared vision. *Opt Express* **30**, (2022).

24. Gao, J., Nguyen, S. C., Bronstein, N. D. & Alivisatos, A. P. Solution-Processed, High-Speed, and High-Quantum-Efficiency Quantum Dot Infrared Photodetectors. *ACS Photonics* **3**, (2016).

25. Youngblood, N., Chen, C., Koester, S. J. & Li, M. Waveguide-integrated black phosphorus photodetector with high responsivity and low dark current. *Nat Photonics* **9**, (2015).

26. Xia, F., Mueller, T., Lin, Y. M., Valdes-Garcia, A. & Avouris, P. Ultrafast graphene photodetector. *Nat Nanotechnol* **4**, (2009).

27. Zha, J. *et al.* Infrared Photodetectors Based on 2D Materials and Nanophotonics. *Adv Funct Mater* **32**, (2022).

28. Zhuge, F. *et al.* Nanostructured Materials and Architectures for Advanced Infrared Photodetection. *Adv Mater Technol* **2**, (2017).

29. Tan, C. L. & Mohseni, H. Emerging technologies for high performance infrared detectors. *Nanophotonics* **7**, (2018).

30. Hunter, S. R., Maurer, G. S., Simelgor, G., Radhakrishnan, S. & Gray, J. High-sensitivity 25μm and 50μm pitch microcantilever IR imaging arrays. in *Infrared Technology and Applications XXXIII* vol. 6542 (2007).

31. Zhao, Y. *et al.* Characterization and performance of optomechanical uncooled infrared imaging system. in *Infrared Technology and Applications XXVIII* vol. 4820 (2003).

32. Lim, S. H., Choi, J., Horowitz, R. & Majumdar, A. Design and fabrication of a novel Bimorph microoptomechanical sensor. *Journal of Microelectromechanical Systems* **14**, (2005).

33. Dong, F. *et al.* An uncooled optically readable infrared imaging detector. *Sens Actuators A Phys* **133**, (2007).

34. Shi, H. *et al.* Optical sensitivity analysis of deformed mirrors for microcantilever array IR imaging. *Opt Express* **17**, (2009).

35. Grbovic, D. *et al.* Uncooled infrared imaging using bimaterial microcantilever arrays. *Appl Phys Lett* **89**, (2006).

36. Djurić, Z., Randjelović, D., Jokić, I., Matović, J. & Lamovec, J. A new approach to IR bimaterial detectors theory. *Infrared Phys Technol* **50**, (2007).

37. Hunter, S. R., Maurer, G., Jiang, L. & Simelgor, G. High-sensitivity uncooled microcantilever infrared imaging arrays. in *Infrared Technology and Applications XXXII* vol. 6206 (2006).

38. Perazzo, T. *et al.* Infrared vision using uncooled micro-optomechanical camera. *Appl Phys Lett* **74**, (1999).

39. Duan, Z. H. *et al.* Uncooled Optically Readable Bimaterial Micro-Cantilever Infrared Imaging Device. *Chinese Physics Letters* **20**, (2003).

40. Datskos, P. G. *et al.* Remote infrared radiation detection using piezoresistive microcantilevers. *Appl Phys Lett* **69**, (1996).

41. Oden, P. I., Datskos, P. G., Thundat, T. & Warmack, R. J. Uncooled thermal imaging using a piezoresistive microcantilever. *Appl Phys Lett* **69**, (1996).

42. Kenny, T. W. *et al.* Micromachined infrared sensors using tunneling displacement transducers. *Review of Scientific Instruments* **67**, (1996).

43. Lavrik, N., Archibald, R., Grbovic, D., Rajic, S. & Datskos, P. Uncooled MEMS IR imagers with optical readout and image processing. in *Infrared Technology and Applications XXXIII* vol. 6542 (2007).

44. Jin, Y., Shi, H. & Zhang, Q. Optical spatial filtering readout techniques for IR/THz imaging and their performance analysis. *Meas Sci Technol* **32**, (2021).

45. Miao, Z., Zhang, Q., Guo, Z., Wu, X. & Chen, D. Optical readout method for microcantilever array sensing and its sensitivity analysis. *Opt Lett* **32**, (2007).

46. Zhang, Q. *et al.* Optical readout uncooled infrared imaging detector using knife-edge filter operation. *Optoelectron Lett* **3**, (2007).

47. Grbovic, D., Lavrik, N. V., Rajic, S. & Datskos, P. G. Arrays of SiO2 substrate-free micromechanical uncooled infrared and terahertz detectors. *J Appl Phys* **104**, (2008).

48. Li, C. *et al.* IR imaging at room-temperature using substrate-free micro-cantilever array. in *Proceedings of 1st IEEE International Conference on Nano Micro Engineered and Molecular Systems, 1st IEEE-NEMS* (2006). doi:10.1109/NEMS.2006.334790.

49. Li, C. *et al.* A novel uncooled substrate-free optical-readable infrared detector: Design, fabrication and performance. in *Measurement Science and Technology* vol. 17 (2006).

50. Dong, F. *et al.* Uncooled infrared imaging device based on optimized optomechanical micro-cantilever array. *Ultramicroscopy* **108**, (2008).

51. Guo, Z. *et al.* Performance analysis of microcantilever arrays for optical readout uncooled infrared imaging. *Sens Actuators A Phys* **137**, (2007).

52. Jiao, B. *et al.* A novel opto-mechanical uncooled infrared detector. *Infrared Phys Technol* **51**, (2007).

53. Miao, Z. *et al.* Uncooled IR imaging using optomechanical detectors. *Ultramicroscopy* **107**, (2007).

54. Corbeil, J. L., Lavrik, N. V., Rajic, S. & Datskos, P. G. 'Self-leveling' uncooled microcantilever thermal detector. *Appl Phys Lett* **81**, (2002).

55. Dong, L. *et al.* The effective image denoising method for MEMS based IR image arrays. in *2008 International Conference on Optical Instruments and Technology: MEMS/NEMS Technology and Applications* vol. 7159 (2008).

56. Dong, L., Liu, X., Zhao, Y. & Liu, M. Study on the image processing algorithms for optical readout based uncooled MEMS IR imager systems. in *MEMS/MOEMS Technologies and Applications III* vol. 6836 (2007).

57. Gong, C. *et al.* The tolerable target temperature for bimaterial microcantilever array infrared imaging. *Opt Laser Technol* **45**, (2013).

58. Xiong, Z. *et al.* The pressure-dependent performance of a substrate-free focal plane array in an uncooled infrared imaging system. *J Appl Phys* **102**, (2007).

59. Ramaiah, M. R. & Prabakar, K. Effect of bimaterial microcantilever physical dimensions on photothermal sensing characteristics. *Sens Actuators A Phys* **331**, (2021).

60. Yang, C. K., Van Der Drift, E. W. J. M. & French, P. J. Review of scaling effects on physical properties and practicalities of cantilever sensors. *Journal of Micromechanics and Microengineering* **32**, (2022).

61. Ramaiah, M. R., Prabakar, K., Sundari, S. T. & Dhara, S. K. Wavelength dependence of photothermal deflection in Au/Si bimaterial microcantilevers. *Sens Actuators A Phys* **315**, (2020).

62. Zhang, N., Cheng, J. C., Warren, C. G. & Pisano, A. P. Bioinspired, uncooled chitin photomechanical sensor for thermal infrared sensing. in *Proceedings of IEEE Sensors* (2011). doi:10.1109/ICSENS.2011.6127320.

63. Rogalski, A., Kopytko, M. & Martyniuk, P. Two-dimensional infrared and terahertz detectors: Outlook and status. *Appl Phys Rev* **6**, (2019).

64. Goossens, S. *et al.* Broadband image sensor array based on graphene-CMOS integration. *Nat Photonics* **11**, (2017).

65. Luo, F. *et al.* High responsivity graphene photodetectors from visible to near-infrared by photogating effect. *AIP Adv* **8**, (2018).

66. Ni, Z. *et al.* Plasmonic Silicon Quantum Dots Enabled High-Sensitivity Ultrabroadband Photodetection of Graphene-Based Hybrid Phototransistors. *ACS Nano* **11**, (2017).

67. Pospischil, A. *et al.* CMOS-compatible graphene photodetector covering all optical communication bands. *Nat Photonics* **7**, (2013).

68. Cakmakyapan, S., Lu, P. K., Navabi, A. & Jarrahi, M. Gold-patched graphene nano-stripes for high-responsivity and ultrafast photodetection from the visible to infrared regime. *Light Sci Appl* **7**, (2018).

69. Valle, M. Bioinspired sensor systems. *Sensors* (2011) doi:10.3390/s111110180.

70. Zhao, Q., Wang, Y., Cui, H. & Du, X. Bio-inspired sensing and actuating materials. *J Mater Chem C Mater* **7**, 6493–6511 (2019).

71. Droogendijk, H., Brookhuis, R. A., De Boer, M. J., Sanders, R. G. P. & Krijnen, G. J. M. Towards a biomimetic gyroscope inspired by the fly's haltere using microelectromechanical systems technology. *J R Soc Interface* **11**, (2014).

72. Martín-Palma, R. J. & Kolle, M. [INVITED] Biomimetic photonic structures for optical sensing. *Opt Laser Technol* **109**, 270–277 (2019).

73. Daraghmeh, N. H., Chowdhry, B. Z., Leharne, S. A., Al Omari, M. M. & Badwan, A. A. Chitin. *Profiles Drug Subst Excip Relat Methodol* **36**, 35–102 (2011).

74. Kinoshita, S. & Yoshioka, S. Structural colors in nature: The role of regularity and irregularity in the structure. *ChemPhysChem* (2005) doi:10.1002/cphc.200500007.

75. Kinoshita, S., Yoshioka, S. & Kawagoe, K. Mechanisms of structural colour in the Morpho butterfly: Cooperation of regularity and irregularity in an iridescent scale. *Proceedings of the Royal Society B: Biological Sciences* (2002) doi:10.1098/rspb.2002.2019.

76. Giraldo, M. A. & Stavenga, D. G. Brilliant iridescence of Morpho butterfly wing scales is due to both a thin film lower lamina and a multilayered upper lamina. *J Comp Physiol A Neuroethol Sens Neural Behav Physiol* (2016) doi:10.1007/s00359-016-1084-1.

77. Miyako, E. *et al.* Self-assembled carbon nanotube honeycomb networks using a butterfly wing template as a multifunctional nanobiohybrid. *ACS Nano* **7**, (2013).

78. Yang, Q. *et al.* Bioinspired fabrication of hierarchically structured, pH-tunable photonic crystals with unique transition. *ACS Nano* (2013) doi:10.1021/nn400090j.

79. Ahmed, R., Ji, X., Atta, R. M. H., Rifat, A. A. & Butt, H. Morpho butterfly-inspired optical diffraction, diffusion, and bio-chemical sensing. *RSC Adv* (2018) doi:10.1039/c8ra04382e.

80. Zhou, L. *et al.* Butterfly Wing Hears Sound: Acoustic Detection Using Biophotonic Nanostructure. *Nano Lett* (2019) doi:10.1021/acs.nanolett.9b00468.

81. He, J. *et al.* Integrating plasmonic nanostructures with natural photonic architectures in Pd-modified Morpho butterfly wings for sensitive hydrogen gas sensing. *RSC Adv.* **8**, 32395–32400 (2018).

82. Lu, T. *et al.* Bioinspired thermoresponsive photonic polymers with hierarchical structures and their unique properties. *Macromol Rapid Commun* (2015) doi:10.1002/marc.201500246.

83. Pris, A. D. *et al.* Towards high-speed imaging of infrared photons with bio-inspired nanoarchitectures. *Nat Photonics* (2012) doi:10.1038/nphoton.2011.355.

84. Grujić, D. *et al.* Infrared camera on a butterfly's wing. *Opt Express* (2018) doi:10.1364/oe.26.014143.

85. Zhang, F. *et al.* Infrared detection based on localized modification of Morpho butterfly wings. *Advanced Materials* (2015) doi:10.1002/adma.201404534.

86. Shen, Q. *et al.* Butterfly Wing Inspired High Performance Infrared Detection with Spectral Selectivity. *Adv Opt Mater* **8**, 1901647 (2020).

87. Zhu, Y., Zhang, W. & Zhang, D. Fabrication of Sensor Materials Inspired by Butterfly Wings. *Adv Mater Technol* (2017) doi:10.1002/admt.201600209.

88. Li, Q., Zeng, Q., Shi, L., Zhang, X. & Zhang, K.-Q. Bio-inspired sensors based on photonic structures of Morpho butterfly wings: a review. *J. Mater. Chem. C* **4**, 1752–1763 (2016).

89. Xue, H. *et al.* Toward the Burgeoning Optical Sensors with Ultra-Precision Hierarchical Structures Inspired by Butterflies. *Adv Mater Interfaces* **8**, 2100142 (2021).

90. Osotsi, M. I. *et al.* Butterfly wing architectures inspire sensor and energy applications. *Natl Sci Rev* **8**, (2021).

91. Atanasijevic, P., Grujic, D., Krajinic, F., Mihailovic, P. & Pantelic, D. Characterization of a bioderived imaging sensor based on a Morpho butterfly's wing. *Opt Laser Technol* **159**, 108919 (2023).

92. Atanasijevic, P., Mihailovic, P., Grujic, D., Pantelic, D. & Skenderovic, H. Morpho butterfly wings as imaging sensor. in *14 th Photonics Workshop* 29 (2021).

93. Atanasijevic, P., Krajinic, F., Mihailovic, P. & Pantelic, D. Thermoelectric temperature control of Morpho butterfly wings used for radiation sensing. in *16 th Photonics Workshop* 20 (2023).

94. Zivic, M., Atanasijevic, P. & Barjaktarovic, M. Development of a digital holographic microscope for observation of Morpho butterfly wing scales. in *2021 29th Telecommunications Forum, TELFOR 2021 - Proceedings* (2021). doi:10.1109/TELFOR52709.2021.9653260.

95. Mićić, M., Atanasijević, P. & Mihailovic, P. Laser diode driver on a Programmable System on a Chip. *Review of Scientific Instruments* (2024) doi:10.1063/5.0184666.

96. Michelson, A. A. & Morley, E. W. On the relative motion of the Earth and the luminiferous ether. *Am J Sci* **s3-34**, (1887).

97. Abadie, J. *et al.* A gravitational wave observatory operating beyond the quantum shot-noise limit. *Nat Phys* **7**, (2011).

98. Goulielmakis, E. *et al.* Direct measurement of light waves. *Science (1979)* **305**, (2004).

99. Gabor, D. A new microscopic principle. *Nature* **161**, (1948).

100. Goodman, J. W. Introduction to Fourier Optics, Second Edition. *Optical Engineering* (1996) doi:10.1117/1.601121.

101. Kreis, T. *Handbook of Holographic Interferometry: Optical and Digital Methods*. (Wiley, 2006).

102. Schnars, U. & Jueptner, W. *Digital Holography: Digital Hologram Recording, Numerical Reconstruction, and Related Techniques*. (2005).

103. Aylo, R., Nehmetallah, G. T. & Williams, L. *Analog and Digital Holography with MATLAB*. *Analog and Digital Holography with MATLAB* (2015). doi:10.1117/3.2190844.

104. Kong, L. J., Sun, Y., Zhang, F., Zhang, J. & Zhang, X. High-Dimensional Entanglement-Enabled Holography. *Phys Rev Lett* **130**, (2023).

105. Buzas, A., Wolff, E. K., Benedict, M. G., Ormos, P. & Der, A. Biological Microscopy with Undetected Photons. *IEEE Access* **8**, (2020).

106. Vashist, S. K., Luppa, P. B., Yeo, L. Y., Ozcan, A. & Luong, J. H. T. Emerging Technologies for Next-Generation Point-of-Care Testing. *Trends Biotechnol* **33**, (2015).

107. Rivenson, Y., Zhang, Y., Günaydın, H., Teng, D. & Ozcan, A. Phase recovery and holographic image reconstruction using deep learning in neural networks. *Light Sci Appl* **7**, (2018).

108. Leith, E. N. & Upatnieks, J. Reconstructed Wavefronts and Communication Theory. *J Opt Soc Am* **52**, (1962).

109. Cooley, J. W. & Tukey, J. W. An algorithm for the machine calculation of complex Fourier series. *Math Comput* **19**, (1965).

110. Restrepo, J. F. & Garcia-Sucerquia, J. Magnified reconstruction of digitally recorded holograms by Fresnel-Bluestein transform. *Appl Opt* **49**, (2010).

111. Shimobaba, T. & Ito, T. *Computer Holography: Acceleration Algorithms and Hardware Implementations*. (2019). doi:10.1201/9780429428005.

112. Shimobaba, T. *et al.* Computational wave optics library for C++: CWO++ library. *Comput Phys Commun* (2012) doi:10.1016/j.cpc.2011.12.027.

113. Ghiglia, D. C. & Pritt, M. D. *Two-Dimensional Phase Unwrapping: Theory, Algorithms, and Software*. *J Investig Dermatol* vol. 120 (1998).

114. Zhao, M. *et al.* Quality-guided phase unwrapping technique: Comparison of quality maps and guiding strategies. *Appl Opt* **50**, (2011).

115. Kemao, Q., Gao, W. & Wang, H. Windowed Fourier-filtered and quality-guided phase-unwrapping algorithm. *Appl Opt* (2008) doi:10.1364/AO.47.005420.

116. Park, S., Kim, Y. & Moon, I. Automated phase unwrapping in digital holography with deep learning. *Biomed Opt Express* **12**, (2021).

117. Zhao, Z. *et al.* Robust 2D phase unwrapping algorithm based on the transport of intensity equation. *Meas Sci Technol* **30**, (2019).

118. Bianco, V. *et al.* Strategies for reducing speckle noise in digital holography. *Light Sci Appl* **7**, (2018).

119. Kreis, T., Jueptner, W. P. O. & Geldmacher, J. Principles of digital holographic interferometry. in *Optics & Photonics* (1998).

120. Coppola, G. & Ferrara, M. A. Polarization-Sensitive Digital Holographic Imaging for Characterization of Microscopic Samples: Recent Advances and Perspectives. *Applied Sciences* **10**, (2020).

121. Kühn, J. *et al.* Real-time dual-wavelength digital holographic microscopy with a single hologram acquisition. *Opt Express* **15**, (2007).

122. Wu, Y. & Ozcan, A. Lensless digital holographic microscopy and its applications in biomedicine and environmental monitoring. *Methods* **136**, 4–16 (2018).

123. Lee, M., Yaglidere, O. & Ozcan, A. Field-portable reflection and transmission microscopy based on lensless holography. *Biomed Opt Express* (2011) doi:10.1364/boe.2.002721.

124. Tseng, D. *et al.* Lensfree microscopy on a cellphone. *Lab Chip* (2010) doi:10.1039/c003477k.

125. Gerchberg, R. W. & Saxton, W. O. PRACTICAL ALGORITHM FOR THE DETERMINATION OF PHASE FROM IMAGE AND DIFFRACTION PLANE PICTURES. *Optik (Stuttgart)* **35**, (1972).

126. Latychevskaia, T. & Fink, H. W. Solution to the twin image problem in holography. *Phys Rev Lett* **98**, (2007).

127. Ting-Chung Poon, J.-P. L. *Introduction to Modern Digital Holography with MatLab*. *Journal of Chemical Information and Modeling* vol. 53 (2013).

128. Hopffer, C. *Neue Lepidopteren von Peru Und Bolivia*. (1874).

129. Berthier, S. *Iridescences: The Physical Colors of Insects*. *Optical Engineering* (2006). doi:10.1007/b106784.

130. Elbaz, A. *et al.* Chitin-Based Anisotropic Nanostructures of Butterfly Wings for Regulating Cells Orientation. *Polymers (Basel)* **9**, (2017).

131. Rehman, A. ul, Ahmad, I. & Qureshi, S. A. Biomedical Applications of Integrating Sphere: A Review. *Photodiagnosis Photodyn Ther* **31**, (2020).

132. Pantelic, D. V., Grujic, D. Ž. & Vasiljevic, D. M. Single-beam, dual-view digital holographic interferometry for biomechanical strain measurements of biological objects. *J Biomed Opt* (2014) doi:10.1117/1.jbo.19.12.127005.

133. Yang, K., Wang, M., Wang, Z. & Fan, Z. Design of laser diode driver with constant current and temperature control system. in (2018). doi:10.1117/12.2285055.

134. Zhao, Y. *et al.* High-Precision Semiconductor Laser Current Drive and Temperature Control System Design. *Sensors* **22**, (2022).

135. Rudd, E. P. Laser diode driver with 5-decade range. *IEEE Trans Instrum Meas* **49**, (2000).

136. Hodgson, D. & Olsen, B. Protecting your laser diode. *ILX Lightwave Corporation* (2003).

137. Beauregard, B. Improving the Beginner's PID. http://brettbeauregard.com/blog/2011/04/improving-the-beginners-pid-introduction/ (2011).

138. Pease, R. *AN-1515 A Comprehensive Study of the Howland Current Pump*. *Texas Instruments* (2013).

139. Yang, A. D., Xia, B. S., Ouyang, C. L., Hou, D. W. & Guo, E. L. An ultrahigh performance laser driver based on novel composite topology enhanced Howland current Source. *Review of Scientific Instruments* **93**, (2022).

140. Dideriksen, T. Nikon SDK C# Wrapper. https://sourceforge.net/projects/nikoncswrapper/.

141. THORLABS. Laser Diodes: Ø3.8 mm, TO-46, Ø5.6 mm, Ø9 mm, and Ø9.5 mm TO Cans. https://www.thorlabs.com/newgrouppage9.cfm?objectgroup_id=5260.

142. Hetnarski, R. B. & Eslami, M. R. Thermal stresses - Advanced theory and applications. *Solid Mechanics and its Applications* **158**, (2009).

143. Blaikie, A., Miller, D. & Alemán, B. J. A fast and sensitive room-temperature graphene nanomechanical bolometer. *Nat Commun* **10**, (2019).

144. Czerwoniec, A., Torzewicz, T., Samson, A. & Janicki, M. Estimation of heat transfer coefficient temperature dependence from cooling curve measurements. in *Proceedings of the 22nd International Conference Mixed Design of Integrated Circuits and Systems, MIXDES 2015* (2015). doi:10.1109/MIXDES.2015.7208555.

145. Janicki, M., Kindermann, S., Pietrzak, P. & Napieralski, A. Estimation of local temperature dependent heat transfer coefficient for dynamic thermal analysis of electronic circuits. *J Phys Conf Ser* **135**, (2008).

146. Rogers, B., Adams, J. & Pennathur, S. *Nanotechnology: Understanding Small Systems: Third Edition*. *Nanotechnology: Understanding Small Systems: Third Edition* (2014). doi:10.1201/b17424.

147. Hecht, E. Optics / Eugene Hecht. *Optics* 338–387 (2017).

148. Greg Hollows & Nicholas James. The Airy Disk and Diffraction Limit. https://www.edmundoptics.com/knowledge-center/application-notes/imaging/limitations-on-resolution-and-contrast-the-airy-disk/.

149. Saleh, B. & Teich, M. *Fundamentals of Photonics, 3rd Edition*. (2019).

150. Paschotta, R. Gaussian Beams. in *Field Guide to Lasers* (2009). doi:10.1117/3.767474.p18.

151. De Araújo, M. A. C., Silva, R., De Lima, E., Pereira, D. P. & De Oliveira, P. C. Measurement of Gaussian laser beam radius using the knife-edge technique: Improvement on data analysis. *Appl Opt* **48**, (2009).

152. González-Cardel, M., Arguijo, P. & Díaz-Uribe, R. Gaussian beam radius measurement with a knife-edge: A polynomial approximation to the inverse error function. *Appl Opt* **52**, (2013).

153. Edmund Optics. Testing and Targets. https://www.edmundoptics.com/knowledge-center/application-notes/imaging/testing-and-targets.

154. Leung, C. & Donnelly, T. D. Measuring the spatial resolution of an optical system in an undergraduate optics laboratory. *Am J Phys* **85**, 429–438 (2017).

155. Boreman, G. D. *Modulation Transfer Function in Optical and Electro-Optical Systems, Second Edition*. (2021). doi:10.1117/3.2581373.

156. Estribeau, M. & Magnan, P. Fast MTF measurement of CMOS imagers using ISO 12333 slanted-edge methodology. in *Proc.SPIE* vol. 5251 (2004).

157. Buhr, E., Günther-Kohfahl, S. & Neitzel, U. Accuracy of a simple method for deriving the presampled modulation transfer function of a digital radiographic system from an edge image. *Med Phys* **30**, 2323–2331 (2003).

158. Viallefont-Robinet, F. *et al.* Comparison of MTF measurements using edge method: towards reference data set. *Opt Express* **26**, (2018).

159. van den Bergh, F. Deferred slanted-edge analysis: a unified approach to spatial frequency response measurement on distorted images and color filter array subsets. *Journal of the Optical Society of America A* **35**, (2018).

160. Williams, D. Benchmarking of the ISO 12233 Slanted-edge Spatial Frequency Response Plug-in. in *Society for Imaging Science and Technology: Image Processing, Image Quality, Image Capture, Systems Conference* (1998).

161. Bloch, D. Ray Optics extension for Inkscape. https://inkscape.org/~dbloch/★ray-optics.

Appendix A

A MATLAB code for hologram reconstruction using the Fourier form of the Fresnel integral. Each code section is commented on in detail.

```
%% Simple holographic reconstruction - Fourier form of the Fresnel
integral

clear all
close all
clc

% Input parameters

FilterDC = 1; % 1 - YES, 0 - NO
FilterTwin = 1; % 1 - YES, 0 - NO
side = 'left'; % where is the object?

% Podaci iz eksperimenta:
pixelSize = 2.45*1.0e-6; % the pixel pitch of the detector (CMOS) [m]
WaveLength = 532.0*1.0e-9; % laser's wavelwngth [m]
z = 1.05; % object to CMOS distance [m]
z_ps = 1.005; % point source to CMOS distance [m]

% read the hologram image
hologram = double(imread(['path to the input image...']));

% reconstruct the hologram
E2_1 = Fresnel_filt_0(hologram(:,:,2),WaveLength,pixelSize,z, ...
    z_ps,0,0,FilterDC,FilterTwin,side); % the reconstructed complex E
field


% Hologram intensity
E2_int=abs(E2_1).^2; % the intensity is proportional to |E|^2

E2_int_log = log(1 + E2_int)./log(2); % adjusting the contrast

MAX = max(max(E2_int_log)); % maximum value
MIN = min(min(E2_int_log)); % minimum value
LowLim = 70; % lower useful boundary between the MAX and the MIN [%]
UpLim = 100; % upper useful boundary between the MAX and the MIN [%]

% show the adjusted intensity image of the recontructed field
```

```
figure
imshow(E2_int_log,[MIN+(LowLim/100)*(MAX-MIN) (UpLim/100)*MAX]);

function E2 = Fresnel_filt_0(holo_im, WaveLength, pixelSize, z, z_ps, ...
    xR, yR, FilterDC, FilterTwin, side)

% This is the function for the illumination and electric filed
propagation
% from the hologram to the image (object) plane. The illumination is
% presumed to be using a spherical wave.
% holo_im - hologram image
% WaveLength - wavelength of the recording/reconstruction laser [nm]
% pixelSize - CMOS pixel dimensions [m]
% z - object to CMOS distance [m]
% z_ps - point source to CMOS distance [m]
% xR - x point source coordinate [m]
% yR - y point source coordinate [m]
% FilterDC - 1 - YES, 0 - NO
% FilterTwin - 1 - YES, 0 - NO
% side - where is the object? 'left' or 'right'


k = 2*pi/WaveLength; % wave number
si = size(holo_im); % hologram size
N = si(2); % horizontal dimension
[mm, nn] = meshgrid((-N/2):(N/2)-1); % creating the grid

x1 = pixelSize.*mm; % x axis - hologram plane
y1 = pixelSize.*nn; % y axis - hologram plane

x2 = mm.*WaveLength.*z./pixelSize./N; % x axis - object plane
y2 = nn.*WaveLength.*z./pixelSize./N; % y axis - object plane

Cz = (exp(1i*k*z)./(1i*WaveLength*z)).*exp((1i.*pi./WaveLength./z) ...
    .*(x2.^2 +  y2.^2)); % the phase factor before of the integral

E1 = padarray(holo_im,si(2)-si(1),'post'); % zero padding of the hologram
% (resolution enhancement)

% the illumination of the hologram with the spherical reconstruction wave
E1 = E1.*exp(-1i.*k.*sqrt( (x1-xR).^2 + (y1-yR).^2 + (z_ps).^2));

% filter the DC term using a moving average filter?
if FilterDC == true
    windowSize = 3; % window size for the moving average
    kernel = ones(windowSize, windowSize) / windowSize ^ 2;
    E1_mov_avg = imfilter(E1, kernel, 'symmetric');

    E1 = E1 - E1_mov_avg; % subtract the moving average
end

% filter the twin image?
if FilterTwin == true
    X = ones(N,N);
    if strcmp(side,'left')
        X(:,1:N/2) = 0; % mask creation - left
```

```
    elseif strcmp(side,'right')
            X(:,N/2:N) = 0; % mask creation - right
    else X = 0;
    end
    E1 = ifft2(fft2(E1).*X); % the filtered field
end

% solving the Fresnel integral (2D FFT)
E2 = fft2(E1.*exp((1i.*pi./WaveLength./z).*(x1.^2 +  y1.^2)));
E2 = Cz.*fftshift(E2); % shifting the reconstruction
end
```

Appendix B

The Appendix is dedicated to the visualization of the time evolution of the light induced freestanding sample vibrations, due to a 19 mW, 110 ms, 980 nm EB pulse. The vibrating pattern appears at the rising edge of the EB. This is easily visible in the intensity images. Then the vibrations start to fade away, only to be excited once again at the falling edge of the EB, although this time to a lesser extent.

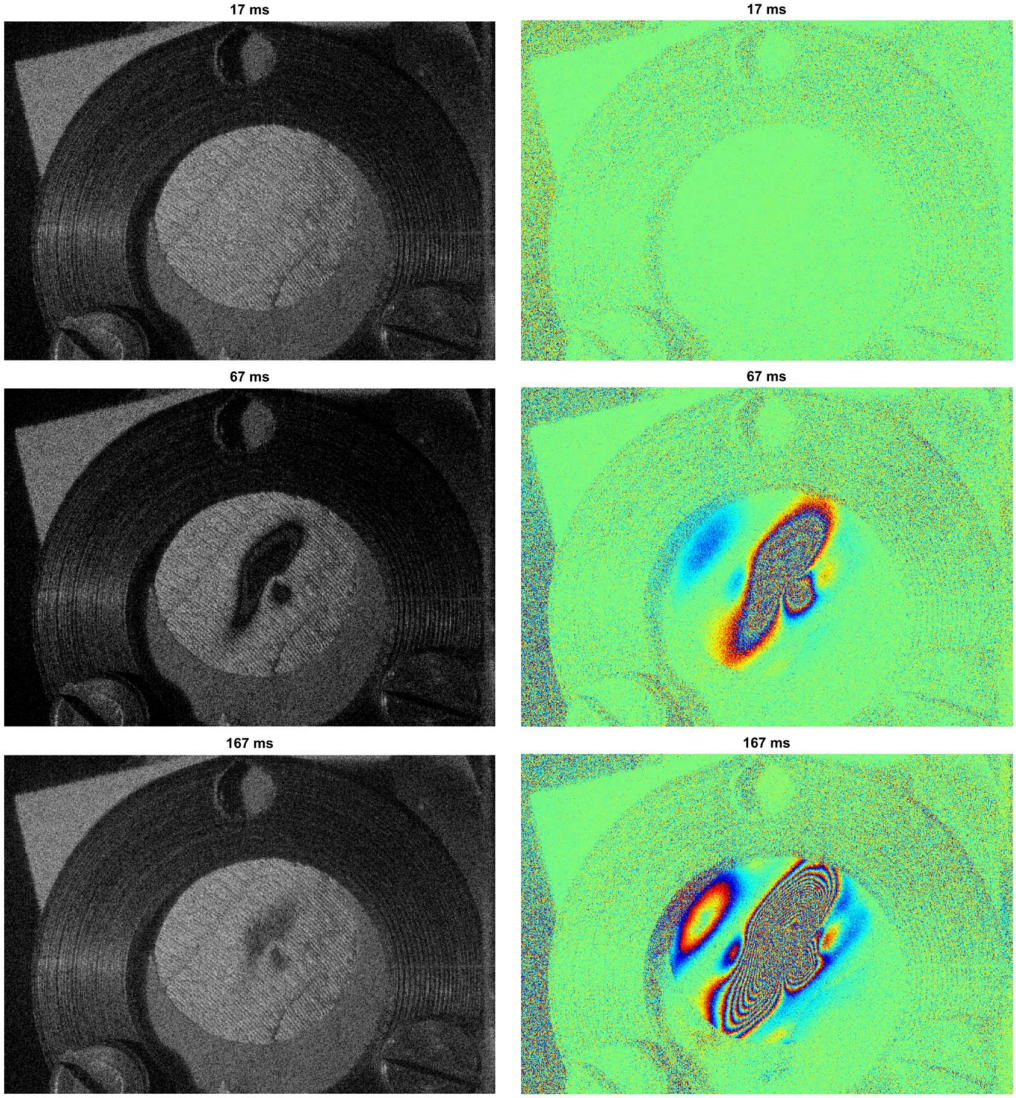

Figure B.1 Time evolution of the illumination induced vibrations $17 - 167\ ms$ (rising edge).

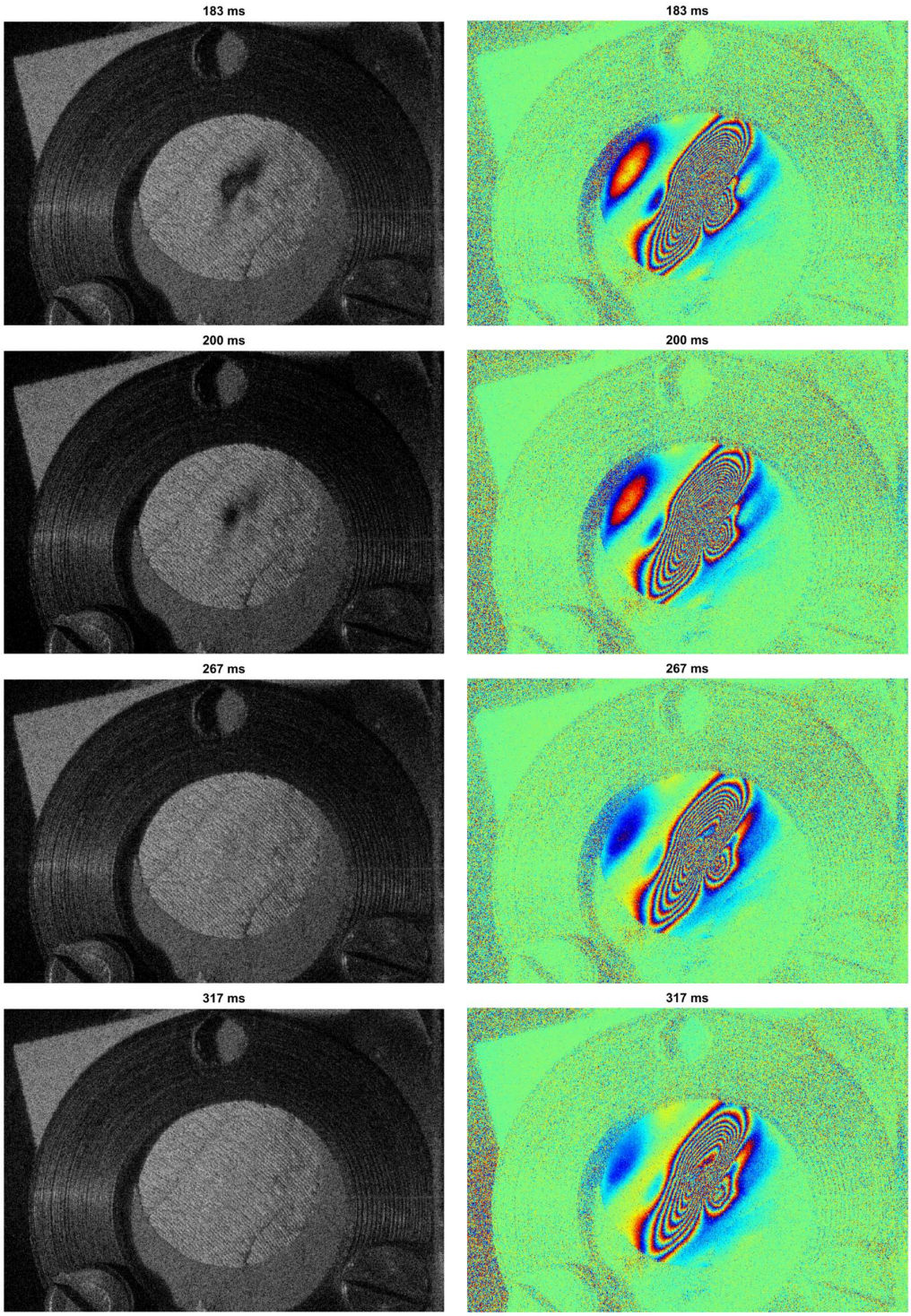

Figure B.2 Time evolution of the illumination induced vibrations $183 - 317\,ms$ (falling edge).

Biography

Petar Atanasijević was born on the 11th of August 1994 in Belgrade, where he finished his primary and grammar school education. He acquired his B. Sc. degree in 2017, at the University of Belgrade, School of Electrical Engineering, Physical Electronics - Nanoelectronics, Optoelectronics, Laser Technology module, with the GPA of 9.0. The following year, he obtained a M. Sc. degree at the Nanoelectronics and Photonics module, attended at the same School, with the 10.0 GPA. Throughout his bachelor and master's studies, he focused his research interests toward the development of readily available high performing electronic devices for biomedical and renewable energy resources applications. His final theses were conducted under the careful guidance of Prof. Dr. Peđa Mihailović.

Since December 2017, he has been employed at the Department of Microelectronics and Technical Physics, School of Electrical Engineering, where he currently holds the position of a teaching assistant. He is engaged in teaching a multitude of courses, ranging from introductory physics, to sensors, applied electronics and photonics. Up to this point, he has published five scientific papers in international peer-reviewed journals. His research interests are wide, spreading from digital holographic interferometry, novel sensing methods and precise electronics, to all-optical computing, and beyond. He was an active participant in multiple national, international and commercial projects, regarding scientific, engineering and teaching advancements. He is a student member of the Optical Society of Serbia, and OPTICA.

Изјава о ауторству

Име и презиме аутора Петар Атанасијевић

Број индекса 2018/5016

Изјављујем

да је докторска дисертација под насловом

Карактеризација одзива крила Морфо лептира као холографски испитиваног сензора слике

(енг. Response characterization of a Morpho butterfly's wing as a holographically interrogated imaging sensor)

- резултат сопственог истраживачког рада;
- да дисертација у целини ни у деловима није била предложена за стицање друге дипломе према студијским програмима других високошколских установа;
- да су резултати коректно наведени и
- да нисам кршио/ла ауторска права и користио/ла интелектуалну својину других лица.

Потпис аутора

У Београду, 26.02.2024.

Изјава о истоветности штампане и електронске верзије докторског рада

Име и презиме аутора Петар Атанасијевић

Број индекса 2018/5016

Студијски програм Електротехника и рачунарство, модул Наноелектроника и фотоника

Наслов рада Карактеризација одзива крила Морфо лептира као холографски испитиваног сензора слике

Ментор проф. др Пеђа Михаиловић

Изјављујем да је штампана верзија мог докторског рада истоветна електронској верзији коју сам предао/ла ради похрањивања у **Дигиталном репозиторијуму Универзитета у Београду**.

Дозвољавам да се објаве моји лични подаци везани за добијање академског назива доктора наука, као што су име и презиме, година и место рођења и датум одбране рада.

Ови лични подаци могу се објавити на мрежним страницама дигиталне библиотеке, у електронском каталогу и у публикацијама Универзитета у Београду.

Потпис аутора

У Београду, 26.02.2024.

Изјава о коришћењу

Овлашћујем Универзитетску библиотеку „Светозар Марковић“ да у Дигитални репозиторијум Универзитета у Београду унесе моју докторску дисертацију под насловом:

Карактеризација одзива крила Морфо лептира као холографски испитиваног сензора слике

(енг. Response characterization of a Morpho butterfly's wing as a holographically interrogated imaging sensor)

која је моје ауторско дело.

Дисертацију са свим прилозима предао/ла сам у електронском формату погодном за трајно архивирање.

Моју докторску дисертацију похрањену у Дигиталном репозиторијуму Универзитета у Београду и доступну у отвореном приступу могу да користе сви који поштују одредбе садржане у одабраном типу лиценце Креативне заједнице (Creative Commons) за коју сам се одлучио/ла.

1. Ауторство (CC BY)

2. Ауторство – некомерцијално (CC BY-NC)

3. Ауторство – некомерцијално – без прерада (CC BY-NC-ND)

4. Ауторство – некомерцијално – делити под истим условима (CC BY-NC-SA)

5. Ауторство – без прерада (CC BY-ND)

6. Ауторство – делити под истим условима (CC BY-SA)

(Молимо да заокружите само једну од шест понуђених лиценци.
Кратак опис лиценци је саставни део ове изјаве).

Потпис аутора

У Београду, 26.02.2024.

1. **Ауторство.** Дозвољавате умножавање, дистрибуцију и јавно саопштавање дела, и прераде, ако се наведе име аутора на начин одређен од стране аутора или даваоца лиценце, чак и у комерцијалне сврхе. Ово је најслободнија од свих лиценци.

2. **Ауторство – некомерцијално.** Дозвољавате умножавање, дистрибуцију и јавно саопштавање дела, и прераде, ако се наведе име аутора на начин одређен од стране аутора или даваоца лиценце. Ова лиценца не дозвољава комерцијалну употребу дела.

3. **Ауторство – некомерцијално – без прерада.** Дозвољавате умножавање, дистрибуцију и јавно саопштавање дела, без промена, преобликовања или употребе дела у свом делу, ако се наведе име аутора на начин одређен од стране аутора или даваоца лиценце. Ова лиценца не дозвољава комерцијалну употребу дела. У односу на све остале лиценце, овом лиценцом се ограничава највећи обим права коришћења дела.

4. **Ауторство – некомерцијално – делити под истим условима.** Дозвољавате умножавање, дистрибуцију и јавно саопштавање дела, и прераде, ако се наведе име аутора на начин одређен од стране аутора или даваоца лиценце и ако се прерада дистрибуира под истом или сличном лиценцом. Ова лиценца не дозвољава комерцијалну употребу дела и прерада.

5. **Ауторство – без прерада.** Дозвољавате умножавање, дистрибуцију и јавно саопштавање дела, без промена, преобликовања или употребе дела у свом делу, ако се наведе име аутора на начин одређен од стране аутора или даваоца лиценце. Ова лиценца дозвољава комерцијалну употребу дела.

6. **Ауторство – делити под истим условима.** Дозвољавате умножавање, дистрибуцију и јавно саопштавање дела, и прераде, ако се наведе име аутора на начин одређен од стране аутора или даваоца лиценце и ако се прерада дистрибуира под истом или сличном лиценцом. Ова лиценца дозвољава комерцијалну употребу дела и прерада. Слична је софтверским лиценцама, односно лиценцама отвореног кода.